UNIVERSITÀ
DEGLI STUDI
DI PADOVA

SEDE AMMINISTRATIVA: Università degli Studi di Padova
Centro di Ateneo di Studi e Attività Spaziali "Giuseppe Colombo" (CISAS)

SCUOLA DI DOTTORATO DI RICERCA IN: Scienze Tecnologie e Misure Spaziali
INDIRIZZO: Astronautica e Scienze da Satellite
CICLO XXVI

PLANET FORMATION IN BINARY STAR SYSTEMS AND ITS RELEVANCE DURING TARGET SELECTION FOR EXTRASOLAR PLANET SEARCH WITH THE TRANSIT METHOD

DIRETTORE DELLA SCUOLA: Prof. Giampiero Naletto
COORDINATORE DI INDIRIZZO: Prof. Giampiero Naletto
SUPERVISORE: Prof. Francesco Marzari
CO–SUPERVISORE: Dr. Silvano Desidera

PHD STUDENT: GIOVANNI PICOGNA

This thesis is dedicated to Elisa, who always supports me and believes in my dreams.

ABSTRACT

In this Thesis I have studied the impact of binary stars on planet formation and evolution in order to maximize the process of target selection in a future space mission devoted to planet detection. The impact has been firstly addressed via a statistical analysis of the frequency and characteristics of planets in those complex systems. Then, a more in–depth investigation has been made by modeling different planet formation stages in circumbinary and circumstellar environments. I have also studied the impact of close stellar encounters on the evolution of planetary systems in order to explore the relevance of this effect on the statistics of exoplanet mass and orbital distributions.

According to the outcome of my simulations the presence of the companion star has a strong impact on planet formation and evolution process. The protoplanetary disk is strongly perturbed, exhibiting tidal waves and developing an overall eccentric shape. In the third dimension hydraulic jumps are observed that could prevent the dust sedimentation and halt the planetesimal formation.

In circumbinary disks, the planetesimal evolution appears strongly affected by the asimmetry of the gravitational field of the eccentric disk, that excites mutual planetesimal velocities, favouring fragmentation rather than accretion, thus preventing planet formation.

All these effects together influence the overall statistics of planets in binaries and must be taken into account when deriving the general properties of exoplanet systems since the majority of stars are born in multiple configurations, and nearly half of the them are part of a binary system in the Galactic field. Planets in binaries are expected to be a frequent and interesting occurrence and will have a high impact on the target selection process. Future space missions will for sure improve our statistic of these planetary systems, and allow a better understanding of the complex process of planet formation in these esotic environments.

SOMMARIO

In questa Tesi ho studiato l'impatto della binarietà sulla formazione ed evoluzione planetaria allo scopo di massimizzare il processo di selezione dei target in una futura missione spaziale dedicata alla scoperta di transiti planetari. L'impatto è stato studiato prima con un'analisi statistica della frequenze e delle caratteristiche dei pianeti in questi sistemi complessi. In seguito, si è eseguito uno studio più dettagliato dalla modellizzazione di diversi scenari di formazione planetaria in sistemi circumbinari e circumstellari in binarie. Inoltre,

ho studiato l'impatto dei flyby stellari sull'evoluzione dei sistemi planetari per capire la rilevanza di questo fenomeno sulla distribuzione statistica della massa e dei parametri orbitali dei pianeti extrasolari osservati.

Dal risultato delle simulazioni effettuate, la presenza della compagna stellare nel sistema binario ha un forte impatto sul processo di formazione ed evoluzione dei sistemi planetari. I dischi protoplanetari sono fortemente perturbati, mostrando delle onde mareali e sviluppando una forma eccentrica. Nella terza dimensione si osservano dei salti idraulici che possono prevenire la sedimentazione e bloccare il processo di formazione planetaria.

Nei dischi circumbinari, l'evoluzione dei planetesimi appare fortemente influenzata dall'asimmetria del campo gravitazionale del disco eccentrico, portando ad un incremento delle velocità mutue e favorendo la frammentazione piuttosto che l'accrescimento in protopianeti.

Tutti questi effetti influenzano la statistica dei pianeti in binarie e devono essere presi in considerazione quando si vuole derivare le proprietà generali dei sistemi planetari, poiché la maggior parte delle stelle si è formata in configurazioni multiple e circa la metà di esse nel campo galattico è parte di un sistema binario. Ci si aspetta che i pianeti in binarie siano un evento frequente ed interessante e dunque abbiano un impatto notevole nel processo di selezione dei target. Le missioni spaziali future sicuramente miglioreranno la statistica di questi sistemi planetari, e permetteranno una più profonda comprensione dei complessi processi di formazione planetaria in questi ambienti esotici.

PUBLICATIONS

Some ideas and figures have appeared previously in the following publications:

F. Marzari and G. Picogna. Circumstellar disks do erase the effects of stellar flybys on planetary systems. *A&A*, 550:A64, February 2013. doi: 10.1051/0004-6361/201220436.
F. Marzari and P. Thebault and H. Scholl and G. Picogna and C. Baruteau. *A&A*, 553:A71, May 2013. doi: 10.1051/0004-6361/201220893.
G. Picogna and F. Marzari. Three-dimensional modeling of radiative disks in binaries. *A&A*, 556:A148, August 2013. doi: 10.1051/0004-6361/201321860.

Accepted for publication in *A&A*:

G. Picogna and F. Marzari. Effects of stellar flybys on planetary systems: 3D modeling of the circumstellar disks damping effects.

CONTENTS

1

INTRODUCTION

The importance of binary and multiple stars was known since the beginning of modern astronomy. Most Sun-like stars are believed to form as gravitationally bound pairs (~ 75% from numerical experiments by (Parker et al., 2011)), and nearly half of them are currently found to be member of a couple or multiple system (Raghavan et al., 2010; Duquennoy and Mayor, 1991).

However, after the first discoveries of an extrasolar planets orbiting a Solar–type star by Mayor and Queloz (1995), the surveys dedicated to planet detection targeted only single stars because of technical difficulties in detecting binary and multiple star systems.

The refining of ground observational techniques and the advent of space missions devoted to planet detection, like CoRoT and Kepler, in the last decade has overcome these difficulties permitting the discovery of planets even in binary star systems.

They have been found both in S–type orbit, encircling one component of the binary, and P–type orbit, around both components of the stellar system.

These are challenging planet formation environments, since the stellar companion perturbations can significantly affect the course of it, depending on the architecture of the system. Nonetheless, the understanding of these processes is of paramount importance in order to address the general picture of planet formation and evolution, since the majority of stars are born in this configuration.

Thus, estimating the prevalence of planets in binary systems is a relevant issue when computing the fraction of stars hosting planets. In addition, planet formation in binaries is important to understand the single steps of planet growth and how it is modified by an external perturber. The prevalence is also important when planning extrasolar planet search surveys for predicting the potential number of discoveries, including binary targets.

The next generation space missions devoted to planet detection will have the possibility to better characterize the exoplanets bulk and atmospheric properties obtaining unprecedented informations on the processes at play.

PLATO, which is a proposed ESA mission for the next decade, will search for extrasolar planets orbiting brigth stars using the transit method. It would be capable of detecting planets down to Earth–size orbiting different stellar environments, including binaries. Furthermore, it will be aided by the current astrometric Gaia mission which will furnish plenty of data about stellar physical parameters, in particular about astrometric binaries, permitting PLATO to obtain a more accurate physical characterization of the planetary systems, and improve greatly the statistics of planets in binary systems. Mostly important, with asteroseismology analysis of the host stars, PLATO would be able to determine the age of the planetary systems, improving our knowledge about long–term dynamical processes.

With these characteristics, PLATO is the perfect mission to address the planet formation and evolution processes in the general frame, and in particular around binary stars. The outcome of the mission will possibly give important hints for understanding the influence of an external perturber on the various phases of the system evolution.

In order to maximize the planet detection in binary systems and select the most promising targets for PLATO and future missions devoted to planet detection, is then necessary not only to study the statistical informations obtained from past observation of this class of objects, but also to understand the theory of planet formation and evolution in these perturbed systems.

In Chap. 2 I will review the main techniques of planet detection, dealing in particular with the transit method which is the most used in space missions. Then, the past and future space mission devoted to planet detection will be analysed in Chap. 3, focusing in particular on PLATO, that is the most promising for finding planets in binary stars. In Chap. 4, a statistical analysis of the impact of binaries in planet detection on a putative field of the PLATO mission is performed, togheter with an analysis of the main differences between planet hosted by binary stars respect to those in single stellar systems.

With the aim of understanding the differences observed in the statistical analysis, I will review the classic theory of planet formation in Chap. 5. Then, the same process is studied in circumstellar (Chap. 6) and circumbinary environments (Chap. 7), deriving the influence of the binary companion with different system architectures. The long–term evolution of planetary systems will be addressed in Chap. 8. In particular, I will deal with the influence of star close encounters on the dynamical evolution of planetary systems in Chap. 9. Finally, in Chap. 10 I will draw the conlusions of this work.

Part I

PLANET DETECTION

2

EXOPLANET DETECTION AND THE TRANSIT METHOD

In this chapter we will review the main techniques of planet detection, paying particular attention on their relevance to find planets orbiting binary stars.

2.1 EXOPLANET DETECTION TECHNIQUES

Lets consider a planetary system formed by a star of mass $M_\star$ and a planet of mass M_p, orbiting around their common center of mass. In a reference frame centered on the barycenter, the star has a position vector $\mathbf{r}_\star$ and the planet $\mathbf{r}_p$, while the relative position vector is given by $\mathbf{r} = \mathbf{r}_p - \mathbf{r}_\star$. We could in priciple study both the baricentric orbits of the two objects and their relative orbit. However, there are some importants relations that hold between them that will help us to obtain their orbital parameters, starting from the observations about one of them. This aspect is crucial since in indirect methods we obtain data only about the star orbit or the relative orbit. Thus, using these relations, we could link them together from different observational techniques and obtain the physical and orbital parameters of the undetected planet.

In a barycentric reference frame we have

$$M_\star \mathbf{r}_\star + M_p \mathbf{r}_p = 0,$$

so the position vectors are proportional to the relative vector

$$\mathbf{r}_\star = -\frac{M_p}{M}\mathbf{r}, \tag{1}$$

$$\mathbf{r}_p = \frac{M_\star}{M}\mathbf{r}, \tag{2}$$

where $M = M_\star + M_p$. Furthermore, calling $\mathbf{v}_\star$, $\mathbf{v}_p$ the barycentric star and planet velocity, $\mathbf{v} = \mathbf{v}_p - \mathbf{v}_\star$ the relative velocity, and deriving with respet to time the eqs. 1–2 we obtain

$$\mathbf{v}_\star = -\frac{M_p}{M}\mathbf{v}, \tag{3}$$

$$\mathbf{v}_p = \frac{M_\star}{M}\mathbf{v}, \tag{4}$$

where we do not consider the mass evolution of the two bodies, which is a good approximation if the stars are in their main sequence. Since from the Kepler's laws we know that the relative orbit is an ellipse with positions and velocities given by $\mathbf{r}, \mathbf{v}$, the barycentric orbits are rescaled versions of the relative orbit, so they are ellipses with

1. a semimajor axis rescaled in the same way

$$\mathbf{a}_\star = \frac{M_p}{M}\mathbf{a}, \tag{5}$$

$$\mathbf{a}_p = \frac{M_\star}{M}\mathbf{a}, \tag{6}$$

   where $a = a_\star + a_p$ is the semimajor axis of the relative ellipse,

2. the same shape which is defined by their eccentricity $e = e_\star = e_p$
3. the same period P,
4. the same inclination i, since in a two–body problem the orbits are coplanar,
5. an orientation that differs by π on the plane.

Therefore, from the Newton's law for the relative orbit and the eqs. 1–2 we obtain

$$\ddot{\mathbf{r}} = -\frac{GM}{r^3}\mathbf{r}, \tag{7}$$

$$\ddot{\mathbf{r}}_\star = -\frac{G(M_p^3/M^2)}{r_\star^3}\mathbf{r}_\star, \tag{8}$$

$$\ddot{\mathbf{r}}_p = -\frac{G(M_\star^3/M^2)}{r_p^3}\mathbf{r}_p, \tag{9}$$

so they all obey a version of the Kepler's third law with the mass values rescaled as (M_p^3/M^2) for the star and $(M_\star^3/M^2)$ for the planet.

The position and velocity vectors of the relative orbit in polar coordinates are given by

$$\mathbf{r} = (r\cos f)\hat{\imath} + (r\sin f)\hat{\jmath}, \tag{10}$$

$$\mathbf{v} = (\dot{r}\cos f - r\dot{f}\sin f)\hat{\imath} + (\dot{r}\sin f + r\dot{f}\cos f)\hat{\jmath}, \tag{11}$$

where $\hat{\imath}$ and $\hat{\jmath}$ are the unit vectors, f is the true anomaly, and r is the magnitude of the position vector, which can be derived from the equation of the ellipse in polar coordinates

$$r = \frac{a(1-e^2)}{1+e\cos f}. \tag{12}$$

From the second Kepler's law we can also express the true anomaly evolution as

$$\dot{f} = \frac{df}{dt} = \frac{2\pi a^2}{Pr^2}\sqrt{1-e^2}, \tag{13}$$

thus, the velocity vector, from eqs. 11,12, 13, can be written also as

$$\mathbf{v} = -\frac{2\pi a}{P\sqrt{1-e^2}}\left[\sin f\hat{\imath} - (e+\cos f)\hat{\jmath}\right]. \tag{14}$$

With these relations in hand we can study the various detection methods and infer many important relations about the planetary orbit.

2.2 RADIAL VELOCITIES

The radial velocity technique is an indirect method to detect a planet. It exploits the Doppler effect to determine the orbital motion of a star around its stellar system barycenter due to the presence of one (or more) companion object. The Doppler effect states that the light emitted by a source that is approaching the observer is shifted towards shorther wavelengths. For a receding source the opposite stands. The simplest relativistic form of the Doppler effect is

$$z \equiv \frac{\lambda - \lambda_0}{\lambda_0} = \frac{1 + v_r/c}{\sqrt{1 - v^2/c^2}} - 1, \tag{15}$$

where λ is the observed wavelength, λ_0 is the wavelength at rest, v_r is the relative velocity of the source and the observer in the direction of the line of sight, v is the magnitude of the relative velocity, c is the speed of light, and z is called redshift.

Once every other possible phenomenon that causes a shifting in the absorption lines or a modification of their profiles has been removed, the Doppler shifts are converted in a radial velocity and interpreted as the motion of the star around the common barycenter of the stellar system.

We want to derive a set of equations that are indipendent from the orbital motion plane. A common choice is to transform the position and velocity vectors from the astrocentric reference frame to a modification of the Herschel astrocentric one (Beaugé et al., 2007) (see Fig. 1). The reference plane of this new system is the sky plane, where the x–axis is taken along the line of nodes and directed towards the γ point, the y–axis is tangent to the sky–plane and directed such as the resulting system is right–handed, and the z–axis is directed along the line of sight, and it points away from the observer. In this particular reference frame we fix $\Omega = \pi$. With 3 rotations it is possible to move from the astrocentric reference frame to the Herschel one, where the combined rotation matrix is

$$R = \begin{pmatrix} \cos\omega & \sin\omega\cos i & -\sin\omega\sin i \\ -\sin\omega & \cos\omega\cos i & -\cos\omega\sin i \\ 0 & \sin i & \cos i \end{pmatrix}. \tag{16}$$

Thus, by multiplying the velocity vector (eq. 14) in the old reference frame by the rotation matrix (eq. 16), we can rewrite the components of the relative velocity in the new reference system as

$$v_x = -\frac{2\pi a}{P\sqrt{1-e^2}}\left[\sin(f+\omega) + e\sin\omega\right] \tag{17}$$

$$v_y = \frac{2\pi a\cos i}{P\sqrt{1-e^2}}\left[\cos(f+\omega) + e\cos\omega\right] \tag{18}$$

$$v_z = -\frac{2\pi a\sin i}{P\sqrt{1-e^2}}\left[\cos(f+\omega) + e\cos\omega\right]. \tag{19}$$

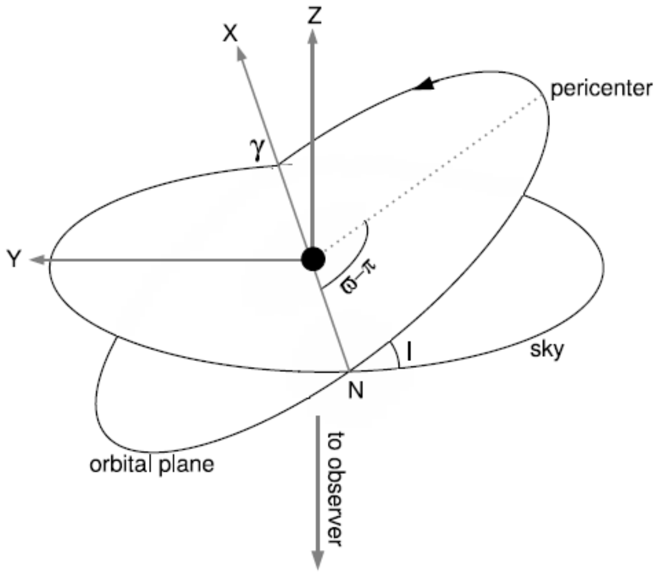

Figure 1: Herschel astrocentric reference system (Beaugé et al., 2007).

The radial velocity of the parent star, which is consider as a perturbation that a planet on a Keplerian orbit induces on his host star, can be derived from eqs. 19,3, 5

$$v_{z,\star}(t) = K[\cos(f(t) + \omega) + e\cos(\omega)] + v_{r,b}, \tag{20}$$

where $v_{r,b}$ is the barycenter radial velocity, and

$$K = -\frac{M_p}{M}\frac{-2\pi a \sin i}{P\sqrt{1-e^2}} = \frac{2\pi a_\star \sin i}{P\sqrt{1-e^2}}, \tag{21}$$

is a fundamental parameter since, noting that $v_{r,max} = (K + Ke\cos\omega)$ and $v_{r,min} = (-K + Ke\cos\omega)$, it is equal to

$$K = \frac{v_{r,max} - v_{r,min}}{2}, \tag{22}$$

so it is an observable and it is called the velocity semiamplitude.
From the observations we obtain a time series of radial velocities. As a preliminary step it is necessary to convert the time values in true anomalies through the eccentric anomaly E solving the classical Kepler equation iteratively

$$E - e\sin E = \frac{2\pi}{P}(t - T), \tag{23}$$

where T is the time of periastron, and

$$\tan\left(\frac{f}{2}\right) = \sqrt{\frac{1+e}{1-e}}\tan\left(\frac{E}{2}\right). \tag{24}$$

Thus, fitting the time series on the eq. 20 one can determine the set of parameters K, e, ω, T, P, and the barycenter velocity $v_{r,b}$. Once we determine this set of parameters, from eqs. 21, we could obtain an expression for the semimajor axis of the star

$$a_\star \sin i = \frac{\sqrt{1-e^2}}{2\pi} K P. \tag{25}$$

Furthermore, from the third Kepler's law

$$\frac{4\pi^2}{GM} = \frac{P^2}{a^3}, \tag{26}$$

and remembering eq. 5, we could derive an expression for the minimum mass of the planet

$$\frac{M_p^3 \sin^3 i}{M^2} = \frac{(1-e^2)^{3/2} K^3 P}{2\pi G}, \tag{27}$$

which is also called the mass function. Considering the planetary mass negligible respect to the stellar mass ($M_p << M_\star$) the minimum planet mass becomes

$$M_p \sin i \approx \left(\frac{P}{2\pi G}\right)^{1/3} K M_\star^{2/3} (1-e^2)^{1/2}, \tag{28}$$

and the semimajor axis of the relative orbit from the third Kepler's law (eq. 26)

$$a_p \approx \left(\frac{G}{4\pi^2}\right)^{1/3} M_\star^{1/3} P^{2/3} \tag{29}$$

Thus, from the fit of the radial velocity data with the Keplerian model we have derived 4 of the 6 orbital elements (i.e. a, e, ω, T). The longitude of the ascending node Ω (which was fixed) and the orbital inclination i remain unknown and it is necessary another detection method to completely solve the stellar orbit. When the stellar mass is known from stellar models, using eqs. 28,29, it is possible to derive an expression for the planetary mass and semimajor axis of the relative orbit. Although the true mass of the planet could in principle be very different from the minimum value derived, it has been shown that between the two values the following relation stands

$$M_p \leqslant 2 M_p \sin i \tag{30}$$

in 87% of the cases. For a planet in a circular orbit around a Solar–type star the value of the velocity semiamplitude is given by

$$K[m/s] \approx 28.57 M_p \sin i [M_{Jup}] P^{1/3} [yr]. \tag{31}$$

Since the probability to detect a planet depends on the value of the velocity semiamplitude, this expression teach us that the radial velocity method is more sensitive to massive short–period planets. To have an idea of the scale factor, Jupiter induces on the Sun a perturbation of the radial velocity with a semiaplitude of 12.5 m/s, while the Earth of 9 cm/s.

RADIAL VELOCITIES AND BINARIES Binary stars are generally discarded by target selection processes in radial velocity surveys, since they result in spectral contaminations (Martínez Fiorenzano et al., 2005).

Nonetheless, more than 50 planets orbiting binary stars have been discovered with the transit technique, altough in many cases the star binarity has been discovered after the planet detection since their semi–major axes are very high.

The most intersting case discovered with this method is indeed Gamma Chepei b (Hatzes et al., 2003). In effect, the binary has a quite close binary semimajor axis $a_B = 20$ AU, and $e_B = 0.439$, rendering the planet formation process challenging due to the tidal interaction of the companion star (see Chap. 5). The planet orbits the more massive component of the binary system with a semimajor axis $a = 2.05$ and $e = 0.049$.

2.3 TRANSITS

The most prolific indirect method of planet detection at the time of writing is the transit method. The physical principle at the basis of this technique is the transit of a planet across his host star, along the observer's line of sight (i.e. the line joining the observer with the light source), that causes a stellar flux variation.

GEOMETRIC PROBABILITY The necessary condition to observe a transit is that the projected separation on the sky plane between the planet and his host star is less than the sum of the star $R_\star$ and planet R_p radii (see Fig. 2)

$$\mathbf{r}(t)\cos i \leqslant R_\star + R_p, \tag{32}$$

where i is the inclination of the planetary orbit and $\mathbf{r}(t)$ is the position vector of the planet in the reference system centered on the star. Assuming that the eclipses are centered at conjunctions (i.e. close approaches between the star and planet centers along the line of sight), the true anomaly in a transit is given by (Winn, 2011)

$$f_{tra} = \frac{\pi}{2} - \omega, \tag{33}$$

where ω is the longitude of periastron. Thus, the impact parameter b, defined as the sky–projected distance at close approach in units of the stellar radius (see Fig. 3), is

$$b = \frac{\mathbf{r}(t_{tra})}{R_\star}\cos i = \frac{a}{R_\star}\frac{1-e^2}{1+e\cos f_{tra}}\cos i, \tag{34}$$

and from eqs. 32,33 we obtain

$$b = \frac{a}{R_\star}\frac{1-e^2}{1+e\sin\omega}\cos i \leqslant 1 + k, \tag{35}$$

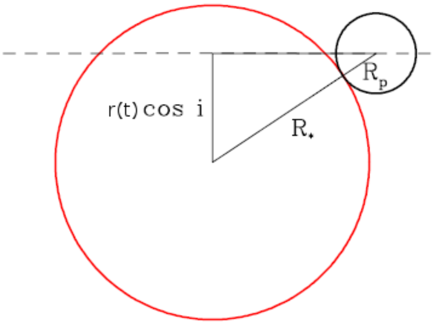

Figure 2: Geometry of a transit duration as viewed by the observer.

where $k = R_p/R_\star$ is the planet to star radius ratio. Hence, the maximum orbit inclination that allows a transit detection is

$$\cos i_{\max} = \frac{R_\star}{a}(1+k)\frac{1+e\sin\omega}{1-e^2}, \tag{36}$$

and assuming isotropic orbits, we can derive the probability to observe a transit by comparing the integral of $\cos i$ over the range of inclinations that permits a transit with the integral over all possible values (Sackett, 1999)

$$P_{tr} = \frac{\int_0^{i_{\max}} d(\cos i)}{\int_0^1 d(\cos i)} = \frac{R_\star}{a}(1+k)\frac{1+e\sin\omega}{1-e^2}, \tag{37}$$

which, for a circular orbit ($e = 0$) and assuming that the star is much more massive than its planet ($k \sim 0$), simplifies as

$$P_{tr} = \frac{R_\star}{a}. \tag{38}$$

TRANSIT DURATION We can divide the eclipses in two main types:

1. full eclipses, when the stellar and planetary disks, as viewed from the observer point of view (POV), are tangent at four contact times (t_I,t_{II},t_{III},t_{IV} as in Fig. 3)

$$|b| \leqslant (1-k), \tag{39}$$

2. grazing eclipses, when the stellar and planetary disks are tangent at two contact times (t_I,t_{IV} only)

$$(1-k) < |b| \leqslant (1+k). \tag{40}$$

Thus, we can define a total duration of the eclipse as $T_{tot} = t_{IV} - t_I$, a full duration as $T_{full} = t_{III} - t_{II}$, and an ingress and egress durations τ (see Fig. 3). The total duration can be derived geometrically, for the circular case ($e = 0$), considering that it is equal to the interval of the orbital period P during which eq. 35 is satisfied. Hence, given that the

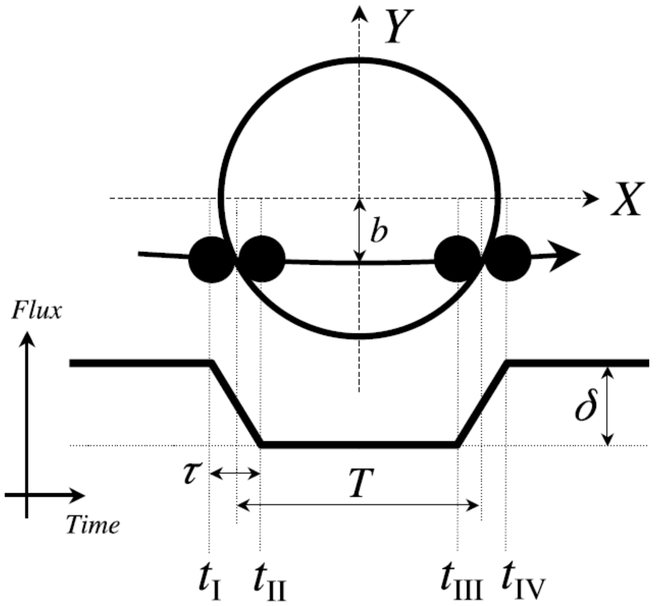

Figure 3: Schematic illustration of a transit, showing the four contact points, the transit time duration, and the idealized light curve (Winn, 2011).

angular velocity of the planet is $P/2\pi$ and the portion of orbit during which there is a transit is

$$\theta_{\mathrm{tot}} = 2\arcsin\left(\frac{R_\star}{a}\frac{(1+k)^2 - b^2}{\sin i}\right), \tag{41}$$

the total duration of the transit will be

$$T_T = \frac{P}{2\pi}\theta_{\mathrm{tot}} = \frac{P}{\pi}\arcsin\left(\frac{R_\star}{a}\frac{(1+k)^2 - b^2}{\sin i}\right), \tag{42}$$

while the full duration of the transit, from eq. 39, is

$$T_F = \frac{P}{\pi}\arcsin\left(\frac{R_\star}{a}\frac{(1-k)^2 - b^2}{\sin i}\right), \tag{43}$$

For eccentric orbits, we have to multiply eqs. 42– 43 by a scaling factor given by Winn (2011)

$$\alpha_{\mathrm{ecc}} = \frac{\sqrt{1-e^2}}{1+e\sin\omega}. \tag{44}$$

It is noteworthy that in the limiting case of a near circular orbit for $R_p << R_\star << a$, $M_p << M_\star$, and excluding grazing eclipses ($b << (1-k)$) the total transit duration simplifies as

$$T_{\mathrm{full}} = T_0\sqrt{1-b^2}, \tag{45}$$

where

$$T_0 \equiv \frac{R_\star P}{\pi a} \approx 13\mathrm{hr}\left(\frac{P}{1\mathrm{yr}}\right)^{1/3}\left(\frac{\rho_\star}{\rho_\odot}\right)^{-1/3}. \tag{46}$$

So, we could also derive an hint about the stellar mean density from the transit analysis.

LOSS OF LIGHT DURING ECLIPSES Concerning the flux evolution during a transit event, we could define 3 different stages.

1. **Transit**. When the planet crosses his parents star, from the observer POV, the flux received $F(t)$ decreases because the planet blocks a fraction of the starlight proportional to the ratio of their radii k (Winn, 2011)

   $$F(t) = F_\star(t) + F_p(t) - k^2 \alpha_{tr}(t) F_\star(t), \tag{47}$$

   where $F_\star$ and F_p are the stellar and planetary fluxes, α_{tr} is a dimensionless function of order unity which accounts for the overlap area between the planet and star disks. Fining our analysis we must take account of the limb darkening effect, due to the difference of the star luminosity between the center and the edge (limb). This happens because in the limbs the line of sight enters with an oblique angle in the stellar atmosphere, reaching at a higher altitude an optical depth of unity, where the temperature and stellar radiation are lower. The net effect in the light curve is to blur the second and third contact points, and round the flat bottom part. Moreover, studying the flux evolution in the flat part it is possible to detect stellar variations due to its superficial activities.

2. **Outside eclipse**. When the planet leaves the star disc and before it is occulted by the star, the flux raises because it is given by the sum of the star and planet fluxes

   $$F(t) = F_\star(t) + F_p(t). \tag{48}$$

   Moreover, there is a continuous increase of flux in this phase because, as the planet orbits around his star, it reveals an increasing fraction of its day–side face. On the other hand, when the planet approaches the transit there is a slow continuous flux decrease as the night–side face of the planet become visible.

3. **Occultation**. When the planet is occulted by the star the flux drops because of the missing planet flux. However, in a grazing eclipse a fraction of the planet disc could remain visible

   $$F(t) = F_\star(t) + F_p(t) - \alpha_{occ}(t) F_p(t), \tag{49}$$

   where again α_{occ} is a dimensionless function of order unity.

A major result from the transit analysis is that, if the planetary night-side is negligible, the maximum loss of light is (Winn, 2011)

$$\delta_t \sim k^2. \tag{50}$$

All in all, from the transit technique we can derive fundamental informations such as the planet to star radius ratio (eq. 50), the impact parameter b and rescaled star radius $R_\star/a$ from the total and full durations of the transit (eq. 42, 43), the orbital inclination (eq. 35), and a hint about the star density (eq. 46).

However, in order to obtain some informations about the planetary mass it is necessary to perform a radial velocity follow–up and derive it from the semiamplitude velocity K (eq. 28).

Moreover, to better constraint the planetary and mass radius it is necessary to refine the stellar values. In this context the astroseismology is fundamental to obtain high precision values of the star mass and radius.

We will analyze in more detail in the next chapters the major planetary detection around binaries with this method.

2.4 TIMING

The timing technique has been used to detect the first exoplanets (Wolszczan and Frail, 1992), orbiting around a pulsar. It is based on the detection of a time variation to a regular, periodic photometric variability. The regular phenomena could be of various types such as a pulsar or a pulsating star, but the most interesting ones for our porpouse are eclipsing binaries and stars with a transiting planet. This time variations could be observed as a additional Doppler shift, light–travel time, and gravitational perturbations.

This technique has been employed successfully to detect pulsars and eclipsing binary systems for a long time. Noteworthy, the precision reached in the planet detection around pulsars is stunning (of the order of the Moon mass), due to the very high precision of the pulsar period.

Concerning the detection of additional planets in a planetary system or new planets in a binary star system, from transit time variations, there have been great progresses in recent years with the Kepler mission (Ford et al., 2012). This method is called transit timing variations (TTV) (Holman and Murray, 2005; Agol et al., 2005), and it allows the orbital period and mass determination of the perturber from transit detections alone.

The time interval between two succesive transits of an unperturbed planet is constant over time, expect for small corrections due to orbital precession.

However, if a second planet is present in the system, their mutual gravitational interaction will produce an energy and angular momentum exchange, which in turn alter the interval between consecutive transits. As an example, considering our Solar System, Mercury would have a TTV of tens of seconds, while Mars of thousends of seconds (Holman and Murray, 2005).

Given a transiting planet with a semimajor axis and period a_1, P_1 and a external perturbing planet with semimajor axis $a_2 > a_1$, period P_2, and mass M_2, the magnitude of the interval variation is (Holman and Murray, 2005)

$$\Delta t \simeq \frac{45\pi}{16}\left(\frac{M_2}{M_\star}\right) P_1 \alpha_e^3 (1-\sqrt{2}\alpha_e^{3/2})^{-2}, \tag{51}$$

where $\alpha_e = a_1/[a_2(1-e_2)]$, in the approximation that the external perturber follows a parabolic orbit with periastron distance of $a_2(1-e_2)$, which is valid for $e_2 \geqslant 0.3$. Thus, it is simpler to derive the TTV for systems where the transiting planet is in the external zone $(P_1 >> 1)$, and for less massive stars $M_\star$.

Moreover, the eccentricity of the external perturber $e_2$can be estimated comparing the relative magnitudes of the time variations $\Delta t_{max}/\Delta t_{min}$, and if its period is much greater than that of the inner planet the previous equation semplifies, giving an estimate of the perturbing planet mass (Holman and Murray, 2005)

$$M_2 \simeq \frac{16}{45\pi} M_\star \frac{\Delta t_{max}}{P_1}\left(\frac{P_2}{P_1}\right)^2 (1-e_2)^3. \tag{52}$$

When the planets are in mean–motion resonance, the transit time variation is enhanced due to a stronger gravitational interaction between them.

The TTV may be the only possibility to determine the mass and density of planets orbiting faint stars, for which a radial velocity measurement is unfeasible, and in effect it was successfully applied to characterize a sample of the Kepler planet candidates (Ford et al., 2012)

2.5 ASTROMETRY

The astrometry technique is based on the measurement of the wobble induced by the planetary companion on his host star, projected on the sky plane. For a star–planet system at a distance d (pc), with mass ratio q, and planetary semimajor axis a (AU), the star semimajor axis $a_\star$ is given by eq. 5, and the star center displacement in milliarcseconds (mas) during an orbital period is

$$\theta = \frac{a_\star}{d} = q\frac{a}{d}. \tag{53}$$

Thus, the astrometry method is ideal to find long period planets $(a >> 1)$ at a close distance d. Therefore, it is complementary to the radial velocity method which is biased for short period planets.

Moreover, astrometry measures 2 independent components of the orbital motion projected on the sky plane, better characterizing the orbital parameters.

To have an idea of the magnitude of this event, if we were observing the Sun from a distance of 10 pc, then the wobble induced by Jupiter would have an amplitude of $\theta = 500$ mas, while that induced by Earth $\theta = 0.3$ mas. Since the precision obtained from ground based facilities is on the order of 1 mas, it is necessary to use space missions to detect terrestrial planets. GAIA, the astrometry ESA space mission, launched at the beginning of 2014, will have a precision of ~ 20 mas at 15 visual magnitude, thus it would be able to detect super–Earths.

At the time of writing there are only two planets detected via this method, but the future GAIA mission could improve a lot this sample.

ASTROMETRY AND BINARIES Although the exoplanet research via astrometric detection is at its first phases, there is a long history of astrometric binaries detected via this method from ground base facilities.

Moreover, astrometric planetary surveys from ground based facilities target preferentially close binaries, in order to obtain a better resolution with differential astrometry. In effect, one of the two planet candidates discovered with this technique, HD 176051 b, is hosted by a binary star system with a S type orbit (around one of the components), an expected mass of $2.26 M_J$ and a semimajor axis $a = 2.02$ AU (Muterspaugh et al., 2010).

2.6 GRAVITATIONAL MICROLENSING

The gravitational microlensing is a relativistic effect which consists in a deflection of a photon that passes close by to a mass (Einstein, 1936; Refsdal, 1964). This effect was the first experimental prove of the Einstein's relativity theory.

The deflection angle is

$$\alpha = \frac{4GM_\star}{bc^2}, \tag{54}$$

where b is the impact parameter, and c is the light speed. When a foreground star (lens) passes in front of a background star (source) along the same light of sight, the image of the source is distorted into a ring. This distortion is due to the different impact parameters of the source photons passing nearby the lens, which lead to distinct deflection angles. The radius of the Einstein ring of a source at a distance d_S passing along the line of sight of a lens at a distance d_L and a mass M_L is

$$R_E = \frac{2}{c}\sqrt{\frac{GM_L d_{LS}}{d_L d_S}}, \tag{55}$$

where d_{LS} is their relative distance. The axial simmetry of the distorted figure is broken when the alignment is not perfect, and it results in multiple images with an angular distance from the lens again of the order of R_E .

A peculiar property of the microlensing effect is that the surface brightness of the magnified source is conserved, so the resulting star flux reaching us is increased. The maximum of the stellar flux coincide with the perfect alignment of the source and the lens.

The majority of the distorted star figures due to the microlensing effect can't be resolved from ground–based facilities. However, in order to find unresolved lenses it is sufficient to detect stars whose flux change with time by several orders of magnitudes in a period of time $t_E = R_E/\mu$, where μ is the relative motion between the lens and the source. The period t_E of the source magnification is of the order of 1 month for galactic bulge stars.

If the lens harbours a planet with a semi–major axis that is close to the source Einstein ring, even its tiny gravity can induce an additional microlensing effect to the photons passing nearby. This event could be detected as an additional blip in the light curve of the magnified source. The time scale of this event depends on the planet to star mass ratio $t_P = q^{1/2} t_E$, which is of the order of 1 day for a Jupiter mass planet and of 1 hr for an Earth mass planet. Considering a galactic bulge source and a disk lens, the semi–major axis of the planet that could generate a microlens effect is of a few AU.

The major advantage of this method is the possibility to detect small planets down to the Earth size with no particular effort, since there is a poor dependance of the event period on the planetary mass $t_P \propto q^{1/2}$. However, in order to detect such a signal it is necessary to continuosly monitor millions of stars, and it very unlikely to observe a second magnification event for a particular star. Furthermore, in most of the cases, the planetary properties could be estimated only on a statistical bases, due to the great amount of parameters that influence this event. Nonetheless, it is possible to obtain better constraints on planetary properties when the lens and source stars separates from our point of view and they can be studied separately.

MICROLENSING AND BINARIES The number of confirmed planets detected with this method is 26 in 24 planetary systems. Although many cases of lenses due to binary stars have been observed, there haven't been any detection of planets orbiting those systems. When the lens is a binary star, the magnification pattern is more complex than usual forming a so called caustic figure, and resulting in an enhanced magnification event (see e.g. Rattenbury (2009)).

2.7 IMAGING

We have analyzed the most succesfull indirect detection method. However, it is now become possible to detect directly the planet light for

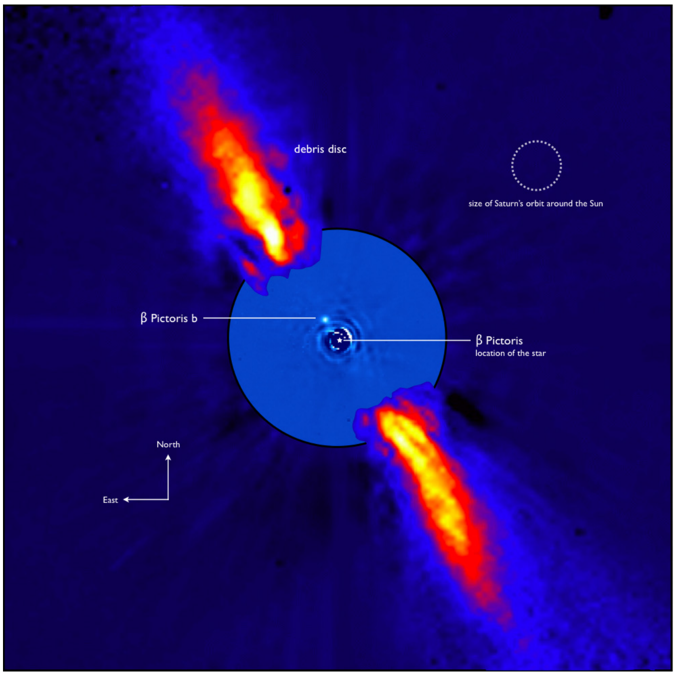

Figure 4: Direct image of the giant planet orbiting the star beta Pictoris (ESO).

a particular class of giant planets orbiting the outer zones of their planetary systems. The great difficulties in the direct detection of exoplanets are due to the extreme contrast between the planet and its host star. In fact, the fraction of the starlight reflected by an Earth–like planet is

$$f = \left(\frac{\pi R_p^2}{4\pi a^2} \right) \sim 10^{-10}, \tag{56}$$

corresponding to 24–25 magnitudes fainter than its host star (Armitage, 2010). The situation is a little bit better in the infrared where we consider their thermal emission $f \sim 10^{-6}$, but the telescopes needed to detect it are considerably greater.

The direct detection of close Earth–like planets is thus almost impossible with the current technologies. Yet, it could be of great importance in order to characterize possible habitable planets and detect life signatures.

There have been discovered almost 20 giant planets with this technique at the time of writing, and there are many efforts to improve this sample via specially designed ground based instruments such as the VLT–SPHERE.

The best example of the direct imaged planets is Beta Pictoris b (Lagrange et al., 2010), which is a giant planet $M \sim 4\text{–}11\ M_J$ with a semi–major axis of 8–9 AU and its host star is a young $1.75M_\odot$ A6V star (see Fig. 4).

IMAGING AND BINARIES The direct–imaging of planets in circumbinary orbits is challenging only for resolved close binaries due to optical problems. Otherwise, it is feasible for spectroscopic binaries. Nonetheless, only recently it has become possible to detect planets with this method and at the time of writing there are no planets detected in binary systems.

3

SPACE MISSIONS DEVOTED TO PLANET DETECTION

3.1 INTRODUCTION

Since the detection of the first extrasolar planet orbiting a pulsar (Wolszczan and Frail, 1992), and the discovery that they are present in every stellar environment, a huge interest has spurred in the scientific community for their detection and characterization. Although the first detections were made only from ground–based facilities, the whish to detect Earth analogues has lead to the planning of dedicated space missions.

The first space mission devoted to exoplanetary research was the French mission CoRoT (COnvection, ROtation and planetary Transits) (Baglin et al., 2006), launched on December 2006 in collaboration with several European countries. It used the transit method (see Sec. 2.3), discovering more than 20 confirmed exoplanets, and hundreds of candidates, laying the foundations for future space missions.

However, the mission that really took a leap forward was the NASA mission Kepler (Koch et al., 2010), which discovered more than 240 confirmed exoplanets including 7 circumbinary planets, and more than 3500 planet candidates, with the transit method.

For the next generation of space mission, ESA has scheduled CHEOPS, which is a small class mission aiming to better characterize the stellar systems were a planet has already been discovered. Moreover, NASA has planned TESS, which is also based on the transit method and will survey a great portion of the sky, searching for planets down to Earth analogues orbiting bright Solar–type stars with a small period. Furthermore, in the beginning of 2014, the ESA mission GAIA will start to detect and fully characterize nearby stars with a huge survey using the astrometry method. With these observations it will be possible also to detect their potential wobbling due to the presence of a planet. Finally, ESA has proposed a space mission, PLATO, with the goal of detecting exoplanetary systems in a wide range of orbital parameters, orbiting brigth stars with a great survey that will cover nearly half of the sky. The University of Padova is deeply involved with the CHEOPS and PLATO space mission, collaborating both from a technical and scientific point of view.

In these chapter I will briefly summarize the main characteristic of the Kepler mission, and the future planned/proposed missions where our University is involved, highlighting their possible contribution to the discovery of planets orbiting binary systems.

Figure 5: Rendering of the Kepler spacecraft. Credit: NASA/Ames/JPL–Caltech.

3.2 KEPLER

Kepler is a spacecraft launched by NASA on March 2009 with the major scientific goal of determining the frequency of Earth–like planets in and near the habitable zone of Sun–like stars, using the transit technique.

MISSION DESIGN The signal produced by an Earth–Sun analog during a transit is a dimming proportional to its area. In order to detect such an event we need to take account of the noise sources given by the shot noise, stellar variability and measurement noise. (Koch et al., 2010) found that the measurament noise needed to detect an Earth–Sun analog must be of the orther of 10 ppm, which is almost 100 times better than the actual possibility from ground–based facilities.

The Kepler team obtained this precision with an accurate selection of the photometer and the observational strategy.

The targeted stars were selected in a single wide Field Of View (FOV) with a diameter of 16° and a Sun avoidance angle of 55°. The advantages of this approach are various both from a technical and a scientific point of view. On the one hand it simplifies the spacecraft design, maximizing the duty cycle and simplifying the data–handling operations. On the other hand, it permits to minimize the necessary stellar classification and obtain a continuous asteroseismic measurements over a long period of time (Koch et al., 2010).

Furthermore, it allows to detect planets with large periods, improve the photometric precision for known planets decreasing the minimum detectable size, and increase the probability of finding unseen companions via transit timing variations (TTV).

A preselection of the stars was made so as to avoid giant stars, since their stellar size and variability reduces the possibility to detect small planets, with a ground based multi–band photometric survey that creates the Kepler Imput Catalog (KIC) (Brown et al., 2011).

The orbit chosen for the spacecraft is an Earth–trailing heliocentric orbit which has some crucial features that render it ideal for precise photometry respect to a low–Earth orbit as pointed out by Werner et al. (2004) for the SPITZER mission and Koch et al. (2010).

The photometer consists in a modified Schmidt telescope design with a 1.4 m diameter f/1 primary mirror and a corrector with a 0.95 m aperture coupled with an array of 42 CCDs. The large FOV required to maximize the scientific output needed a curved focal surface coupled with field–flattening lenses. The core of the photometer is the 95 megapixel focal plane formed by 42 science CCDs and 4 guidance sensor CCDs, each of which has an area of 50 × 25 mm covered by 2200 × 1024 pixels.

The images are defocused to 10 arc seconds so as to improve the photometric precision and the CCDs are read out every 6.02 seconds. In order to minimize the downlink (once a month) there have been selected two main data sets. The long cadence set consist in the integrated pixels of interest (POI) for each selected star every 270 readouts (30 minutes), which are extracted from the image, compressed and stored. This data set is used mainly for planet detection. The short cadence set is formed by a selection of 512 POI, which are extracted every minute, with the aim of improving the timing of planetary transits and perform asteroseismology (Caldwell et al., 2010). Finally, once per month a full–field image is recorded, calibrated and archived.

This mission ended in 2013 after having successfully discovered more than 240 confirmed planets and more than 3500 planet candidates in a great variety of configurations. The major drawback of this mission is that the great majority of the planet candidates are not going to be confirmed in the near future, since the precision needed for a follow–up survey is very challenging.

3.2.1 *Kepler and planets in binaries*

One of the many astonishing discoveries made by the Kepler mission was the class of circumbinary planets. Here we will briefly present the best cases of this sample.

3.2.1.1 *Kepler–16*

Kepler–16 (Doyle et al., 2011) was the first circumbinary planet discovered. It orbits near the dynamical stability region ($a_p = 0.705$ AU) of a close binary system ($a_b = 0.224$ AU, $e_b = 0.16$) formed by a $0.69 M_\odot$ K–type main–sequence star and a $0.20 M_\odot$ M–type red dwarf at 60 pc from us. It is a Saturn–like planet ($M_p = 0.333 M_J$) and it orbits slightly outside the circumbinary habitable zone (Welsh et al., 2013).

3.2.1.2 *Kepler–47*

Kepler–47 (Orosz et al., 2012b) was the first circumbinary multi–planetary system discovered. The binary is formed by a Solar–like star and a $0.3M_{\odot}$ star with a period of 7.45 days and a semimajor axis of 0.08 AU. The inner planet is a gas giant with a semimajor axis of 0.296 AU, while the outer is a Super-Earth planet with $a = 0.989$ AU. A major point of this system is that the outermost planet is just inside the calculated habitable zone of the binary system (Welsh et al., 2013).

3.3 GAIA

Gaia is an astrometric mission funded by ESA and launched at the end of 2013, with the ambitious goal of making the largest, most precise, 3D map of our Galaxy.

MISSION DESIGN The core of the spacecraft is based on a dual telescope concept, sharing a common structure and focal plane. The optic of the two telescopes is identical, and consists in a three-mirror anastigmat (TMA) design. The beams coming from the two telescopes are then combined in image space with a small beam combiner, and reach a large focal plane with an array of 106 CCDs. The GAIA design is multipurpose since it could perform astrometric operations, with accurate measurements even in high density star regions, photometric operations, with continuous spectra in the band 320–1000 nm, and high resolution spectrometry.

SCIENTIFIC OBJECTIVES Gaia will measure very accurately the motion of nearby stars around the centre of the Galaxy, constraining their birth places and so the Galactic formation scenario.

Concerning exoplanets, its astrometric measurements will confirm the existence of Jupiter sized planets, discovered via RV method. Moreover, it will be capable of detecting the inclination of orbital planes with high precision, better constraining the planet mass for known systems. Gaia will also be able to detect new exoplanets with the astrometric and transit method, since it will observe one billion sources about 70 times, recording their position and brightness over time. Furthermore, the huge quantity of data derived by Gaia will be of paramount importance to the target selection of future space missions such as CHEOPS or PLATO.

Concerning binaries, Gaia, with its high precision ($\sim 20mas$), will increase drastically the parameter space of known astrometric binaries, that can be a prime target for circumbinary planets searches.

3.4 CHEOPS

CHEOPS (CHaracterizing ExOPlanet Satellite) will be the first ESA mission dedicated to exoplanet research with the transits method and its launch is planned for 2017. Its peculiarity is that it will be the first follow–up space mission, since its main targets are bright stars ($m_V < 13$) already known to host planets by current and near future ground–based spectroscopy surveys.

MISSION DESIGN The spacecraft design is characterized by its small form factor and the onboard 33.5 cm diameter, f/8, on–axis Ritchey–Chrétien telescope coupled with a single back–illuminated CCD detector with 1024^2 pixels of 13 μm size mounted on its focal plane.

CHEOPS, in order to achieve its scientific goals, needs a precision of 150 ppm/min for a $m_V = 9$ star, which corresponds to the effect of an Earth–sized planet transiting in front of a 0.9 $R_\odot$ star with a period of 60 days, detected with a S/N> 10 for a 100 ppm transit depth.

The spacecraft orbit will be Sun–synchronous with an altitude of 800 km that permits the spacecraft to be pointed permanently in the opposite direction of the Sun. This choice allows uninterrupted observations and reduces the spacecraft thermal variations. The mission duration necessary to complete the proposed core programme is 3.5 years.

SCIENTIFIC OBJECTIVES The main scientific goal of this mission is to study the structure of exoplanets in the super Earth and Neptune mass range. In particular, it will determine the mass–radius relation with an unprecedent precision (10% or better) in a mass range where data lacks, providing better understanding of planet migration during the planet formation and evolution phase. Moreover, it will identify the presence of a significant planet atmospheres, detect potential planetary systems, and provide informations about the energy flux in hot Jupiters atmospheres.

This mission design has two main advantages. On the one hand, respect to random searches performed by CoRoT and Kepler, CHEOPS will know when and where to look, so it will be extremely more efficient. On the other hand, such a scientific goal is achieved with a less expensive small class mission design, since it focuses only on bright stars.

3.5 TESS

TESS (Transiting Exoplanet Survey Satellite) is a space mission devoted to exoplanet detection with the transit method, part of the NASA's Explorer program, that will be launched in 2017.

Its main goal is the detection of small planets orbiting bright host stars in the solar neighborhood, so that detailed characterizations of their bulk and atmosphere properties is feasible. Moreover, it will be capable of detecting planets ranging from Earth-sized to gas giants, orbiting a wide range of stellar types and orbital distances up to a period of $\sim$ 20 days.

MISSION DESIGN TESS lifetime is about two years, during which it will monitor the brightness of more than 500000 stars in the full celestial sphere, expecting more than 3000 planet candidates, including $\sim$ 500 Earth and Super Earth planets, down to the habitable zone.

The core of the spacecraft consists in four wide–angle telescopes. and an array of CCD with 67 megapixels.

The observation strategy consists in “stare and step" phases, with a FOV of $24^{\circ} \times 96^{\circ}$ and a period of 27 days, after which the cameras are stepped by 27 degrees. The spacecraft will be in a High–Earth Orbit (HEO) in a 2:1 resonant orbit with the moon, which provide a very stable environment.

3.6 PLATO

The PLATO 2.0 space mission (PLAnetary Transits and Oscillation of stars) is the next major ESA mission with the scientific goal of detecting terrestrial exoplanets in the habitable zone of nearby Solar–type stars in a wide FOV, and characterizing their bulk properties.

It was originally proposed in 2007 as a medium class candidate for a launch in 2017–2018. After it was discarded by ESA in October 2011, it was reproposed as a candidate for the launch opportunity in 2022–2024 with a significant revision of the mission science case in order to account for the recent discoveries in exoplanetology and the challenges of the next decade.

To reach its objective it will combine planet detection and radius determination from photometric transits, and accurate stellar mass, radii and ages from asteroseismology, performed by the PLATO spacecraft, with planet mass determination from radial velocity follow–up made by ground based facilities. Moreover, the identification of bright targets will be foundamental to study planet atmosphere composition. It is to point out that a great improvement in the PLATO efficiency will be due to GAIA, that will provide an high precision characterization of the complete set of stellar parameters for bright targets ($m_V \leqslant 11$). PLATO will in turn use these data to minimize false positives and follow–up analysis, select the most promising cases for the target selection, and better constraint the parameter space of detected planets.

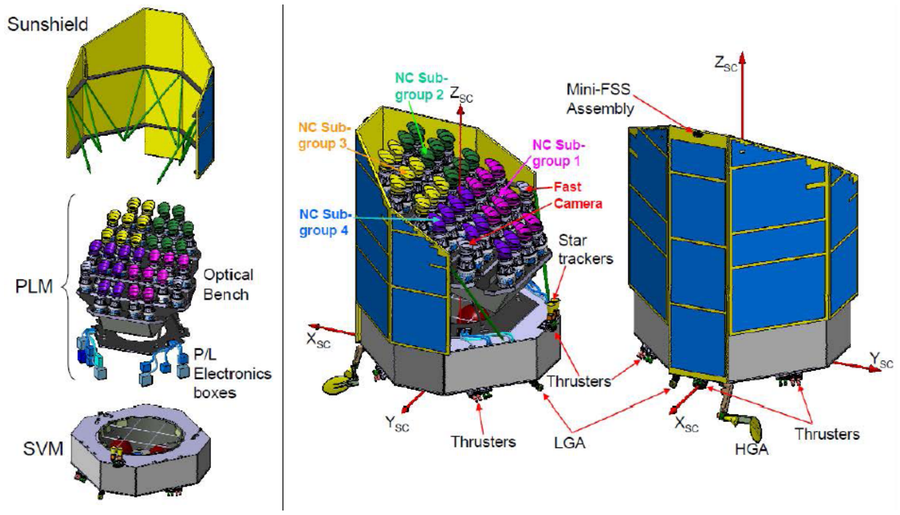

Figure 6: PLATO spacecraft configuration and external equipment layout. Credit: ESA

In this way, it will create the first catalogue of confirmed and characterized habitable planets, with known mean densities, ages, and atmosphere composition.

MISSION DESIGN The instrument needed to achieve these goals must have a wide field of view, due to the scarsity of bright stars, and an high sensitivity. The design selected solves this requirements adopting 32 "normal" telescopes (see Fig. 6), each of which composed by a fully dioptric design camera with 6 lenses, a FOV of 1100 deg^2, and 4 CCDs with 4510^2 pixels of 18μm size.

The CCDs on the focal planes will be readout every 25 s to observe stars with $m_V > 8$. Instead, brighter stars with $4 < m_V < 8$, will be readout with an higher frequency (every 2.5 s) by 2 additional "fast" cameras. The normal cameras are divided in 4 groups with the same FOV, but with a little offset of 9.2°, to obtain a total FOV of 2250 deg^2 per pointing with different sensitivities over the field (see Fig. 7).

The observing plan consists of a combination of 2 long–term target fields that will be observed for 2–3 years each, and a step–and–stare phase to cover the most interesting targets over a large region for up to 5 months per field. The spacecraft will be placed in the Sun–Earth system lagrangian point L2, and its lifetime is about 6 years. During this perios it would be able to observe nearly half of the sky.

SCIENTIFIC OBJECTIVES The real step forward of this mission will be its ability to determine the bulk properties and atmospheres of a huge variety of extrasolar planets. With this information it would be possible to characterize Earth–like planets, and determine the frequency of our Solar System architecture. Moreover, constraining stellar ages with asteroseismology analysis, PLATO will photograph the

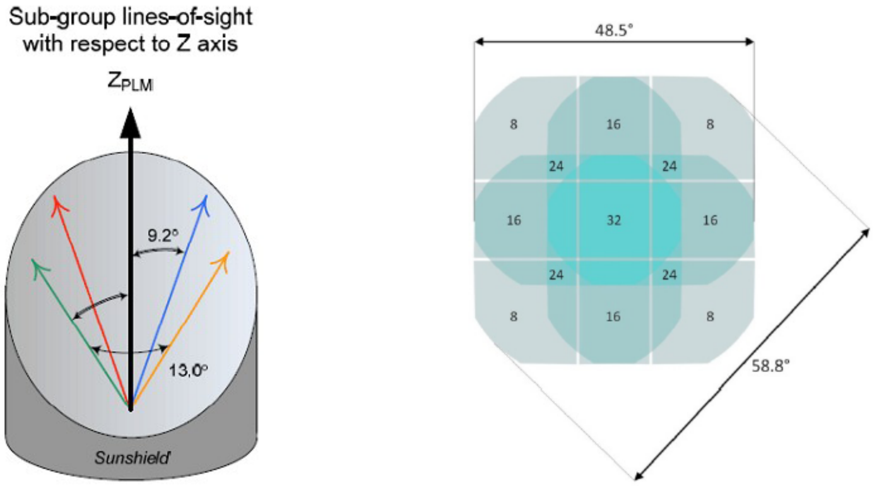

Figure 7: In the left panel we can see the overlapping line–of–sight configuration that results in a different coverage of the field–of–view (right panel). Credit: ESA.

planetary systems at different stages of planet formation and evolution, giving us fundamental hints on how these processes evolve with time and how they depend on the physical environment. The prime goal of detecting an Earth–like planet could be achieved in bright stars ($4 \leqslant m_V \leqslant 11$) thanks to spectroscopic transits follow–up observations that will inspect the planet atmosphere, constraning their habitability.

Concerning planets in binary star systems, PLATO will increase their statistics dramatically, observing a complete sample of bright stars, thus reducing the selection and bias effects in their sample. Moreover, with the fundamental aid of GAIA that will characterize the parameter space of astrometric binaries up to a separation of 20 mas, it will be much more efficient than Kepler in detecting circumbinary planets, not being limited to eclipsing binary targets.

Finally, PLATO could prove the observed trends in the statistical analysis of planets in binaries, such as the circumbinary planets packing near the inner dynamical stability limit, the dearth of planets orbiting very tight binaries, and the difference in mass and eccentricity distribution of circumstellar planets respect to those in single star configurations. (see Chap. 4).

3.7 CONCLUSIONS

The major problem with recent exoplanet space missions (e.g. CoRoT and Kepler) is that they selected faint target stars, for which an accurate measurement of planet physical parameters is not feasible in the near future by follow–up campaigns. CHEOPS mission is the first response to this major problem, focusing only on bright stars were a planet has already been detected, and the next scheduled space missions are all going to target bright stars.

Concerning binary star systems, we have now a growing sample of detected planets both in S–type and P–type orbits, and we are improving our knowledge on planet formation processes in these complex scenarios. Thus, we have the capability to better constraint the configurations where a planet could be detected. In this context, CHEOPS could provide more interesting cases from the analysis of known planetary systems orbiting binaries in a wider parameter space. While, PLATO could really take a leap forward in the detection of planets in binaries, improving greatly their statistics, and reducing the observational bias present in current data.

Part II

STATISTICAL PREDICTION OF PLANETARY SYSTEM ARCHITECTURES

4

INFLUENCE OF BINARY STARS IN A TRANSIT SPACE MISSION

4.1 INTRODUCTION

Observational surveys and numerical experiments of star formation suggests that the majority of Sun–like stars form in multiple systems, and nearly half of them are currently found to be member of a binary star (Parker and Quanz, 2013; Raghavan et al., 2010; Duquennoy and Mayor, 1991). This difference is probabily due to gravitational interactions in relatively dense cluster environments, which could break loosely bounded binary systems (Kroupa, 1995).

Since the majority of stars form in binary systems, estimating the frequency of planets in these environments is then a relevant issue when computing the fraction of stars hosting planets. In effect, it is of paramount importance both from a theoretical point of view, since it shows the footprints of planet formation and evolution processes, and from a observational point of view, in order to select the best target fields for a space mission devoted to planet detection in a wide FOV, such as PLATO.

In this chapter, I review the current observational data about stellar multiplicity, and the main differences between planet properties in multiple stellar systems compared with those orbiting single stars observed so far. Then I present a statistical analysis of the impact of binaries in a putative field of the PLATO mission.

4.2 KEY PROPERTIES OF STELLAR MULTIPLICITY

There are two main parameters that define the multiplicity property of a stellar population: the multiple system frequency (MF) and the companion frequency (CF). The first one describe the fraction of stellar systems that have more than one component, the latter indicates what is the frequency of companions per target. Considering Solar–like stars as those with a mass $0.7M_\odot < M_\star < 1.3M_\odot$, and a spectral type between F and mid–K, Raghavan et al. (2010) found that the mean $\text{MF} = 44 \pm 2\%$ while $\text{CF} = 62 \pm 3\%$, so the majority of field Solar–type stars are in a single configuration. However, those parameters depend strongly on the primary mass. In fact, limiting their sample only to $1.0M_\odot < M_\star < 1.3M_\odot$, Raghavan et al. (2010) found that $\text{MF} = 50 \pm 4\%$ and $\text{CF} = 75 \pm 5\%$, thus stars in single and multiple configurations are almost equal. On the other side, low mass stars ($0.1M_\odot < M_\star < 0.5M_\odot$) have $\mathrm{MF} = 26 \pm 3\%$ and $\mathrm{CF} = 33 \pm 5\%$ (Delfosse et al., 2004; Dieterich et al., 2012).

Mason et al. (1998); Metchev and Hillenbrand (2009) also suggested that the number of visual binaries for young Solar–type stars (0.1–1 Gyr) is greater than the older counterpart, implying an age–dependance of the stellar multiplicity but, as stated by Duchêne and Kraus (2013), we do not have unbiased surveys to surely confirm this trend.

The multiple systems could also be described by their key physical parameters, such as their period, mass ratio and eccentricity. The orbital period P could be directly measured for spectroscopic binaries and visual binaries. For visual binaries with long period, it could also be estimated from the projected separation on a statistical basis. The parametrization that better describe the orbital period is a log–normal distribution (Heacox, 1996; Duquennoy and Mayor, 1991; Raghavan et al., 2010)

$$f(\log P) = C \exp \frac{-(\log P - \overline{\log P})^2}{2\sigma^2_{\log P}}, \tag{57}$$

where C is a constant, $\overline{\log P} = 4.8$, $\sigma_{\log P} = 2.3$, and P is measured in days.

The mass ratio q is generally well described by a power law

$$f(q) \propto q^\gamma, \tag{58}$$

where $\gamma = 0.28 \pm 0.05$ for Solar–type stars (Duchêne and Kraus, 2013), but there is a marked difference between long period ones with a peak at $q \approx 0.3$ and short period binaries with a maximum at $q \approx 1$.

The orbital eccentricity e is an important parameter to understand the dynamical evolution of a system. Binaries with short orbital period P have generally a very low eccentricity due to tidal dissipation (Koch and Hrivnak, 1981). Meanwhile, in multiple systems, a third inclined perturber can pump up the orbital eccentricity (due to Kozai resonance, see Sec. 8.3.2).

4.3 PLANETS IN BINARY STAR SYSTEMS

Although the number of known planets orbiting binary and multiple star systems is significantly lower than that orbiting single star, it is interesting to study statistically the properties of those systems in order to derive some differences in planet formation and evolution processes, and thus constrain the parameter space where a planet could be observed.

At the time of writing there are no statistical analysis of planet properties in circumbinary systems since only 7 such planets have been discovered. However, two trends have been detected so far that need to be addressed by future space missions, namely, planet packing near the dynamical stability limit, and the absence of planets hosted by short period binaries, which are the vast majority of the binary population (see eq. 57).

Thus, we focus on the comparison between planets in S–type orbit with one or more stellar companion, and planets orbiting single stars. It is to point out that the most updated study in the literature on this subject (Desidera and Barbieri, 2007) is outdated, and does not take account of the data from recent transit surveys. Thus, the statistical analysis with up–to–date data could lead to potentially different results. However, both the radial velocity surveys and those using the transit technique suffer of biases against binary detection. Hence, it is not guaranteed that the new studies would be more realistics. Nonetheless, it is instructive to review the basic results obtained from this former study.

MASS DISTRIBUTION From the fit with a power–law of the minimum planetary mass, Roell et al. (2012) found that, while an exponent of -1.03 describes the distribution of all exoplanet candidates, this trend splits in an exponent of -0.97 for multiple stellar systems, and -1.04 for single stars. Moreover, the mean mass of planets in single star systems is of $2.5 M_J$, while it is equal to $3.1 M_J$ for multiple stars.

This trend was confirmed also by Desidera and Barbieri (2007). They divided the binaries in two categories, based on the critical semimajor axis (Holman and Wiegert, 1999) (see Sec. 4.4.2). As it is shown in Fig. 8, for tight binaries ($a_c < 75$ AU), the distribution of massive planets with short orbital periods was statistically different from those orbiting single stars. On the other hand, wide binaries ($a_c > 75$ AU) do not show this trend.

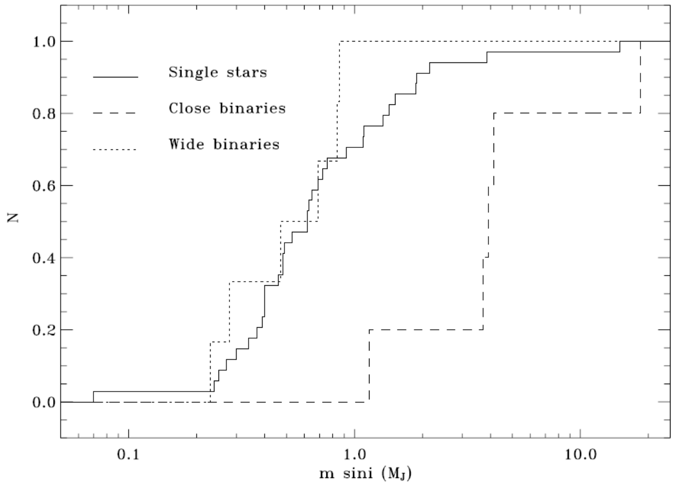

Figure 8: Distribution of the minimum mass for planets with $P < 40$ day, $K < 15$ m/s, orbiting single stars (continuous line), tight binaries (dashed line), and wide binaries (dotted line) In the top panel it is shown the histogram, while in the bottom one the cumulative distribution (Desidera and Barbieri, 2007).

In fact, (Roell et al., 2012) evinced that the planetary minimum mass decreases with an encreasing projected stellar separation (see Fig. 9).

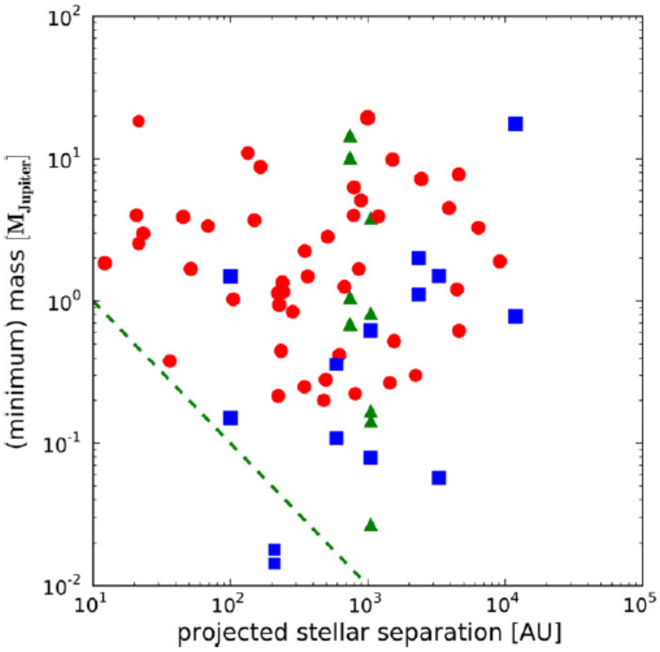

Figure 9: Planetary minimum mass over the projected separation between the exoplanet host star and its stellar companion. The markers represent the number of planets per system (dots–one, squares–two, and triangles–three). The size of the symbols represent the mass of the exoplanet host star (Roell et al., 2012).

As pointed out by Desidera and Barbieri (2007), possible causes of these differentiation could be ascribed to Kozai resonance followed by tidal circularization, and a faster growth and migration rate in these environments as predicted by the Kley (2000) models.

PERIOD DISTRIBUTION Desidera and Barbieri (2007) found also that planets hosted by wide binaries have the same period distribution as those orbiting single stars (Fig. 10), while there is a slightly difference when comparing tight binaries, with a lack of planet periods greater than 1000 days. These result could be due to dynamical stability constraint in the very tight binaries, however those results are not statistically significant and therefore more data is necessary to draw some conclusions.

ECCENTRICITY DISTRIBUTION The distribution of eccentricities both in tight and wide binaries are not significantly different to those orbiting single stars (see Fig. 11), meaning that the process of eccentricity excitation is common and probably takes place during the planet evolution due to planet–disk interaction (see Chap. 8). However, there are different processes that could lead to an high eccentric-

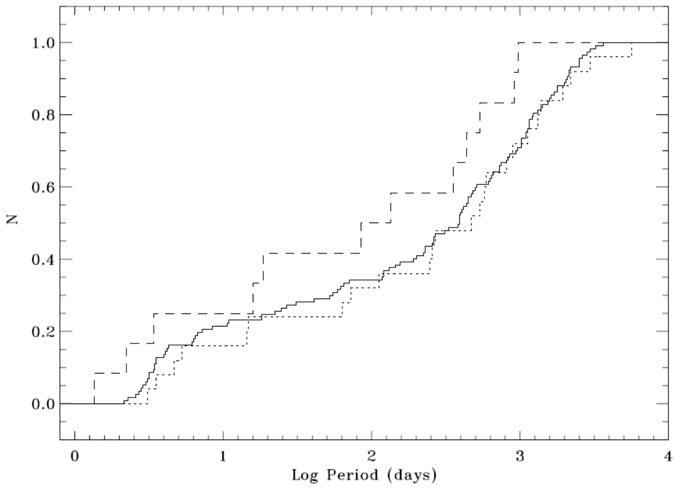

Figure 10: Cumulative distribution of log (period) for planets orbiting single stars (continuous line), tight binaries (dashed line), and wide binaries (dotted line) (Desidera and Barbieri, 2007).

ity in a planet hosted by a binary such as the Kozai resonance (see Sec. 8.3.2) or the chaotic evolution of planetary orbits owing to the stellar companion (see Sec. 8.4.2).

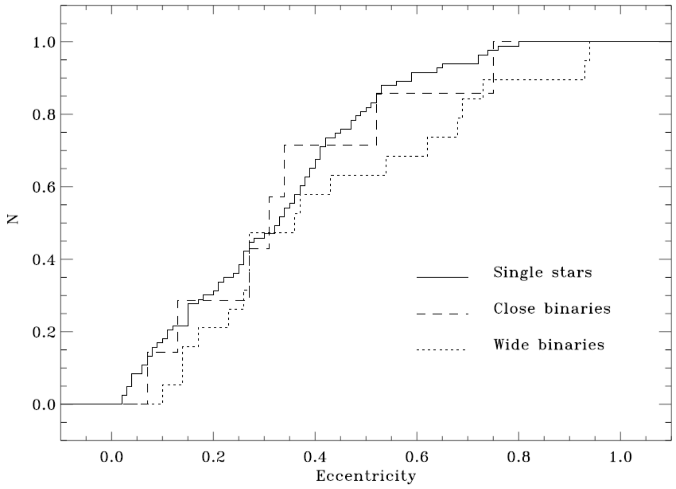

Figure 11: Cumulative distribution of eccentricity for planets orbiting single stars (continuous line), tight binaries (dashed line), and wide binaries (dotted line) with $P > 40$ day (Desidera and Barbieri, 2007).

Concerning the eccentricity of planets in multi–planetary system respect to those with only one planet, there is a clear trend that show higher eccentricities for the latter sample (Fig. 12). This behaviour is explainable considering that planetary systems with a highly eccentric planet are more prone to instabilities due to close encounters. Moreover in planetary systems the precession due to Kozai resonance is suppressed by the interaction with the other planets (see Sec. 8.3.2).

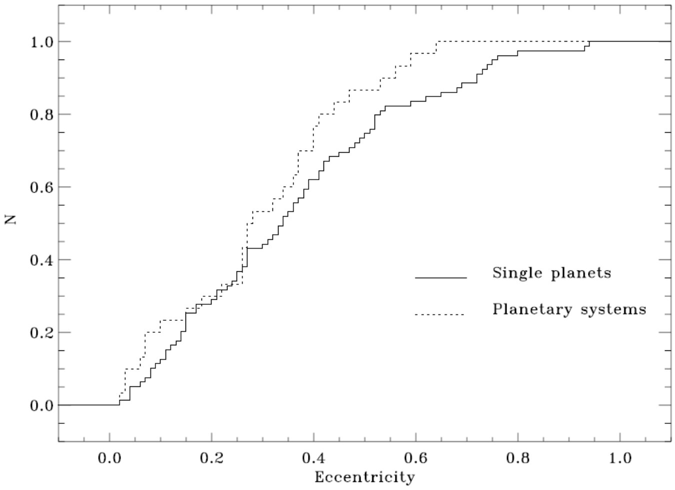

Figure 12: Cumulative distribution of eccentricity for planets orbiting single stars (continuous line), tight binaries (dashed line), and wide binaries (dotted line) (Desidera and Barbieri, 2007).

MULTI–PLANET SYSTEMS An insightful result is the absence of planets in binaries with a semimajor axis less than 10 AU, and a lack of planetary systems for binaries closer than 100 AU, that is a clear effect of the companion star tidal perturbation. Moreover, the occurence of planetary systems in wide binaries is closely to that in single stars (Desidera and Barbieri, 2007).

4.4 STATISTICAL ANALYSIS ON THE IMPACT OF BINARIES

Roell et al. (2012) found that the observed multiplicity rate of stars hosting planets is $MF = 11.95\%$, however this value is to be considered as a lower limit due to observational bias, and the real one cannot be more than a factor of three lower than that of planets orbiting single stars as derived for a complete sample of stars by Bonavita and Desidera (2007).

In order to bypass the observational biases and evaluate the impact of binaries on planet detection in a putative target field of the PLATO mission, we used the code TRILEGAL (Girardi et al., 2005, 2012), a Milky Way star counts model based on the population synthesis approach. This code was specifically modified by Girardi to separate the mass and magnitude contribution of the binary components. In this way we have a synthetic representation of the binary content of the adopted field, including the relevant orbital elements, and mass ratio. This will allow to asses the impact of stellar multiplicity on PLATO achievements.

4.4.1 *Numerical setup*

The parameter space of stellar properties given in imput to the TRILEGAL code was define by an absolute magnitudes $4 < m < 15$, superficial gravity $\log g \geqslant 3.5$, surface temperature $T \leqslant 6500K$, and apparent magnitudes $m_V \leqslant 11$.

Then, we chose a fraction of binaries equal to 0.57 (Duquennoy and Mayor, 1991), and generate a log–normal distribution of periods (eq. 57) for the binaries. The distribution of eccentricities taken into account was selected in order to mimic the orbital circularization for short period binaries and distinguish between close and wide binaries with two different normal distributions

$$f(e) = \begin{cases} 0 & \text{if } P < P_{\text{circ}} \\ C \exp \frac{-(e-\overline{e_1})}{2\sigma^2_{e_1}} & \text{if } P < P_{\text{tight}} \\ C \exp \frac{-(e-\overline{e_2})}{2\sigma^2_{e_2}} & \text{if } P > P_{\text{tight}} \end{cases} \tag{59}$$

where $P_{\text{circ}} = 11.6$ days, $P_{\text{tight}} = 1000$ days, $e_1 = 0.33$, $\sigma_{e_1} = 0.01$, $e_2 = 0.66$, $\sigma_{e_2} = 0.01$. Moreover, we crudely estimated a flat distribution of the mass ratio in the interval between 0.1 and 1.

Finally, the semimajor axes of the binary systems were derived from the period distribution with the third Kepler's law, obtaining the main orbital parameters to input the populations synthesis model TRILEGAL.

It is to note that the code does not take into account the interaction between the binary components but evolve them separetely.

The considered sample consists in 9 different regions ($10\,\text{deg}^2$ each) in the direction of a proposed long–duration PLATO field (see Fig. 13) with the distribution given in Tab. 1.

4.4.2 *Dynamical stability*

Holman and Wiegert (1999) study orbital stability in binary star systems numerically, in a wide range of star mass ratios and eccentricities.

They found that the circumstellar critical semimajor axis a_{cs} in units of the binary semimajor axis a_b is given by

$$\begin{aligned} a_{cs} =& [(0.464 \pm 0.006) + (-0.380 \pm 0.010)\mu + \\ & (-0.631 \pm 0.034)e + (0.586 \pm 0.061)\mu e + \\ & (0.150 \pm 0.041)e^2 + (-0.198 \pm 0.074)\mu e^2]a_b \end{aligned} \tag{60}$$

where e is the binary eccentricity, and μ is the star mass ratio. The validity of this expression is over the ranges $0.1 \leqslant \mu \leqslant 0.9$, and $0.0 \leqslant e \leqslant 0.8$.

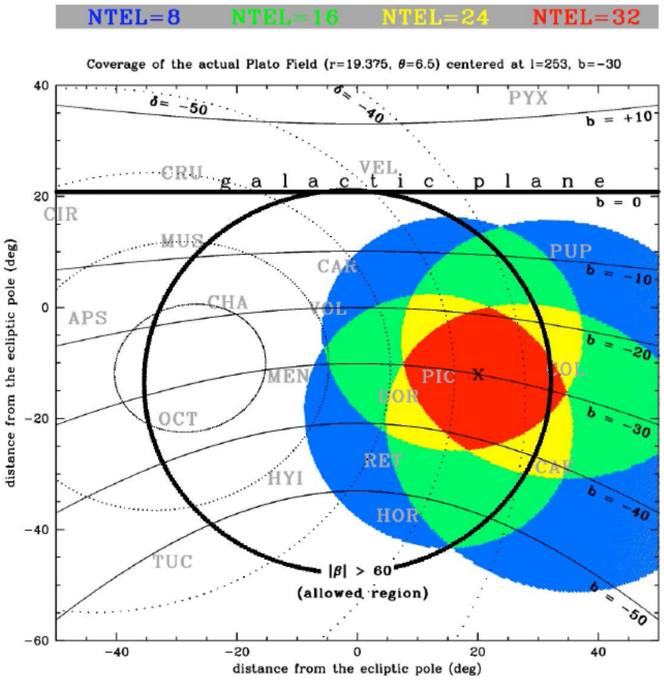

Figure 13: Preliminary long–duration PLATO field chosen for the southern allowed region, with the number of telescopes covering the single sub–regions indicated by different colours. PLATO Assessment Study Report (Yellow Book)

Table 1: List of fields

Field number	*l*	*b*
1	240	-20
2	240	-30
3	270	-10
4	270	-20
5	270	-30
6	270	-40
7	300	-20
8	300	-30
9	300	-40

Position in galactic coordinates of the simulated fields.

Holman and Wiegert (1999) verified also that, in the limit of $\mu \to 0$, the numerical solution tend to the analytical Hill stability solution $a_c \propto (1-\mu)^{1/3}$ of a circular restricted three body problem (see Sec. 8.4.1).

Corcerning planet in P–type orbit, they derive a second expression for the critical semimajor axis a_{cb} in units of the binary semimajor axis

$$\begin{aligned} a_{cb} = &(1.60 \pm 0.04) + (5.10 \pm 0.05)e + (-2.22 \pm 0.11)e^2 + \\ &(4.12 \pm 0.09)\mu + (-4.27 \pm 0.17)e\mu + \\ &(-5.09 \pm 0.11)^2 + (4.61 \pm 0.36)e^2\mu^2, \end{aligned} \tag{61}$$

which is valid over the range $0.0 \leqslant e \leqslant 0.7$ and $0.1 \leqslant \mu \leqslant 0.9$.

The numerical predictions made by (Holman and Wiegert, 1999) are robust, since they have been verified by the vast majority of the extrasolar planets discovered so far. Thus, using these values it is possible to determine which binary systems are suitable for maintaining a planet in a stable orbit, although they do not give us any information on the feasibility of planet formation (see Chap. 5,6, 7), and on the dyamical stability of multi–planetary systems (see Chap. 8).

CIRCUMSTELLAR PLANETS Concerning planets in S–type orbit, we found that (see Tab. 2) 29% of binary stars have a potential circumstellar dynamical stable region inside 1 AU. This stellar environment is thus very hostile to the presence of planets.

The intermediate sample of binaries with a circumstellar stable region between 1 and 10 AU is a very interesting case in which we will study also the process of planet formation in Chap. 6 (especially the high end of this bin). In this sample, formed by the 24% of the simulated binaries, the formation of giant planets seems unfeasible due to the strong interaction between the stars and the tidal truncation of the disk, however it could be possible to form a terrestrial planet in the inner regions.

Finally, almost half of the binary sample (47%) has a critical semimajor axis greater than 10 AU, where the potential planetary system is less subject to the influence of the companion star. Hence, those are possible targets for the planet detection mission. As it is shown in Fig. 14, the fraction of stars with increasing critical semimajor axis smoothly decrease in log–scale to very wide separeted binaries. However, since the disk extension around single Solar–type stars is typically about 100 AU, and the disk truncation due to the binary companion is equal to $r_t \sim a_B/3$ (Artymowicz and Lubow, 1994), we can consider planets in binary systems with semimajor axes greater than 300 AU almost indistinguishable from those orbiting single stars.

Parker and Quanz (2013) performed a similar analysis with slightly different conditions, for a generic sample of Galactic field stars using a Monte Carlo code. They consider the combined probability to find a

Table 2: Critical semimajor axes

Property	Number	Fraction
$a_{\text{crit,cs}} \leqslant 1$ AU	80	29%
$1 > a_{\text{crit,cs}} \leqslant 10$ AU	65	24%
$a_{\text{crit,cs}} > 10$ AU	129	47%
$a_{\text{crit,cb}} \leqslant 10$ AU	76	26%

Binary fractions with a cirmustellar and circumbinary critical semimajor axis in different intervals.

stable planet hosted by single and binary stars in S–type orbit. The dynamical stability was calculated using the Holman and Wiegert (1999) critical semimajor axis for binary stars, while they considered a probability of 100% to find a planet hosted by a single star. Their results are reported in Fig. 15, where they varyed the fraction of binaries in their sample starting from a value of 46%, similar to our sample, to the totality of the sample (100%).

It can be seen that the probability to find a planet inside an orbit of 1 AU ranges between ~ 65% for a binary only population, up to 95% when a fraction of 46% is considered.

From Fig. 15 it could be also seen that this fraction decreases almost linearly in log–space as a function of the semimajor axis, reaching a fraction of systems that can host a planet that ranges between 20 and 65% at 100 AU.

CIRCUMBINARY PLANETS Concerning planets in P–type orbit (see Tab. 2), from our analysis we find that 26% of the binary sample has a potential circumbinary habitable zone within 10 AU. It is to note that we do not separate the sample of binaries that could host a stable circumstellar planetary system, from that hosting a potential circumbinary one. Thus, this fraction of binaries are part of the first two samples consider above, which could not host a stable circumstellar planetary system.

(Parker and Quanz, 2013) found (see Fig. 16), from the combined probability of finding a stable planet hosted by single or binary stars in circumbinary orbit, that the fraction of stars that can harbour a planet at 1 AU ranges from 5 to 59% while, that at 100 AU, from 34 to 75%, again with a binary star population with a minimum of 46% and a maximum of 100% of the simulated sample. Thus, the trend is opposite to that observed for S–type orbit with a fractional increase of potential planets with an increasing binary semimajor axis.

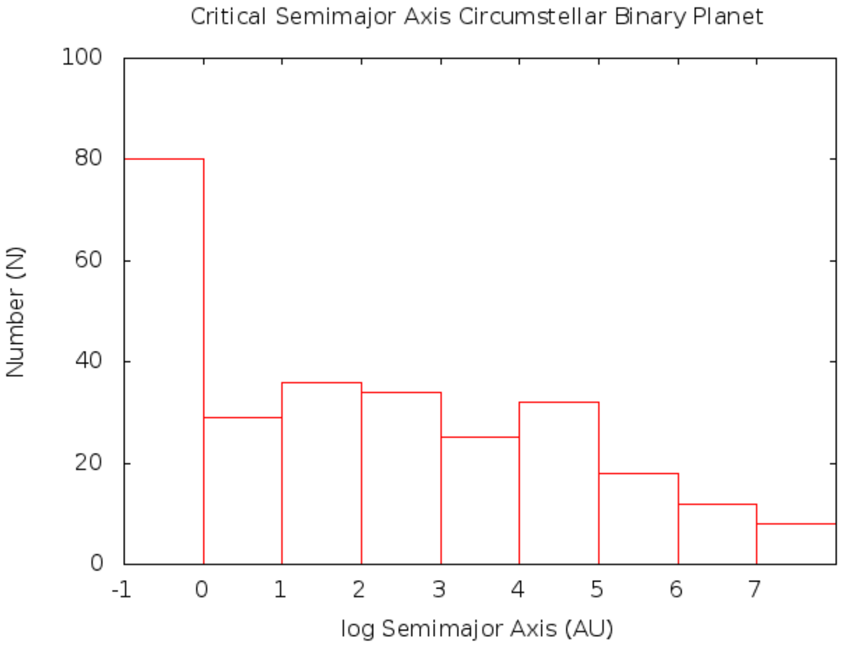

Figure 14: Distribution of circumstellar critical semimajor axis in log scale.

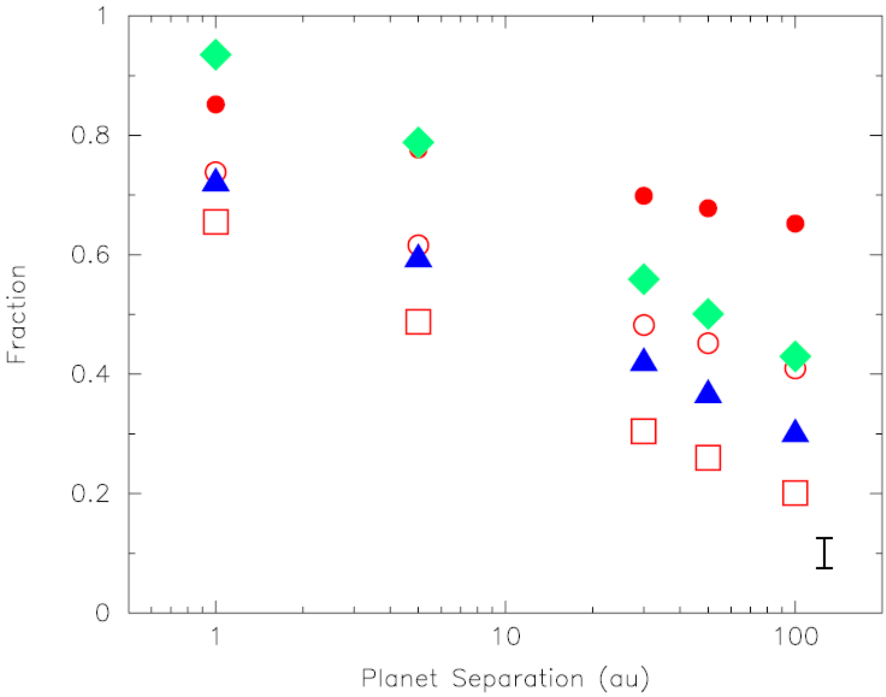

Figure 15: Fraction of systems (binaries and single stars) that could host a stable planet at the given separation on S–type orbits. The filled red circles are for systems with a field–like binary fraction (0.46), whereas the open red circles and open red squares show the fraction of systems that could host a stable planet for the same orbital parameters but binary fractions of 0.75 and 1, respectively (Parker and Quanz, 2013).

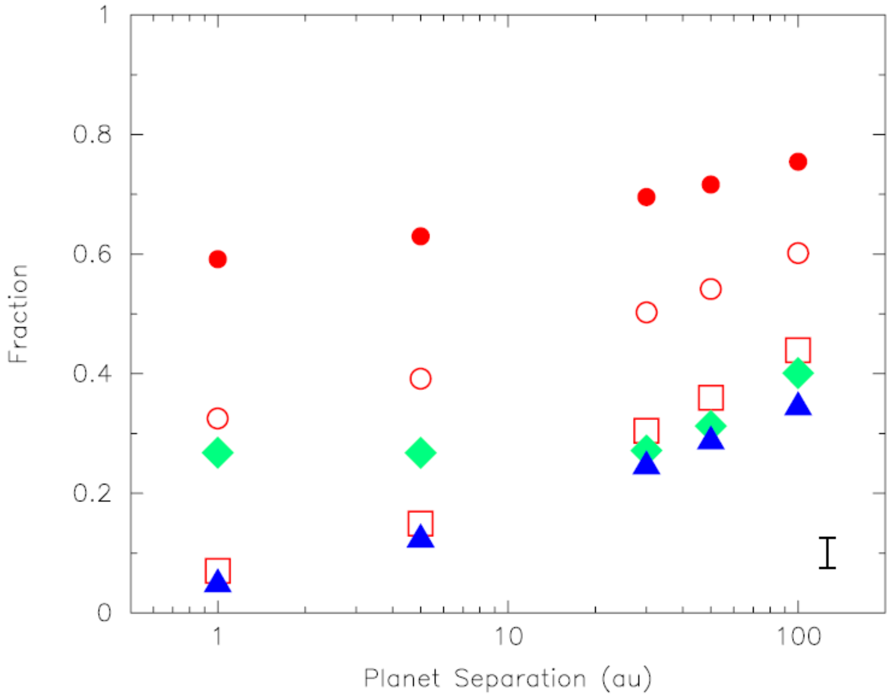

Figure 16: Fraction of systems (binaries and single stars) that could host a stable planet at the given separation on P–type orbits. See legend of Fig. 15 (Parker and Quanz, 2013).

4.4.3 *Observational impacts of binaries*

The analysis of the obervational impact of binaries in the selected PLATO field is based on the contamination of targets due to blendig effect, and on the distribution of angular separations of the binary components, in order to define the number of them that the PLATO photometer is capable to resolve.

BLENDING EFFECT Assuming a magnitude–limited sample, as in the case of PLATO mission, the blending effect consists in the contamination of the selected targets due to binary or multiple stars that enters in the sample only because their composed magnitude is in the selected range, but not the individual components. The binary fraction in the sample, as shown in Tab. 3, is increased by ~ 6% from the initial value due to this effect, leading to a sample formed by ~ 2/3 of binaries. The importance of this effect is better shown in Tab. 4, where it is reported the relative increase in the binary fraction, which is equal to the 20% due to blendig. There is also a little contribution due to binaries with only the secondary companion with $m_V < 11$, which can be explained with the evolution of the primary into a white dwarf.

However, Fig. 17 shows that the magnitude of the blendig effect is limited in most cases (~ 70%) to 0.1 mag.

Table 3: Binary fraction

Star type / Ratio	Value
Single Stars	159
Binary Stars	282
Binary/Tot.	64%
Binary/Tot. no blend	58%

Number of single and binary stars in the sample.

Table 4: Binary fraction

Property	Number	Fraction
$m_{V,p} \leqslant 11$	221	78%
$m_{V,s} \leqslant 11$	34	12%
$m_V \leqslant 11$, $m_{V,p} > 11$, $m_{V,s} \leqslant 11$	3	1%
$m_V \leqslant 11$, $m_{V,p} > 11$, $m_{V,s} > 11$	58	20%

Contribution of the binary components to the binary magnitude.

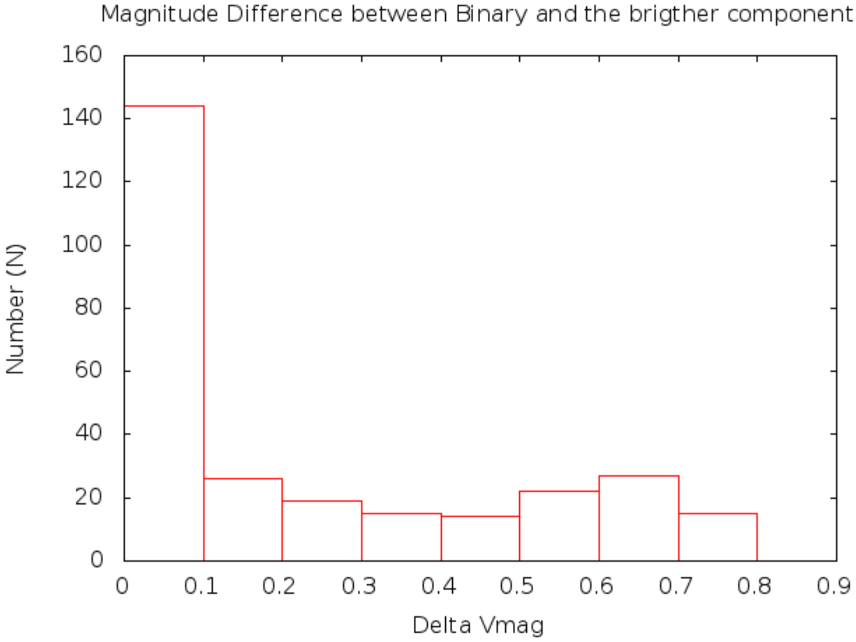

Figure 17: Magnitude difference (in V band) due to blending effect of the stellar companion.

Table 5: Angular separations

Property	Number	Fraction
$\text{sep} \leqslant 1$ arcsec	193	68%
$1 < \text{sep} \leqslant 30$ arcsec	69	24%
$\text{sep} > 30$ arcsec	20	7%

Angular separation (in arcsec) between the binary components.

ANGULAR SEPARATION The projected angular separation between the binaries components (here taken equal to the semimajor axis) are shown in Tab. 5. In 68% of the cases, it is less than 1 arcsec, thus it can be separated only in a few cases with high contrast imaging. Instead, 24% of the binaries have a separation between 1 and 30 arcsec which can be separated with high resolution direct imaging. The only fraction of binaries that the PLATO photometer could directly resolve with its PSF of 30 arcsec is the 7%. However, with the aid of GAIA mission that has an angular resolution of 20 mas, the vast majority of this binaries could be solved. In Fig. 18 we show the angular separation distribution, where it can be seen that it peaks at 1 arcsec.

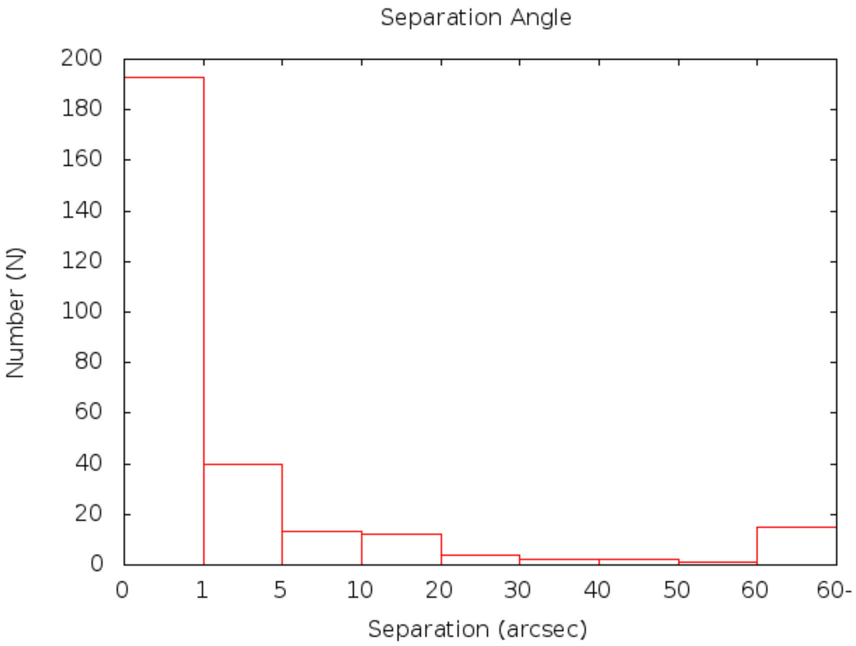

Figure 18: Angular separation distribution between the binary components.

4.5 CONCLUSIONS

It has been shown that the fraction of binary stars is close to that of single Solar–type stars in the Galactic field. However, the number of planets detected in binaries so far is a little fraction of those orbiting single stars, and their properties are possibily strongly affected by bias and selection effects. Hence, statistical analysis of planetary properties in those systems are to be taken with extreme caution.

Nevertheless, they showed that planets in wide binary systems have nearly the same mass and period distributions of planets orbiting single stars (Desidera and Barbieri, 2007). The only difference is due to a possible greater abundance of high eccentric orbits. Conversely, for tight binaries, it was found a statistical significative abundance of massive close–in planets, meaning that in those systems the process of planet formation and/or migration are more complex (see Chaps. 6,8).

In order to understand the properties of planets in binary systems, bypassing the observational bias, it is possible to recreate via a population synthesis software (such as TRILEGAL (Girardi et al., 2005)) the distribution of stars from a selected region of the Galactic field, and define the dynamical stability regions where a planet could be find with the aid of the (Holman and Wiegert, 1999) critical semimajor axes.

This analysis is of paramount importance to maximize the process of field selection for a space mission dedicated to planet detection, such as PLATO. We found that the fraction of binaries that could host a planet in the dynamical stability region in S–type orbit is the 47% of the sample, which is compatible with the value obtained by Parker and Quanz (2013). Moreover, we find a dynamical stability region inner than 10 AU also in the circumbinary region of the 26% of the sample.

Thus, the total fraction of binaries where a planet is potentially detectable is 73%, which is a realatively high value considering the strong influence that could have the gravity of the companion star.

We must point out that these are only dynamical stable regions. In order to derive a better estimate of the impact of binaries on planets we have to address also the more restrictive planet formation conditions.

We studied also the impact of the binaries due to observational effects. Since we adopted a magnitude–limited sample, we find that the blending increase the total fraction of binaries by 6%, giving a total number of binaries equal to $\sim 2/3$ of the entire sample. Finally, we found that PLATO would be capable of resolving only a small fraction of the binary in the sample (7%), while the majority of them could be resolved only with high contrast imaging. However, Gaia will provide astrometric orbits of binaries with periods from a few days to a few years, then allowing to clean the imput catalog from unsuitable binaries. Moreover, it would be possible to select samples of binaries with well defined characteristics from the Gaia catalogue for in–depth study of the impact of multiplicity on planet frequency and properties.

Part III

PLANET FORMATION

5

PLANET FORMATION

5.1 INTRODUCTION

The formation of a planet is a very complex process that starts from micron–sized dust particles in the protoplanetary nebula and builds up terrestrial and giant planets through a growth of at least 12 orders of magnitude in size scale.

This huge range of physical parameters can't be described with a single physical process. Therefore, according to the ongoing dominant mechanism, planet formation process has been divided in 3 main steps: planetesimal formation, terrestrial planet formation, and giant planet formation.

Moreover, each step strongly depends on the physical properties of the disk and stellar system in which it takes place. In this Chapter I will discuss the main phases of the standard model of planet formation in a single stellar environment.

5.2 PLANETESIMAL FORMATION

Planetesimal formation is the more complex and less understood phase of planet formation, since it depends strongly on gas dynamics, and requires a study both from a physical and a chemical point of view in order to determine if the accretion process is possible. Here I will focus on the standard model of sedimentation and collisional growth of dust particles (Lissauer, 1993), shedding some light on the connected problems, and briefly exponing possible alternative proposed scenarios.

Our starting point is a sub–micron sized dust particle immersed in a protoplanetary disk, whose dynamics is dominated by its interaction with the gas.

Lets consider a spherical particle with radius r and mass density ρ_d suspended in a gas disk with density ρ, mean–free path λ, temperature T, and mean molecular weight μ.

If $r < \lambda$, then the gas component is seen by the dust particle as a sample of molecules with a Maxwellian velocity distribution, and the interaction between them is well described by the frequency of their binary collisions. This is called the Epstein drag regime. If the relative velocity between gas molecules and the dust particle $\mathbf{v}$ is not supersonical ($|\mathbf{v}| < v_{th}$), where v_{th} is the mean gas thermal speed

$$v_{th} = \sqrt{\frac{8k_BT}{\pi\mu m_H}}, \tag{62}$$

with k_B the Boltzmann constant, and m_H the hydrogen atom mass, than the net drag force experienced by the particle as it moves through the disk is (Weidenschilling, 1977)

$$\mathbf{F}_D = -\frac{4\pi}{3}\rho r^2 v_{th}\mathbf{v}. \tag{63}$$

When dust particles grow up to $r > \lambda$, the gas act on them as a fluid, and we enter in the Stokes drag regime. So, we can use the fluid dynamics to describe the dust motion, and the drag force acting on it can be expressed as (Adachi et al., 1976)

$$\mathbf{F}_D = kv\mathbf{v}, \tag{64}$$

where the parameter k is given by (Kary et al., 1993)

$$k = \frac{3\rho C_D}{8\rho_d r}, \tag{65}$$

and C_D is the drag coefficient, which depends on the shape of the particle and on the fluid Reynolds number

$$Re = \frac{2rv}{\nu_m}, \tag{66}$$

where ν_m is the molecular viscosity.

DUST SETTLING For the moment we neglect the disk gas turbulence and consider the dust evolution in a laminar disk, and in the Epstein drag regime. The dynamics of the dust in its early phases is strongly bound with the gas dynamics. In effect, the friction time scale, that describes the dust–gas coupling as the time interval in which the relative velocity is significantly modified by the gas drag

$$t_{fric} = \frac{mv}{|F_D|} = \frac{\rho_d}{\rho}\frac{r}{v_{th}}, \tag{67}$$

is of the order of 10 s for a micron–sized dust particle in a typical protoplanetary disk at 1 AU.

In the vertical direction the major force acting on the dust is the stellar gravity

$$|\mathbf{F}_{grav}| = m\Omega^2 z, \tag{68}$$

where $\Omega = \sqrt{GM_\star/d^3}$ is the local Keplerian angular velocity. For a gas molecule in an isothermal disk this force is equally balanced by the pressure gradient. However, a dust particle is not supported by the pressure, so it will accelerate until the gas drag balances the gravitational force, and then slowly drifts towards the median–plane with a settling velocity

$$v_{set} = \frac{\rho_d}{\rho}\frac{r}{v_{th}}\Omega^2 z. \tag{69}$$

The time needed at a particle to reach the disk midplane is

$$t_{\text{set}} = \frac{z}{|v_{\text{set}}|}. \tag{70}$$

Noteworthy, the settling velocity depends on the gas density ρ, so it is faster at high z where the gas is more rarefied, and on the particle size r, encreasing towards the median plane as the particles grow via coagulation. Dullemond and Dominik (2005) found that, if collisions lead to particle adhesion, that is probable due to the low impact velocities (on the order of cm/s), then the settling time is of the order of 10^3 yr. Thus, all the dust will sediment in the disk mid–plane in a timescale shorter than the disk lifetime (several million years).

We have neglected so far the effect of turbulence on particle growth and sedimentation. The analysis of these processes is complex, however the net result is that the turbulence acts to stir up dust particles, preventing their sedimentation up to the mm scale, and encreasing the settling time by an order of magnitude.

RADIAL DRIFT As in the vertical direction, the gas is partially supported against the disk self gravity by an outward pressure gradient also in the radial direction. In the assumption that the local mid–plane pressure is describable with a power law $P \propto r^{-n}$, the gas radial velocity is

$$v_{\phi,\text{gas}} = v_K (1 - \eta)^{1/2}, \tag{71}$$

where $\eta = n c_s^2 / v_K^2$, $v_K = \sqrt{GM_\star/d}$ is the Keplerian speed, and c_s is the local sound speed. For typical disk parameters the gas rotates $\sim 0.5\%$ slower than the Keplerian speed.

We can study two limiting cases

- small dust particles (sub–mm) are strongly coupled with the gas disk ($\Omega t_{\text{fric}} << 1$), so they are forced to have a sub–Keplerian velocity. Thus, the centrifugal force does not balance star gravity and they spiral inward.
- greater solid bodies (mm – km) decouple from the gas disk ($\Omega t_{\text{fric}} >> 1$), and orbit with a Keplerian speed. Hence, they experience a headwind from the sub–Keplerian gas surrounding them that removes their angular momentum. The net result is again an inward drift, with a higher speed.

We must point out that m–sized bodies have the fastest inward drift, and they would be accreted by the star in a time scale of the order of ~ 100 yr if any other process doesn't come into play. For bodies greater than the m scale, the drift velocity slows down again thanks to a smaller surface area to mass ratio.

Since the radial drift depends on particle size, there will be a relative radial velocity between different sized particles. This in turn leads to particle growth via coagulation if the relative velocities are small enough to permit it.

PLANETESIMAL GROWTH The simplest model of planetesimal growth is via pairwise collision. Adhesion is a very efficient process for sub–mm particles, while it is difficult to imagine that this process holds also for m–sized particles, due to their high impact velocities.

If we consider a single particle population with number density n and collisional cross section σ, then the collisional time scale is

$$t_{\rm coll} = \frac{1}{n\sigma\Delta v}, \tag{72}$$

where Δv is their relative velocity.

For micron–sized particles the Brownian motion dominates and the resulting collisional time is of the order of 10 yr. Larger particles will have longer collisional time scales (on the order of 10^3 yr in the inner disk), comparable with the time needed by the radial drift to drive them into the star. However, their settling velocities are faster, increasing the impact probability, and possibly repopulating the particles lost by stellar accretion.

The outcome of a collision is strongly dependant on the relative velocity of the impactors, which span from $\Delta v \sim 0.1$ cm/s for micron–sized particles up to $\Delta v \sim 10$–100 m/s for m–sized rocks, and on their particle size and composition (chemical and physical).

For smaller particles the surface forces have a fundamental role and the threshold relative velocity for spherical grains is in the order of 1–2 m/s. Larger particles have a decreasing surface area to mass ratio, meaning that the surface forces are less effective and the critical factor is the particle ability to dissipate energy during collisions. Thus, rocks have the lowest probability to stick, meanwhile loosely bound aggregates of dust or ice can lead to a net growth even for $\Delta v > 10$ m/s (Wurm et al., 2005).

The planetesimal formation process described so far is thus capable to explain the particle growth through many orders of magnitude. The critical point is the m–sized scale where the collisional time is comparable with the drift velocity. A possible solution is that a rapid pairwise growth continues also in this scale size, refurnishing the bodies accreted into the star.

However, there are also other theories of planetesimal formation that could explain this difficult transition. The Goldreich–Ward mechanism (Goldreich and Ward, 1973) states that the gravitational instability comes into play in the dust layer (we will discuss this mechanism further in sec. 5.4.2), forming km–sized planetesimals directly from the collapse of small dust particles, bypassing many orders of magnitude and the problems associated with them. However, it requires a very high dust fraction in order that collapse is not prevented by turbulence.

Johansen et al. (2007); Cuzzi et al. (2008) proposed an alternative possibility, based on the direct formation of large planetesimals from the accumulation of small solid particles in turbulent structures of the gaseous disk.

5.3 TERRESTRIAL PLANET FORMATION

We start to talk about planetesimals when the gas dynamics becomes only a perturbation to the gravitational interaction between the solid bodies in the protoplanetary disk, and this transition happens when their physical scale reach the order of 1 km. Terrestrial planets build up from pairwise collisions of planetesimals. The dynamic of collision is strongly dominated by gravity, which assures that the majority of the colliding mass becomes bound. The only important parameter for the planetesimal growth in this case is the collisional cross–section, that is the geometrical cross–section modified by the gravity of the bodies and the tidal action of the star.

STELLAR INFLUENCE The radius within which the gravitational action of a protoplanet with mass M and semimajor axis a dominates over that of his host star, with mass $M_\star$, is given by the Hill sphere radius

$$r_H \sim \left(\frac{M_p}{M_\star}\right)^{1/3} a. \tag{73}$$

We can define an associated Hill velocity

$$v_H \sim \sqrt{\frac{GM_p}{r_H}}. \tag{74}$$

and talk about

- dispersion dominated regime, if the dispersion velocity v of bodies with mass $m < M$ passing nearby the protoplanet is greater than the Hill velocity $v > v_H$. This regime is well described by the gravitational interaction between the protoplanet and the particles in a two body approach.
- shear dominated regime, if $v < v_H$. We must take account also of the tidal stellar interaction, considering the full three–body dynamics.

We must stretch out that not all the particles approaching a protoplanet will impact on it. In effect, if a small body passes nearby a protoplanet with a closest distance greater than a few Hill radii, it will be almost unperturbed. Moreover, if the body orbit is closely equal to that of the protoplanet it will enter in a horseshoe orbit and never become gravitationally bound.

Finally, it is to point out that not all the impacts lead to a net growth. Depending on the relative velocity, mass ratio, and physical composition of the impactors, we can have an accretion where most of impactors mass becomes part of the solid body of the planetesimal, a shattering where the colliding particles brake up but remain gravitationally bound, or a dispersal where they break up in different unbounded pieces.

GRAVITATIONAL FOCUSING The gravitational focusing is the cross–section enhancement due to the gravity of the planetesimal. Lets consider a protoplanet with mass M and radius r_1, and a small body passing nearby with mass m and radius r_2. If the relative velocity at infinity is v, the closest distance between them r_c, and we are in the dispersion dominated regime (we can completely ignore the host star influence), the collisional cross–section will be

$$C = \pi(r_1 + r_2)^2 F_g, \tag{75}$$

where the first two terms on the right side represent the geometrical collisional cross–section, and

$$F_g = \left(1 + \frac{v_{esc}^2}{v^2}\right), \tag{76}$$

is the gravitational focusing term, with v_{esc} escape velocity from the point of closest approach

$$v_{esc}^2 = \sqrt{\frac{2G(M+m)}{r_1 + r_2}}. \tag{77}$$

The gravitational focusing strongly depends on the relative planetesimal velocity, and it is strongest in a cold planetesimal disk where $v << v_{esc}$.

PLANETARY GROWTH Lets consider a protoplanet of mass M, radius R and escape speed v_{esc} embedded in a planetesimal swarm with mean mass m in the dispersion dominated regime with an isotropic dispersion velocity v and a volume density ρ_s. The mass growth rate of the protoplanet is (Kokubo and Ida, 1996)

$$\frac{dM}{dt} = \rho_s v \pi R^2 F_g. \tag{78}$$

We can distinguish two main growth regimes

- orderly growth, when the dispersion velocity is comparable or larger than the escape velocity ($v \geqslant v_{esc}$). The gravitational focusing term (eq. 76) is of order unity ($F_g \sim 1$), and the growth rate

$$\dot{M} \propto R^2; \dot{M} \propto M^{2/3}, \tag{79}$$

is determined only by the geometrical cross section. This growth regime is typical in the first phases of planet formation.

- runaway growth, when the dispersion velocity is small compared with the escape velocity ($v << v_{\rm esc}$). The focusing term can be approximated as

  $$F_g \simeq \frac{v_{\rm esc}^2}{v^2} = \frac{2GM}{v^2 R}, \tag{80}$$

  and, from eq. 78, the growth rate is

  $$\dot{M} \propto R^4, \dot{M} \propto M^{4/3}. \tag{81}$$

  Thus, as the protoplanet grows larger, the influence of the gravitational focusing becomes increasingly stronger, dominating the collisional cross section and boosting the planetary growth.

When the growing planetary embryo starts to dominate the stirring, the dispersion velocity of the swarm slows further, becoming comparable with the Hill velocity $v \leqslant v_H$, and we enter in the shear dominated regime. In this case the details are much more complicated, since we must take into account also the gravitational influence of the star/s on the collisional cross section. The net result is a new slow orderly growth

$$\dot{M} \propto M^{2/3}, \tag{82}$$

called oligarchic growth, where larger embryos take longer to encrease their masses, but the mass ratio between them and the planetesimal swarm continues to encrease.

The oligarchic growth ends up after 0.01–1 Myr with the formation of 10^2–10^3 massive protoplanets (10^{-2}–$10^{-1} M_\oplus$) capable of depleting the planetesimal disk surrounding them. Thus, the dynamical friction due to the planetesimal disk can no longer dominate over the long range gravitational interactions between the protoplanets, pumping up their relative velocities. As a result, the protoplanet accumulation drops promptly and their mutual interaction can lead to crossing orbits and strong inelastic collisions. For this reason this stage is also called the phase of great impacts. It is a relative long phase (10^8 yr) which results in the formation of few terrestrial planets and a consistent chemical mixing throughout the disk.

5.4 GIANT PLANET FORMATION

There are two competing theories that explain giant planet formation, namely, the core accretion model (that consequently follows the terrestrial planet formation) and the disk instability model. The main constraint of these models is the relatively short time scale in which the giant planets have to form before the disk gas dispersal (10^7 yr).

5.4.1 *Core accretion model*

The core accretion model builds up giant planets from the planetary cores that reach the critical mass to star accreting a massive gas envelope.

There are 4 main phases in which this process could be divided

- Core formation. The protoplanetary core is formed via pairwise collisions with the standard model of terrestrial planet formation described in the previous section.

- Hydrostatic growth. The gas envelope retained by the planetary embryo grows slowly in hydrostatic equilibrium.

  A protoplanet is capable of maintaining an atmosphere when the gas thermal energy is lower than the gravitational energy. In other words, when the escape velocity is greater than the thermal speed $v_{esc} \geqslant v_{th}$. The associated mass is very low since, at the current location of Jupiter with standard protoplanetary disk parameters, it is equal to $M_p \sim 0.01 M_\oplus$. However, the core mass necessary to retain a significantly gas mass fraction is an order of magnitude greater, and it decreases with the semimajor axis embryos, being of $1 M_\oplus$ at 1 AU.

  During the first phases, when the core is still embedded in the planetesimal disk, the accretion rate of solids is larger than the gaseous component. Thus, the accreting core forces the gas to contract, and increases its atmosphere thanks to the growing escape velocity. This process continues rapidly until the atmosphere becomes optically thick to its own radiation and the pressure gradient hinder the gravitational contraction, leading to a self–regulated contraction.

  Finally, when the planet cleans the protoplanets in its proximity, the solid and gaseous accretion rate slow down and the atmosphere enters a long stage of quasi-static contraction, where the gravitational energy E_{grav} released is balanced by the envelope's luminosity L. This balance is defined by the Kelvin–Helmhotz timescale

  $$t_{KH} = \frac{|E_{grav}|}{L} \sim \frac{G M_c M_e}{R L}, \qquad (83)$$

  where M_c and M_e are the core and envelope mass respectively, and R is the protoplanet average radius. Its magnitude depends mainly on the atmosphere opacity and the solid accretion rate and it is of the order of 10^6 yr. Therefore, it is comparable with the time of gas disk dispersal and it is critical to determine if the planet becomes a gaseous giant or retains only a small amount of gas like Uranus and Neptune in our Solar System.

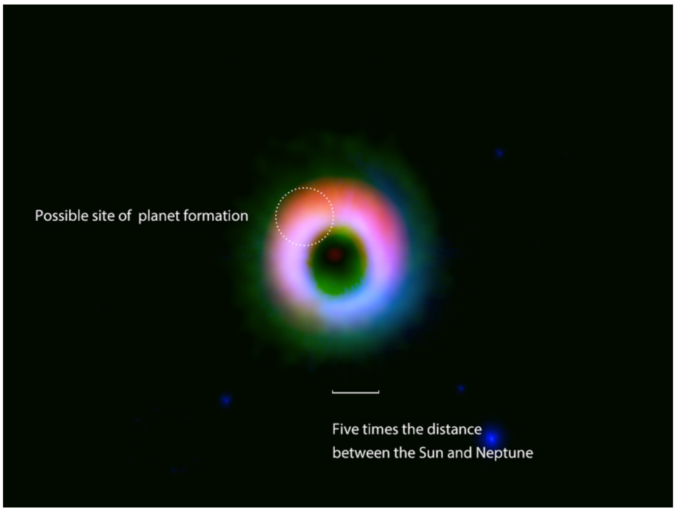

Figure 19: Local Enhancement of Surface Density in the Protoplanetary Ring Surrounding HD 142527 as viewed by ALMA. Credit: ALMA (ESO/NAOJ/NRAO), NAOJ, (Fukagawa et al., 2013).

- Runaway growth. When the critical mass is reached a phase of runaway growth starts, limited only by the nearby gaseous component supply.

  From analytic models of planetary atmosphere, where the inner envelope is considered fully convective while the outer fully radiative, it is found that it will collapse when the envelope mass becomes equal to the core mass.

  Once reached this point, the protoplanet starts to accrete gas from the protoplanetary disk at a high rate, limited only by the disk–planet tidal interaction. The gas accretion rate in this phase for a planet with mass M and capture radius R_c embedded in a gas disk with superficial density Σ and disk thickness H, such as $R_c < H$ is given by

  $$\frac{dM}{dt} \sim \frac{\Sigma}{H}\Omega R_c^2, \tag{84}$$

  which is approximately the product of mass flux and planetary cross section. There are two important accretion scales, the Hill radius and the Bondi radius. The Hill radius represents the distance beyond which the star gravitational influence dominates over the planet 73. While the Bondi radius set a limit beyond which the gas thermal energy becomes greater than the planet gravitational energy

  $$R_B = \frac{GM}{c_s^2}. \tag{85}$$

  We can consider two regimes associated with those scales

  - Bondi–type regime, for $R_B < R_H$. The Bondi radius becomes the distance inside which the gas particles are accreted onto the planet. Substituting the capture radius in eq. 84 with the Bondi radius (eq. 85) we find that the accretion rate in this regime is

    $$\frac{dM}{dt} \propto M^3, \tag{86}$$

    which is faster than an exponential growth. This accretion regime is strongly dependant on the local sound speed and therefore on the disk thickness.

  - Hill–type regime, for $R_H < R_B$. The Hill radius becomes the limiting distance for gas accretion. Replacing the Hill radius with the capture radius in eq. 84 we find an accretion rate of

    $$\frac{dM}{dt} \propto M, \tag{87}$$

    which is an exponential growth. This regime is poorly dependant on the local sound speed since the gravitational force dominates.

  In this phase the great majority of the planetary envelope is accreted in a rather small timescale ($\sim 10^5$ yr).

- Termination of accretion. When the gas supply in the planetary neighborhood is terminated the accretion stops abruptly and the planet enters in a long phase of cooling and quasi–hydrostatic contraction. The main causes of the gaseous depletion are the formation of a local gap and the gas disk dissipation due to the photoevaporation by the star/s.

5.4.2 *Disk instability model*

The disk instability model (Kuiper, 1951; Cameron, 1978; Boss, 1997) starts from the idea that a sufficiently massive protoplanetary disk can become unstable to its own self–gravity leading to disk fragmentation.

The great advantage of this model is the short timescale (on the order of orbital time) needed to form giant planets directly from the pristine protoplanetary disk material, bypassing the time constraints imposed by the dust accretion process.

The critical parameter that determines the disk stability against self–gravitating collapse is (Toomre, 1964)

$$Q \equiv \frac{c_s \kappa}{\pi G \Sigma}, \tag{88}$$

where κ is the epicyclic frequency

$$\kappa^2 \equiv 4\Omega^2 + 2r\Omega\frac{d\Omega}{dr}, \tag{89}$$

that represents the frequency at which a fluid element oscillates when perturbed from circular motion. It reduces to $\kappa^2 = \Omega^2$ for a Keplerian potential.

For $Q < 1$ the disk is unstable against axysimmetric disturbances (Toomre, 1964), where the pressure (c_s) term acts to stabilize short wavelengths disturbances, while the rotation (κ) term the long ones. Moreover, for $Q < 1.5$–1.7, the disk becomes unstable against non–axysimmetric perturbations (Durisen et al., 2007).

Thus, the Toomre Q parameter represents the balance between pressure and rotation which act to arrest the disk collapse, and the gravitational force which favour clump formation. If Q is of order unity, the disk is prone to instability. An analogue of the eq. 88 on a global scale for a Keplerian disk with vertical hydrostatic equilibrium $H = c_s/\Omega$ is

$$\frac{M_d}{M_\star} \geqslant h, \tag{90}$$

where M_d is the disk mass, and $h = H/r = c_s/\Omega$ is the disk scale height. Thus, a thin (cold) disk could become gravitationally unstable although it is not very massive, and conversely a thick (hot) disk could hinder fragmentation even if it is very massive.

When the Toomre factor becomes lower than the critial value Q_{crit}, the disk instability sets in. However there are two possible outcomes:

- Fragmentation. The collapse continues until one or more bound objects are formed.

- Angular momentum transport. As we have stated above, the first linearly unstable modes ($Q < 1.5$–1.7) are generally non–axisymmetric. Thus, they develop spiral–like structures able to transport angular momentum outward via gravitational torque, and therefore mass inward. In turn, the energy released during mass accretion can heat up the disk, raising the Q value beyond the critical one, and reaching a marginal stability (Paczynski, 1978).

The resulting outcome for a particular disk is closely related with its ability to radiate thermal energy, balancing the accretion heating and lowering Q.

To study this problem we start considering the turbolent viscosity generated by gravitational instability (GI) in the form (Shakura and Sunyaev, 1973)

$$\nu = \alpha c_s h, \tag{91}$$

where ν is the kinematic viscosity, and α is called the Shakura–Sunyaev parameter and measures the turbulence efficiency to transport angular momentum. Since this approach models the viscosity as a function of local quantities, it is valid only if the angular momentum transport generated could be approximate as a local process, which is valid for a low disk–to–star mass ratio $q < 0.5$ and a thin disk $h \leqslant 0.1$ (Forgan et al., 2011).

There are two main events that could trigger disk instability in a marginally stable disk, namely, an increase in the local surface density or a decrease in the local mid–plane temperature. The last process has the shorter timescale, and so is the most efficient in boosting the GI.

Defining a local cooling time

$$t_{\mathrm{cool}} = \frac{U}{|dU/dt|}, \tag{92}$$

Gammie (2001) found that the α parameter necessary to start GI is inversely proportional to the cooling time

$$\alpha = \frac{4}{9\gamma(\gamma-1)\Omega t_{\mathrm{cool}}}, \tag{93}$$

where γ is the two–dimensional adiabatic index, and the critical value is $\alpha_{\mathrm{crit}} \simeq 0.1$, which corresponds to a local cooling time of $t_{\mathrm{cool,crit}} \simeq 3/\Omega$, although it is not clear if this limit applies also on 3–D simulations (Meru and Bate, 2012).

All in all, we need both a gravitational unstable disk ($Q < 1$) and a short cooling time in order to obtain clump formation. This process could possible happen in the outer cool parts of the disk (50–100 AU) if it is sufficiently massive. The result will be a giant planet, which slowly contracts via quasistatic stages and differentiates creating a solid core.

6

PLANET FORMATION IN BINARY STAR SYSTEMS : CIRCUMSTELLAR CASE

As for single stars, binary stars in the early stages of their evolution are surrounded by protoplanetary disks. An example is the L1551 IRS 5 system, which contains two protostars, each surrounded by a circumstellar disk (Rodríguez et al., 1998; Osorio et al., 2003). Spatially resolved observations of disks in binaries in the Orion nebula cluster (Daemgen et al., 2012) suggest that the fraction of circumstellar disks around individual components of binary systems is about 40%, only slightly lower than that for single stars (roughly 50%). This is possibly due to the impact of the companion star on the disk evolution which causes disk truncation, eccentric shape, warping, and heating (Nelson, 2000; Kley and Nelson, 2008; Paardekooper et al., 2008; Marzari et al., 2009, 2012).

The physical properties of circumstellar disks are relevant for forming planetary systems. Perturbed disks, like those in close binaries, may affect planet accretion at different stages, producing a population of planets that differ from those around single stars. The process by which dust particles evolve into kilometer–sized planetesimals, which is still not fully understood for single stars ((Weidenschilling, 1977; Blum and Wurm, 2008), see sec. 5.2), may be altered in disks around binaries. Spiral waves excited by the companion perturbations may, via Epstein drag coupling (eq. 63), affect the relative velocity of the colliding particles, the drift rate towards the star and the vertical settling speed. All these parameters strongly influence the collisional sticking process and dust agglomeration into larger bodies, and the binary perturbations appear to act against a fast dust coagulation. On the other hand, the large scale motions in these disks, excited by the gravitational pull of the companion star, may locally favor concentration and subsequent accumulation of dust and pebbles directly into planetesimals (Johansen et al., 2007; Cuzzi et al., 2008). Even the planetesimal accretion phase appears more complex in close binary systems due to the increase in the mutual impact velocity between the planetesimals caused by the combined action of secular perturbations by the companion star and gas drag effects (Marzari and Scholl, 2000; Thébault et al., 2004, 2006, 2008; Kley and Nelson, 2008; Thébault et al., 2009; Marzari et al., 2009; Xie and Zhou, 2009; Xie et al., 2010b; Paardekooper et al., 2008; Marzari et al., 2012).

In spite of all these additional complications, which seem to lower the efficiency of planet formation, about 50 planets are known to date in binary stars, among which are also the newly discovered planet in the Alpha Centauri system (Dumusque et al., 2012). In addition, according to Bonavita and Desidera (2007) and Mugrauer and Neuhäuser (2009), the frequency of planets in binaries do not appear to differ much from that of planets orbiting single stars. However, it is reasonable to expect that the differences in the two initial steps of planet formation – dust coagulation and planetesimal accretion – would have a significant impact on the final physical properties and dynamical architecture of planetary systems around single and binary stars. For example, Zucker and Mazeh (2002), Eggenberger et al. (2004), Mugrauer et al. (2005), and Desidera and Barbieri (2007) find some discrepancies in the mass–period and eccentricity–period diagrams of planets in binaries and single stars.

The dynamical structure of circumstellar disks in binaries is crucial not only to understand the processes of planet formation but also to predict the migration of planets. Their morphology, temperature, and density profiles are significantly affected by the excitation of eccentric modes (Paardekooper et al., 2008; Kley and Nelson, 2008; Marzari et al., 2009), shock waves formation, and mass exchange (Nelson, 2000). These differences, compared to disks around single stars, may influence the migration speed and direction. Population synthesis calculations, like those described in Mordasini et al. (2012), have shown that differences in migration may lead to distinct predictions concerning the final orbital and mass distributions of planets. To understand the architecture of planetary systems in binaries, in particular those with small separations, it is then important to know the morphology and physical state of circumstellar disks in the crucial phases of planet growth, i.e., during dust coagulation and planetesimal accumulation.

In order to obtain some hints on planet formation in binary stars, we model the 3D evolution of circumstellar disks in binaries using the SPH code VINE (Wetzstein et al., 2009; Nelson et al., 2009). The original code had been upgraded to improve both momentum and energy conservation. In addition, to better model optically thick disks in their initial stages of evolution, we have implemented a radiative energy equation. This is particularly recommended since the companion star induces strong spiral waves in the disks that may generate local strong shocks and compressional heating violating the local isothermal approximation. In addition, these shocks may also produce notable effects in the vertical direction, potentially affecting the dust coagulation process.

In Appendix A we focus on the upgrades to the SPH code VINE and on the implementation of the radiation hydrodynamics.

Table 6: Parameters of the simulations

Acronym	a_B (AU)	ρ (g/cm^3)
HIDECL	30	$1 \cdot 10^{-9}$
LODECL	30	$5 \cdot 10^{-10}$
HIDEFA	50	$1 \cdot 10^{-9}$
LODEFA	50	$5 \cdot 10^{-10}$

6.1 INITIAL SETUP OF THE DISKS IN THE BINARY SYSTEM

The parameter space of a binary system with a circumstellar disk surrounding each stellar component is very wide so we focus in this thesis on a configuration that is supposed to be the more plausible one according to observations. A mass ratio of $\mu = M_s/M_p = 0.4$ and an eccentricity of $e = 0.4$ are adopted in the definition of our standard case since these values are statistically the most frequent among the binary systems observed so far (Duquennoy and Mayor, 1991). Two different values of the binary semi–major axis are adopted in our models: $a = 30$ and $a = 50$ AU. Coplanarity is assumed between the disks and the binary orbit, even if in the future we plan to relax this constraint. We consider a high–density disk with a midplane density $\rho_0(r = 1, z = 0) = 1 \cdot 10^{-9}$ g/cm^3, which is a value close to that prescribed by the minimum mass solar nebula (MMSN) model. A second less massive case, with $\rho_0(r = 1, z = 0) = 5 \cdot 10^{-10}$ g/cm^3, is also modeled to test the influence of the initial density profile on the morphology and physical properties of the disks. Hereinafter, the four different runs are named in the following way: the high–density case with binary semi–major axis $a_B = 30$ AU is called HIDECL, while the low density case with the same value of a_B is named LODECL. The two runs with $a_B = 50$ AU are called HIDEFA and LODEFA, respectively.

The density midplane radial profile is computed as $\rho_0(r) \propto r^{-1.5}$. The initial vertical density stratification of the disks is computed as in Bitsch and Kley (2010) using a Gaussian–like dependence of the density on z. This is a good approximation for a stationary disk where the pressure balances the z–component of the central star gravity

$$\rho(r, z) = \rho_0(r, z) \exp\left[-\frac{z^2}{2H^2}\right], \tag{94}$$

with the scale height $h = H/r$ initially set to a constant value of 0.04. The circumprimary disk extends from 0.5 AU to 8 AU and the circumsecondary to 5.5 AU, both within the tidal truncation limits computed by Artymowicz and Lubow (1994) in the case where the binary semi–major axis is set to 30 AU. For the second case where $a_B = 50$ AU our configuration with relatively small disks is similar to that observed for the system L1551 IRS 5 (Rodríguez et al., 1998) where the circumstellar disks of the binary system are well separated and smaller than the tidal truncation radius. We did not increase the size of the disks up to the tidal truncation radius since we wanted to explore whether a less perturbed configuration with the stars moving farther away affects the same disks of the simulations with $a_B = 30$ AU. At the outer border, the disk density is smoothly truncated with $\rho(r, z)$ exponentially decreasing. The mass of the primary disk in the HIDECL and HIDEFA models is $0.015 M_\odot$, while that of the secondary is $0.003 M_\odot$. The secondary disk is less massive since we scale its initial density with the stellar mass and its initial radius is also smaller. In the LODECL and LODEFA models the masses of the disks are $0.0075 M_\odot$ and $0.0015 M_\odot$, respectively since the density is reduced by a factor 2.

Each disk is initially evolved as a single disk around its star until it reaches a steady state both in density and temperature. Once this state is reached, the stars and their disks are combined into a binary system with the desired orbital parameters. Each SPH simulation uses about $1 \cdot 10^6$ particles distributed in both disks according to their size and density. The distinctive parameters of the four different models are summarized in Table 6. Those SPH particles traveling within 0.5 AU are accreted by the star. Their number is limited in time, and for this reason, we do not correct for their effects on the pressure and viscous forces on particles moving inside the border as in Bate et al. (1995).

The initial values of α_{SPH} and β_{SPH} adopted in the simulations are 0.1 and 0.2, respectively. The α_{SS} viscosity, estimated from eq. (167), is about $(2-4) \cdot 10^{-3}$ for the primary disk and $(1-2) \cdot 10^{-3}$ for the disk around the secondary star. The α_{SS} of the primary disk is very close to that of Nelson (2000).

6.2 RESULTS

In the forthcoming sections, we describe the evolution of the disks in the four different models. We focus on the disk morphology,the occurrence of shock waves, and the mass exchange between the two disks (in particular for the cases with $a_B = 30$ AU). Shock waves cause the onset of hydraulic jumps along the vertical axis, which might significantly affect the dust accumulation towards the median plane of the disk and possibly inhibit the planetesimal formation via pairwise accumulation. In addition, in the models with small a_B, the high temperature induced by the pericenter passages, and not fully dissipated at the apocenter, may further inhibit planet formation, as already guessed by Nelson (2000). The asymmetry in the disk shape will also be explored as a potential prediction for observers.

6.2.1 *High–density disks*

In the top panel of Fig. 20 we illustrate the integrated density of the circumstellar disks in the HIDECL model. The secondary star is close to the pericenter of its orbit around the primary, the most perturbing configuration for the two disks. This is the third pericenter passage of our simulation, which took about three months of CPU time on a dedicated 32–processor machine (VINE is parallelized with OPENMP). This long integration time is due to the radiative transfer, which requires a very short time step, in particular close to the pericenter when strong spiral waves are excited in both disks, and mass is transferred from one disk to the other.

The primary disk displays two prominent, tidally generated trailing spiral arms that tightly wind towards the center of the disk. The appearance of this pattern, initially at the outer edges of the disk, begins when the companion star approaches the primary star, and they reach their maximum intensity shortly after the pericenter passage. They are transient features, and they are gradually damped when the stars evolve towards the apocenter. The gas density is significantly higher at the location of the spirals as is the temperature (see Fig. 23). The arms cover a substantial portion of the disk affecting its overall evolution even by locally changing the shear viscosity and heating rate. In Fig. 20 the secondary disk seems to have a more complex spiral pattern with three arms, but an additional arm, as we see later on, is simply excited by the impact of stream material coming from the primary disk. A significant mass transfer occurs during the pericenter passage mostly from the primary star to the secondary. This phenomenon might in the long term lead to a redistribution of mass between the two disks with the initially smaller one becoming slowly more massive and gradually loosing memory of its initial density profile. The spiral waves are also visible in the $x-z$ and $y-z$ sections of the disks as regions of higher density and inflated in the vertical direction.

6.2.2 *Spiral shock waves, hydraulic jumps and dust settling*

Three–dimensional waves in accretion disks act like fundamental modes that correspond to large surface distortions in the disk (Lubow and Ogilvie, 1998). Boley et al. (2005) have shown that shock waves in 3D disks cause abrupt increases in the disk scale height. These jumps convert part of the flow’s initial kinetic energy into potential energy, while some is irreversibly lost into heat. Breaking waves, generated at the jump, crash onto the pre–shock flow creating additional disordered motion and possibly affecting the chondrule formation and dust settling processes. This shock–related splashing, observed in the bottom plots of Fig. 20, is evidently highly nonlinear and has the

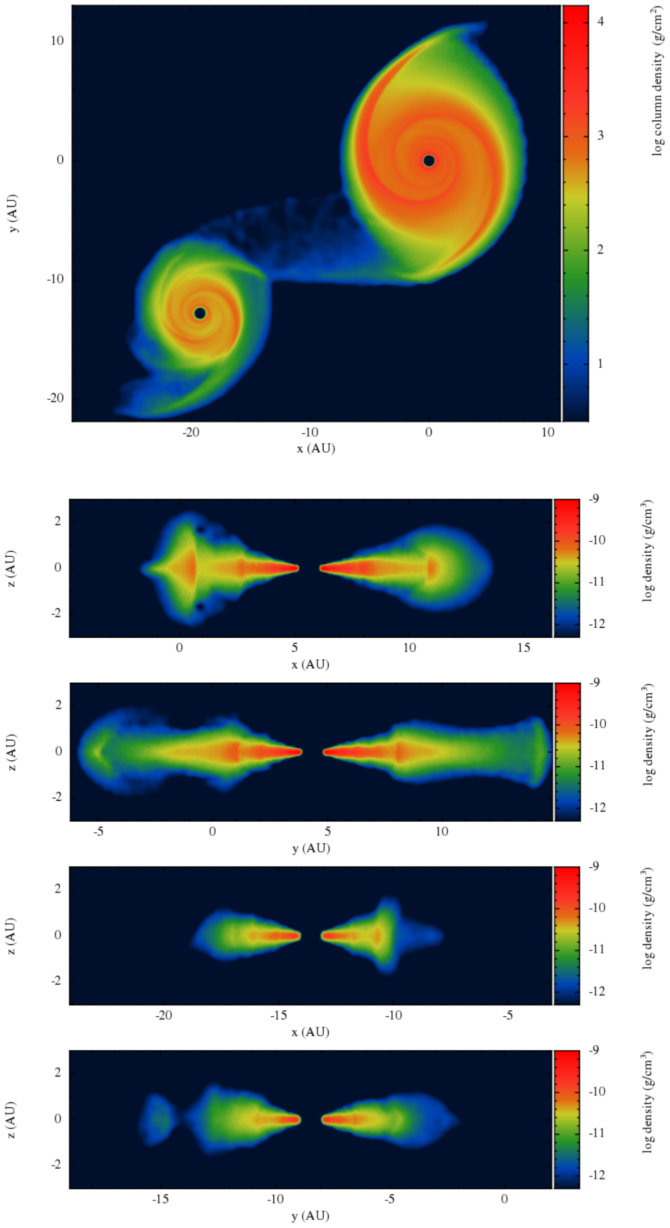

Figure 20: In the top plot the logarithm of the superficial density (column integrated) of the circumstellar disks for HIDECL (high density, small binary semi-major axis) is shown during the pericenter passage of the secondary star. In the bottom panels the density (non–integrated) is drawn along the $x-z$ and $y-z$ sections of the primary disk (2nd and 3rd panels) and secondary disk (4th and 5th panels).

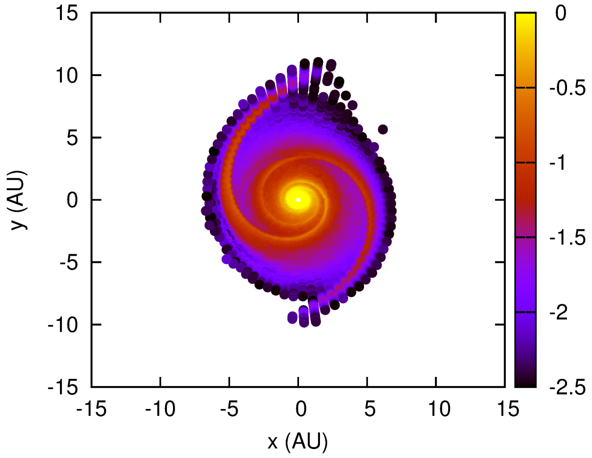

Figure 21: Vertically integrated vortensity in the primary disk during the pericenter passage in the HIDECL model.

characteristics of hydraulic jumps that behave, in part, like gravity modes (Martos and Cox, 1998). To verify that the waves excited during the pericenter passage are indeed shock waves, we performed two tests. First we estimated a 2D vortensity by computing the ratio between a column integrated vorticity ω derived for each SPH particle as $\omega = \hat{\mathbf{z}} \cdot (\nabla \times \mathbf{v})$ and the superficial density Σ as the average of the 3D density ρ over concentric rings

$$\eta = \frac{\omega}{\Sigma}. \tag{95}$$

This quantity is used locally as an indicator of shocks since vortensity is generated when the material passes through a shock. In Fig. 21 the spiral waves are clearly outlined, and the vortensity perturbations are superimposed on the density waves observed in the superficial density plots.

The second test relies entirely on the fact that spiral shocks also lead to hydraulic jumps (Durisen, 2011). In general, a hydraulic jump occurs when the flow reaches a region where there is an abrupt decrease in its speed. Conservation of mass, momentum, and energy requires that the bulk kinetic energy of the prejump flow be converted across the jump into gravitational potential energy and disordered motion. There is an increase in the flow vertical height at the shock wave passage, according to the Rankine–Hugoniot equations, and the consequent fallback of gas onto the disk causes additional disordered motion and the developing of vortices. Even though the gas in the protoplanetary disk is compressible, the formation of a shock wave, in our scenario forced by the gravitational perturbations of the companion star, produces a similar phenomenon. We can estimate quantitatively how much the scale height of the disk is affected by the shock wave using a simplified model developed by Boley et al. (2005), which assumes that the shock is planar, is vertically stratified in the direc-

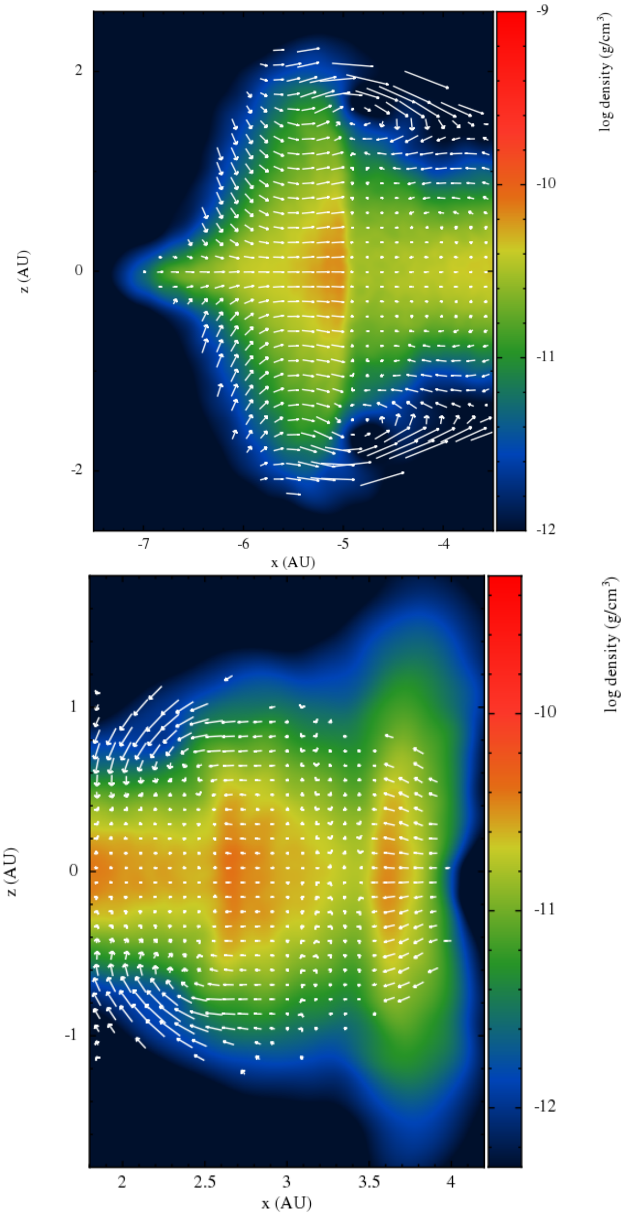

Figure 22: Velocity field and density of a slice in the (x, z) plane in the region of hydraulic jumps for the primary (top panel) and secondary (bottom panel) in the HIDECL model. Both disks are centered on their parent stars to properly compute the gas velocity field. The scales in x and z are different in the two plots and, in addition, the star is on the right in the top plot (circumprimary disk), while it is on the left in the bottom one (circumsecondary disk).

tion perpendicular to the wave propagation, and has the pre–shock region in vertical hydrostatic equilibrium.

Defining the jump factor J_f as the ratio between the pressure body forces and self–gravitating potentials in the pre–shock and post–shock regions Boley et al. (2005) find that for strong shock waves ($M >> 1$) and when the background potential dominates the gas potential

$$J_f \to \frac{2\gamma M^2(\gamma-1)}{(\gamma+1)^2}, \tag{96}$$

where M is the Mach number and γ is the adiabatic index. The two limiting cases are

- $J_f > 1$, the gas is overpressured, and it will expand vertically;
- $J_f < 1$, self–gravity cause the gas to compress.

A strong adiabatic shock ($M \to \infty$) disrupts vertical hydrostatic equilibrium, because $J_f > 1$ and the material expands upward at the sound speed on a timescale of approximately $H/c_s \approx \Omega^{-1} = t_{rot}/2\pi$. As shown in the bottom panels of Fig. 20, at the spiral waves the density distribution along the z–axis is puffed up, and this confirms that in our models we are in the $J_f > 1$ case where the gas expands vertically. To predict the height of the shock bore, Boley et al. (2005) adopt a classical hydraulic jump model, where $g_z = \mathrm{cost}$. The jump of the fluid behind the shock is determined by the Froude number

$$F = \frac{V}{c} = \frac{u_1}{\sqrt{g_z h_1}}, \tag{97}$$

which is defined as the ratio of a characteristic velocity (V) to a gravitational wave velocity (c) or as the ratio of a body's inertia to gravitational forces, and it is an analogous to the Mach number. In a non–dissipative jump,

$$\frac{h_2}{h_1} = \sqrt{\frac{1}{4}+2F^2} - \frac{1}{2}. \tag{98}$$

In the limit of a strong jump ($F >> 1$) we would have $h_2/h_1 \sim F$. Using this classical result as a model for understanding the maximum height, a shock bore reaches during the post–shock vertical expansion, Boley et al. (2005) derive, for a non self–gravitating disk,

$$\frac{h_2}{h_1} \approx \sqrt{J_f}. \tag{99}$$

This ratio has a behavior similar to that of the Froude number described in eq. (98). When $M = 1$, $h_2/h_1 \sim 1$, and $h_2/h_1 \sim M$ when $M >> 1$. This does not mean that any fluid element close to the shock wave shows a jump in the vertical direction, but it does imply that the disk scale height will change. As an example, material near the midplane ($d\Phi/dz \rightarrow 0$, $J_f \rightarrow 0$) will not be affected by a single shock wave passage, while higher altitude gas will have the strongest response. In our HIDECL case, we can apply this model to the spiral waves observed in Fig. 20 and estimate the jump factor J_f and the corresponding Froude number. In Fig. 22 we show a detail of both disks in the $(x - z)$ plane around the shock wave. In Fig. 22a (upper plot), we show a slice of the circumprimary disk where the star is on the right. In Fig. 22b (lower plot) we instead show a detail of the circumsecondary disk where the star is on the left. Different scales are used in the plots to magnify the density variations. The formation of hydraulic jumps at the spiral waves is clearly visible with a significant increase of the gas vertical height and the formation of breaking waves on top of the jumps. The motion of the gas is evidenced by velocity vectors which are superimposed to the 2–D density plot. There is a significant decrease in the velocity magnitude across the wave and an abrupt change in the gas density. A rough estimate of the jump–factor J_f from Fig. 22a by using eq. (99) gives a value of $J_f \approx 3.2$ and a Froude number (from eq. 98) $F \approx 1.6$.

Similar values are also found in the secondary disk. The velocity field evidences the formation of breaking fronts at the top of the hydraulic jump and the splashing of material from the top of the jump. Shock bores not only generate the vertical displacement of fluid elements illustrated in Fig. 22a,b, but they also drive gas to large radial excursions from their circular orbits, causing large amounts of wave energy to be transformed into kinetic energy stirring and mixing the disk. This is also at the origin of the disk heating. When the gas crosses the shock front, the shock normal component of the fluid element velocity diminishes, according to the Rankine–Hugoniot equations, while the tangential component is preserved and the flow become supersonic after the shock. This leads to streaming along the spiral arms (Roberts et al., 1979). Moreover, when the gas expands upwards, the pressure confinement normal to the shock loosens and the fluid expands radially, causing some gas to flow back over the top of the shock. The resulting morphology is a spiral pattern moving through the disk in the $(x - y)$, as illustrated in Fig. 20, while the pattern appears as a breaking wave in the vertical direction. In the inner part of the disk we do not observe breaking waves, but this is due to the fast crossing of winding spiral arms. The orbital period of a fluid element is much shorter than the pattern period of a spiral wave. Shortly after the first shock, the gas therefore encounters another arm before it can settle back onto the disk, ending up elevated between shock passages. However, in the outer part of the disk the periods become comparable and the shock bores have the time to develop into breaking waves. The evolution of the gas disk into hydraulic jumps may have critical consequences for the dust settling towards the disk midplane. When the gas is pumped up at the shock waves, via aerodynamic effects, it can drag the smaller components of the dust inverting their settling motion. As a consequence, at each pericenter passage, the disk will develop strong spiral waves able to stir up the dust significantly slowing the sedimentation process down, if not suppressing it. In addition, it would also increase the relative velocity between dust particles halting the coagulation process at small dust sizes and possibly preventing the formation of planetesimals through the conventional scenario of dust coagulation. On the other hand, turbulent motion that may develop in the proximity of spiral waves, may favor the fast accretion of pebbles into large planetesimals, as suggested by Johansen et al. (2007) and Cuzzi et al. (2008).

6.2.3 *Temperature profile: Chondrule formation at shocks?*

In Fig. 23 we show the midplane temperature distribution of the two disks during the pericenter passage. At the shocks generated by the spiral structures, the temperature is raised to high values that might cause vaporization of some grains, as suggested by Nelson (2000), and chondrule formation (Boley et al., 2005). The secondary disk is cooler than the primary and this is due to its lower density. It appears also overheated at the outer edge, more than the circumprimary, since mass coming from the more massive circumprimary disk strikes its outer borders thereby increasing its temperature.

During the pericenter approach, there is a considerable transient internal thermal energy generation in the disks by means of shock waves and mass transfer. Once the stars depart from each other traveling towards the apocenter, the disks cool down due to radiative cooling possibly reaching an equilibrium state. This effect is shown in Fig. 24 where we compare the azimuthally and vertically averaged temperature profiles for both disks when the stars are at pericenter and apocenter, respectively. The difference is more marked in the outer parts of the disks, and it can be as large as 200 K. This phenomenon was also observed by Nelson (2000) in his simulations of an equal mass binary system with $a_B = 50$ AU and $e_b = 0.3$. He performed 2D SPH numerical simulations of such a binary star/disk + star/disk system finding a relatively mild difference in temperature between pericenter and apocenter. Our larger difference may be attributed to the different dynamical configuration. In effect, our HIDECL model system is more compact (smaller semimajor axis), and it also has higher eccentricity. This dynamical configuration leads to a stronger heating at shock waves and a larger mass exchange that causes a consistent local temperature increase where the transferred flow impacts the disk. Both these effects can explain the larger difference in the temperature profiles between pericenter and apocenter we find in our model. On the other hand, we have lower temperatures in the disks on average compared to the ones obtained in Nelson

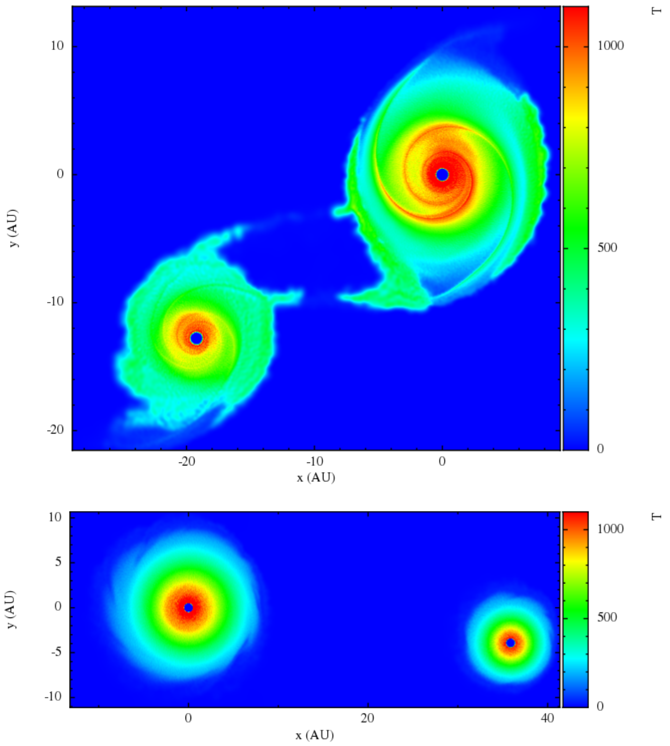

Figure 23: Temperature distribution in the two disks computed at their median plane when the stars are close to the pericenter (upper panel) and apocenter (lower panel) in the HIDECL model.

(2000) but this may be related to the different initial density adopted in his simulations, the different orbital architecture and the different cooling algorithm. The Nelson (2000) case compares better with our models where the stars have a larger separation ($a_B = 50$ AU), which is discussed later on. Our temperature profiles appear to be comparable or slightly higher than those in Müller and Kley (2012), even if a different initial density profile is adopted ($\Sigma \propto r^{-1}$ while ours declines as $\Sigma \propto r^{-1/2}$). In addition, Müller and Kley (2012) consider a single disk around the primary, and as a consequence, the mass exchange between the two disks, with its consequent heating, is not included in their model. Also, since our simulations are performed in 3D, the amount of heating due to gas compression at the shock waves where hydraulic jumps occur is higher.

While high temperatures appear to prevent the condensation of icy dust particles and then the growth of giant planet cores, they may favor the formation of chondrules. They form as melt droplets that were heated to high temperatures, while they were independent, free–floating objects in the protoplanetary nebula. After they were heated, cooled, and crystallized, chondrules were incorporated into the parent bodies in which chondrites originate. There are constraints on chondrule formation like a peak temperature of about 1300 K followed by a fast cooling (100–1000 K per hour) as suggested in Ar-

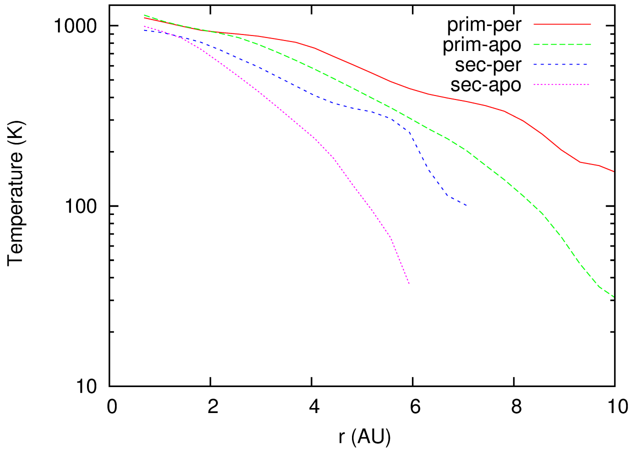

Figure 24: Azimuthally and vertically averaged temperature profiles of both disks in the HIDECL model when the stars are at pericenter and apocenter, respectively. The secondary disk is less dense than around the primary, so its temperature is on average lower.

mitage (2010). In our simulations we find that the temperature along the shock waves is higher than 1000 K, and it drops quickly after the wave passage. This may favor chondrules formation in such disks, in particular in more compact and eccentric binary configurations where stronger and possibly hotter spiral waves develop. This mechanism is not local since the shock waves induced by the companion star covers the whole disk, since the spiral wave extends from inside to the outer borders. As a consequence, it would not be necessary to invoke additional heating mechanisms or local shock fronts of different origins (Urey and Craig, 1953; Urey, 1967; Sanders and Taylor, 2005; Asphaug et al., 2011; Levy and Araki, 1989; Joung et al., 2004; Morfill et al., 1993; Pilipp et al., 1998; Desch and Cuzzi, 2000; Nakamoto et al., 2005; Boss and Graham, 1993; Ruzmaikina and Ip, 1994; Hood et al., 2009; Hood, 1998; Weidenschilling et al., 1998; Ciesla et al., 2004; Morris et al., 2012; Wood, 1996; Desch and Connolly, 2002; Boss and Durisen, 2005; Boley and Durisen, 2008). In this picture, the strong shock waves generated by binary interaction during pericenter passages might be an additional and very efficient mechanism for chondrule formation over the whole disk.

6.2.4 *Mass exchange between the disks*

When the two stars are at the pericenter, the gravitational interaction of the companion on each disk is the strongest. Spiral shock waves tidally induced by the gravitational perturbations of the stars propagate within each disk causing a significant mass transfer between the two disks in addition to disk heating. The mass exchange is bidirectional, but in absolute value, the primary disk donates more mass to

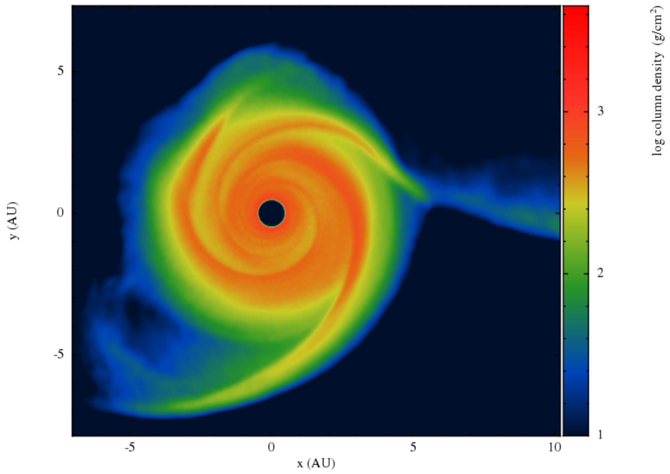

Figure 25: Density distribution of the secondary disk when the stars are at the pericenter in the HIDECL model. A new spiral arm is created by the material transferred from the primary disk and impacting the outer edge of the secondary.

the secondary, possibly because of its higher mass and its stronger shock waves that extend farther out from the disk center.

Where the mass stream coming from one disk hits the other and is accreted, heat is generated. This effect can been seen in the temperature distribution illustrated in Fig. 23a. At the edge of both disks, where the exchanged mass is accreted, the temperature is locally higher. This heating is subsequently spread around within the disk, contributing to the overall disk temperature profile. For this reason, in modeling disks in close binaries, it is important to include the secondary disk since the final temperature profile will depend on the amount of mass exchanged between the disks.

The mass accreted by the secondary disk generates an additional spiral arm in the disk as illustrated in Fig. 25. There are three spiral arms in the disk, two generated by the primary star tidal field and an additional one produced by the the impact of a stream from the primary.

The morphology of the mass flux moving from the primary to the secondary reflects the shape of the shock wave. It appears as a concave structure continuing in the shock wave direction and propagating towards the secondary disk. In Fig. 26 we show a 3D plot of the material transferred from the primary disk to the secondary and its temperature. The concave structure (like a water wave) is visible, and the gas impacting the secondary disk is heated up by the compressional motion.

The mass flow from the primary to the secondary disk induced by the formation of spiral waves during the pericenter passage can have significant effects in the long term. It can reduce the viscous mass loss of the secondary disk and change the initial post–formation mass ra-

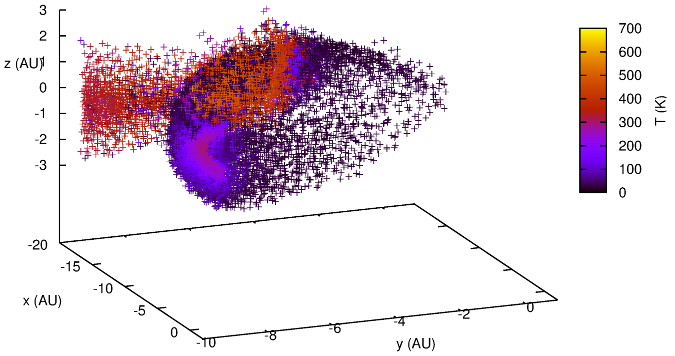

Figure 26: Temperature distribution of the material flowing from the circumprimary disk to the circumsecondary in the HIDECL model. The impact on the secondary of the flow from the primary is marked by a raise in the temperature.

tio of the two disks. If this ratio was similar to the stellar mass ratio during the protostar contraction, later on this ratio could be different. The lifetime of the secondary disk may be longer, thereby increasing the probability of finding a planet around a less massive companion star, as suggested by the discovery of the planet around Alpha Centauri B (Dumusque et al., 2012). However, a longer integration timespan is required to confirm this trend.

6.2.5 *Disk eccentricity*

The disk eccentricity is an important parameter for the evolution of a putative planetesimal population born in the disk. As shown in Paardekooper et al. (2008), Marzari et al. (2012), and Kley and Nelson (2008), an eccentric shape for the disk may perturb the evolution of the planetesimal eccentricity and orbital alignment, which may lead to destructive collisions rather than growth. The azimuthally averaged eccentricity profile of both disks (primary and secondary) at apocenter, where the spiral waves are dissipated, is shown in Fig. 27 for the HIDECL model. The disk eccentricity is low in the inner parts of both disks and it increases in the outer more perturbed regions. The eccentricity values agree with those derived in both Müller and Kley (2012) and Marzari et al. (2012) for radiative disks on a longer timescale. In our model the secondary disk is significantly more eccentric compared to the primary and this might be due to the stronger perturbations of the primary star, which is more massive, and to a reduced self–gravity related damping effect Marzari et al. (2012). It is noteworthy that the eccentricity profile we obtain after three pericenter passages is similar to that of Müller and Kley (2012) and Marzari et al. (2012), derived after more binary periods, making us confident that our results also hold in the long term. In particular, Fig. 3 of Müller and Kley (2012) shows that, for radiative disks, the eccentricity

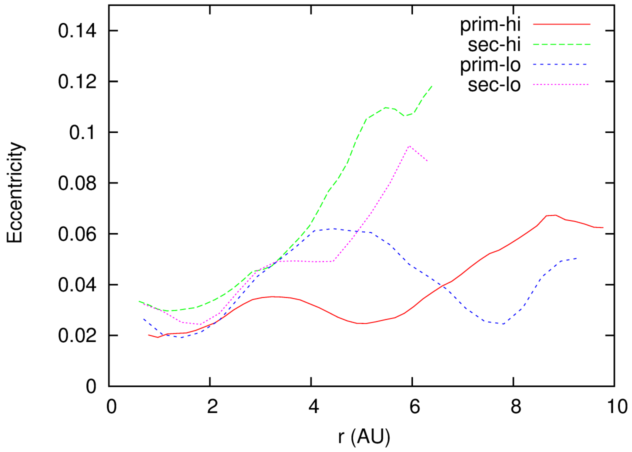

Figure 27: Disk eccentricity profiles, averaged on azimuth and vertical direction, of the primary and secondary disks in the HIDECL and LODECL models. The eccentricity is computed at the apocenter when the strong spiral arms have almost completely dissipated.

profile does not vary significantly with time. This behavior is different from isothermal disks where the disk eccentricity requires more time to reach a quasi–stationary (and more eccentric) state (Müller and Kley, 2012; Marzari et al., 2009, 2012; Kley and Nelson, 2008). As suggested in Marzari et al. (2012) and Cassen and Woolum (1996), the energy loss by radiation may be at the origin of this different evolution, leading to a faster damping of density waves in radiative disks.

6.2.6 *Low–density disks*

The morphology of the disks in the LODECL model does not differ significantly from that of the HIDECL and strong trailing spiral patterns form in the both disks close to pericenter dissipating by the time the stars move to the apocenter. The main difference between the LODECL and HIDECL scenarios concern the temperature distribution and the vertical height of the hydraulic jump at the shock waves. In Fig. 28 we compare the temperature profiles of the two cases with $a_B = 30$ AU. As expected, the lower density case has an overall lower temperature, and it is similarly heated up at the pericenter when shock waves develop and mass transfer occurs. Concerning the hydraulic jump at the shock waves, values as high as 2.2 for the h_2/h_1 ratio are found in the shock waves giving $J_f \sim 4.8$ and $F \sim 1.9$. These values are slightly higher compared to the HIDECL case and might be related to the lower sound speed in the LODECL disk, leading to larger Mach numbers. Figure 29 is a 3D picture of the two lower density disks showing the large vertical jumps at the shock waves. The eccentricity of both disks is compared in Fig. 27 to that of the

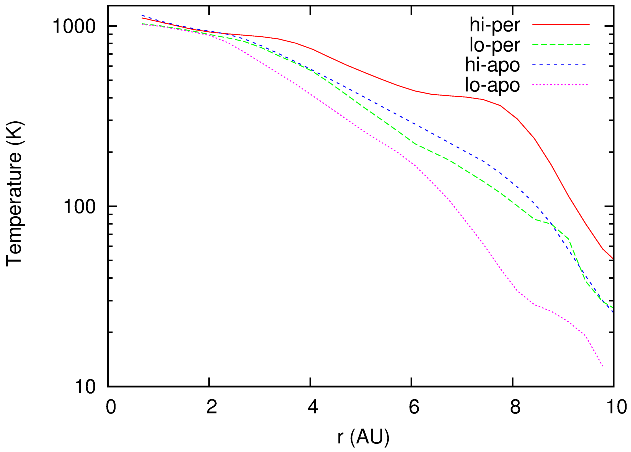

Figure 28: Azimuthally and vertically averaged temperature profiles of the low–density disk (LODECL model) around the primary star compared to the high–density case (HIDECL) with the binary at pericenter and apocenter. The lower density disk is cooler in both cases.

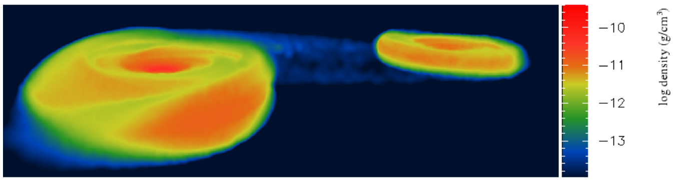

Figure 29: 3D picture of the density distribution of the disks in the LODECL model close to the binary pericenter. Large vertical jumps can be observed at the shock waves. The surfaces are drawn at $\tau \sim 2$.

HIDECL case and they show a similar behavior. As a consequence, the reduction of a factor two in density is not enough to significantly affect the shape of the disks. Even if the self–gravity damping effect is less strong Marzari et al. (2009), the lower temperature profile of the LODECL case might somehow help in keeping the overall disk eccentricity (Marzari et al., 2012) within 0.1 for both disks.

6.2.7 *Binary systems with larger separation*

In the models HIDEFA and LODEFA the semimajor axis of the binary system is increased to 50 AU, a configuration similar to the one explored by Nelson (2000). The orbital elements of the binary are the same, but Nelson (2000) considers two equal mass solar type stars and equal mass disks, while we model a system where the secondary star is less massive ($0.4M_\odot$), and the disk is scaled in density of the same ratio and is less radially extended. Differences are then expected in terms of physical properties of the disks in the simulations. We did not match the configuration of Nelson (2000) since we wanted to test the dependence of the disk evolution on the binary semimajor axis so we kept the same architecture of the previous models but we increase the binary semimajor axis. Figure 30 illustrates the integrated density distribution of the two disks in the proximity of the binary pericenter in the HIDEFA model. Two–armed spiral shock waves are still present in the secondary disk, while they are reduced to density waves in the primary. These waves are weaker than those observed in the model disks of Nelson (2000), owing to the lower mass of the companion star in our simulations and to the different disk densities and sizes. The disk around the secondary shows shock bores as in the cases with $a_B = 30$ AU (HIDECL and LODECL). This is illustrated in the lower panel of Fig. 30 from which a value of the jump factor $J_f \sim 2$ is estimated. This value is significantly lower than that computed for the HIDECL and LODECL cases as a consequence of the less perturbative configuration in the HIDEFA model. An almost negligible mass transfer between the two disks occurs in this configuration, due to the lack of strong shock waves on the primary disk. In Fig. 31 the averaged temperature profiles are compared in the close and distant cases with the stars at pericenter and apocenter. At pericenter the close case ($a_B = 30$ AU) is hotter compared to the distant ($a_B = 50$ AU) case. This is an expected outcome since both disks in the HIDECL case are significantly more perturbed by shock waves, and a remarkable mass transfer occurs. At apocenter, the primary disks have approximately the same temperature profiles since the shock waves have dissipated, and the viscous heating and cooling are almost in equilibrium. The secondary disk is instead still very hot in the HIDECL case, possibly because its dissipation timescale is longer than the binary orbital period, and its excitation at pericenter was much stronger than in the

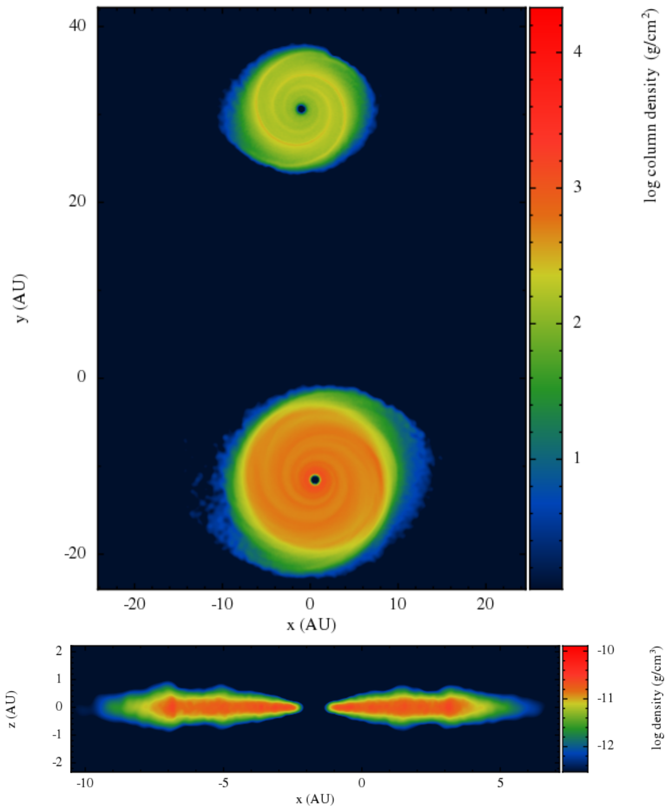

Figure 30: Integrated density profile of the disks in the HIDEFA model shortly after the pericenter (upper panel). The non–integrated density of the disk around the secondary star is shown in the x–z plane. Shock bores are visible even if less marked than in the HIDECL case. The hydraulic jumps in the primary are of negligible height.

HIDEFA case, as also shown by the lower value of J_f. Compared to the temperature profiles given in Nelson (2000), our values are lower, and this may be ascribed to the differences in the architecture of the system, in the cooling algorithm and in the fact that our models are 3D. In Fig. 32 we compare the temperatures in the LODEFA and HIDEFA cases at pericenter and, as expected, the low–density disks are cooler. In this less perturbed case, the difference in temperature between the LODEFA and HIDEFA models must be mostly ascribed to a different balance between viscous heating and radiative cooling. In both cases the temperature rise at pericenter is negligible when compared to the close cases ($a_B = 30$ AU). This can be inferred by comparing the upper panel of Fig. 31, where the stars are at pericenter, with the bottom panel where the stars are at apocenter. While there is a significant difference between the temperature profiles of the close case (HIDECL) in the two dynamical configurations, for the HIDEFA case the increase in temperature at pericenter is significantly less marked for both disks. In the distant configurations, the disk eccentricity is small independently of the initial gas density, as shown in Fig. 33. We

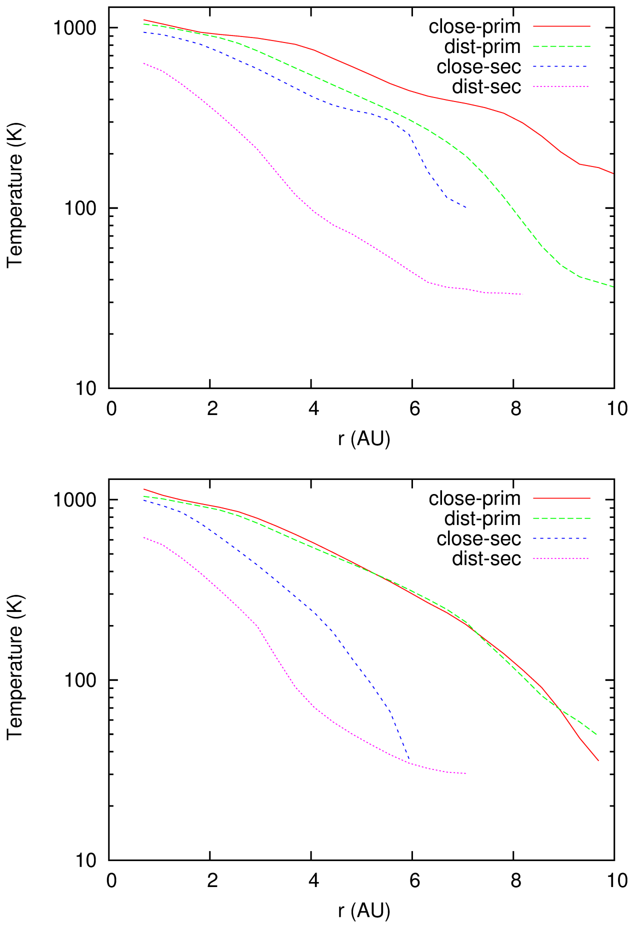

Figure 31: Comparison of the azimuthally and vertically averaged temperature profiles in the HIDEFA and HIDECL cases at pericenter (upper panel) and apocenter (lower panel) for both disks. At apocenter the temperature of the primary disk in the HIDEFA and HIDECL cases is very similar.

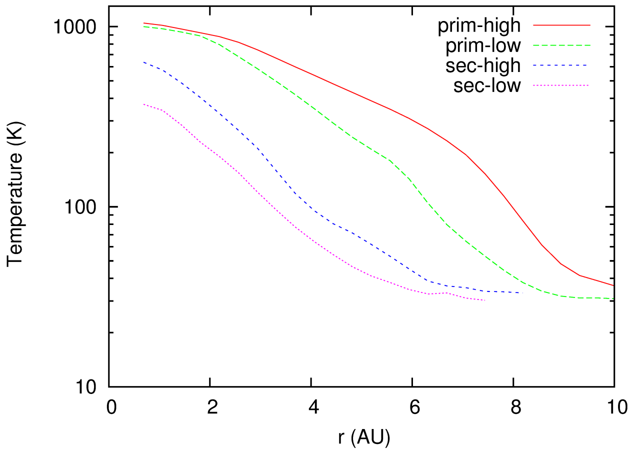

Figure 32: Temperature profiles at the binary pericenter in the LODEFA and HIDEFA cases for both the primary and secondary disks.

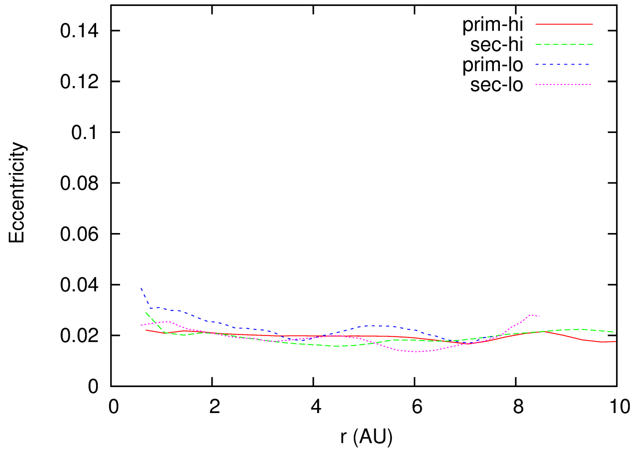

Figure 33: Eccentricity profiles for both disks in the two distant ($a_B = 50$ AU) HIDEFA and LODEFA cases. The same scale of Fig. 27 is adopted for comparison.

expect that in this more quiet configuration, planetesimal accumulation can proceed less perturbed by the disk gravity.

6.3 SUMMARY AND DISCUSSION

We have performed 3D simulations of circumstellar disks in binary systems using VINE, an SPH algorithm that has been modified to model a fully radiative disk. The cooling has been simulated by including boundary particles that populate the outer surfaces of the disks (defined by $\tau \geqslant 1$) and effectively radiate away the heat transported from the inner regions via radiative transfer. Four different binary and disk configurations are modeled to explore the influence of the companion star perturbations on the disk morphology, temperature, and eccentricity. Two close configurations ($a_B = 30$ AU) with different initial gas densities scaled by a factor 2 and two distant configurations ($a_B = 50$ AU) with the same scale factor in density.

In the close configurations the spiral shock waves excited during the pericenter approach of the two stars generate hydraulic jumps whose height can be calculated from the simulations leading to an estimate of the Froude number. A significant mass transfer occurs between the disks at the binary pericenter when tidal trailing spiral waves are excited. This is an additional source of heat for both disks, and it can also increase the mass and lifetime of the smaller secondary disk enhancing the possibility of planet formation in it. It is also noteworthy that the mass ratio between the two disks at later stages of evolution may not reflect the primordial value due to the flux of mass from the primary to the secondary.

In the secondary disks, the impact of material coming from the primary disks excites the formation of an additional shock wave. The temperature profiles show a large difference between pericenter and apocenter related to the heating generated by shock waves and mass transfer at pericenter. The disk eccentricity is relatively low for the primary disks with values compatible with previous 2D studies. The secondary disk is more eccentric compared to the primary in particular in the outer regions where the eccentricity can be as high as 0.1. There is no notable difference in the disk morphology and disk eccentricity when we model less massive disks. On the other hand, the temperature profiles, due to the dependence of the viscous heating on the density, are instead significantly different.

In the models with a higher value of the binary separation ($a_B = 50$ AU), hydraulic jumps appear only in the secondary disks, while in the primaries the spiral waves, even at the pericenter, do not cause a significant change in the disk morphology. This implies that there is a limiting binary separation beyond which the strength of the tidal spiral patterns on the primary disk is not enough to excite the motion of the gas in the vertical direction and lead to mass transfer. In these less perturbed configurations, the disk eccentricity is lower even for the secondary disks with an upper limit of ≈ 0.03 over the full radial extent of the disks. Owing to the reduced strength of the spiral waves and negligible mass exchange, the distant configurations have lower temperature profiles with the stars at pericenter compared to the close configurations. At apocenter the primary disks in the distant and close configurations have the same temperature while the secondary disk is hotter possibly because it did not dissipate all the heat accumulated during the pericenter passage. As for the close configurations, the temperature profiles of the less dense disks is lower than in higher density cases.

6.3.1 *Implications for planet formation*

As already pointed out by Nelson (2000), the high temperature of the disks and the consequent shifting outside of the "snow line" may inhibit the condensation of ices reducing the amount of available mass for accreting the core of giant planets. Although in our models the temperature profiles are lower than those found by Nelson (2000), even if with a different system architecture, the temperature is still too high in the close configurations. In the dense close configuration (HIDECL) at pericenter, the "snow line" is at about 8 AU for the primary and 6 AU for the secondary disk. In both cases, the "snow line" location almost coincides with the outer borders of the disks. At apocenter, the two values shrink to 6 AU and 4 AU, respectively. In the more distant configurations, the "snow line" is at 6 AU for the primary with negligible differences between pericenter and apocenter, while it shifts from 2 to 3 AU for the secondary disk. Even locally, at the shock waves, the temperatures are high enough to prevent icy dust condensation, but on the other hand, they might favor the formation of chondrules.

In addition to the high temperature of the disk, our simulations show that the spiral waves generate hydraulic jumps that would invert the dust settling to the disk midplane induced by the aerodynamic drag. This would significantly affect the settling velocity and timescale and, as a consequence, the coagulation process into larger particles. The relationship between the size and vertical height would be destroyed and a substantial remixing of the dust would occur at the shock bores. An additional nasty effect for particle growth would be the increase in the mutual relative velocities at the shock, in particular where breaking waves crash back onto the disk.

The two effects described above seem to work against the coagulation of dust into large planetesimals, thereby preventing the formation of planets in binaries. Even the subsequent planetesimal accretion process appears critical in binary systems as already pointed out by Marzari and Scholl (2000),Thébault et al. (2004),Thébault et al. (2006),Thébault et al. (2008),Kley and Nelson (2008), Thébault et al. (2009),Marzari et al. (2009),Xie and Zhou (2009),Xie et al. (2010b), Paardekooper et al. (2008), and Marzari et al. (2012). However, close binary systems hosting giant planets have been detected, such as γ Cephei (Campbell et al., 1988), Gliese 86 (Queloz et al., 2000), HD41004 (Zucker et al., 2004), HD196885 (Correia et al., 2008), and the small terrestrial planet in Alpha Centauri (Dumusque et al., 2012). There are two possible scenarios for the formation of the present dynamical architectures of these systems. The first is that the binary system hosting the planet had a larger separation in the past compatible with the growth of planets according to the standard core–accretion model. The subsequent dynamical evolution of the stellar system – either because it is part of an unstable triple stellar system or because it suffered a close encounter with a third (background) star (Marzari and Barbieri, 2007a,b; Martí and Beaugé, 2012) – led to a shrinking of the binary orbit without ejecting the planet(s) from the system. A second possibility is related to the new model for planetesimal formation based on the direct formation of large planetesimals from the accumulation of small solid particles in turbulent structures of the gaseous disk (Johansen et al., 2007; Cuzzi et al., 2008). The onset of disordered motions is strongly favored in circumstellar disks in binaries due to the formation of strong spiral waves that not only affect the radial evolution of the disk but also influence the vertical structure of the disk, as shown in our models. The quick formation of large planetesimals may bypass the crucial stage of dust coagulation and subsequent planetesimal accumulation, even if it would not solve the problem of the high temperature able to prevent the condensation of icy dust grains.

6.3.2 *Speculations on the long–term evolution*

One limitation of our approach is related to the heavy computational load needed to complete a simulation. Even the 2D simulations performed by Nelson (2000) are limited to a few binary revolutions. The main cause of this is related to the energy equation solution that requires a very short time step owing to the large and short–term variations in internal energy of the gas at the shock waves and at the location where material from one disk impacts the other. In effect, our models and those presented in Nelson (2000) are the only ones where each star of the binary system has its own disk. Simulations of radiative disks with grid codes model only the disk around the primary star, and they do not have to deal with the mass exchange between the two disks. In SPH simulations it would in theory be possible to speed up the computations by implicitly solving the energy equation. However, this approach fails to properly follow the behavior of the gas internal energy in the highly perturbed environment of disks in binaries, as discussed in more detail in the next section. Concerning the long–term evolution of the system we have studied, it is encouraging that 2D simulations of radiative and self–gravitating disks in binaries (Müller and Kley, 2012; Marzari et al., 2012) show stable behavior, that does not evolve significantly even at later stages. This is possibly related to the fast radiative damping of density waves as suggested in Marzari et al. (2012). The disk eccentricity and temperature profiles we obtain in 3D are similar to those observed for disks around the primary star in the previously mentioned papers, and they are self–similar after many binary revolutions. As a consequence, we may infer that the features we find in our simulations, such as the hydraulic jumps, are preserved during the subsequent evolution of the disks. As an additional test, we performed an isothermal simulation of the HIDECL model assuming a temperature profile similar to that of our radiative model at apocenter. After 20 binary revolutions, the main features due to the binary perturbations (spiral waves and vertical excursions) are still present and have the same morphology at any pericenter passage during the full length of the simulation. However, we have to point out that there are significant differences between the radiative and isothermal runs. As already pointed out by 2D simulations, spiral waves are damped more quickly in the radiative model as illustrated in the bottom plots of Fig. 34. The integrated density distribution of the primary disks in the radiative (left) and isothermal (right) models are compared in the same orbital configuration after the pericenter passage. The density waves are significantly less marked in the radiative case, suggesting that they are more effectively damped than in the isothermal one. The scale height of the disk is higher in the radiative case, and the hydraulic jumps have a significantly larger jump factor J_f (see Fig. 20)

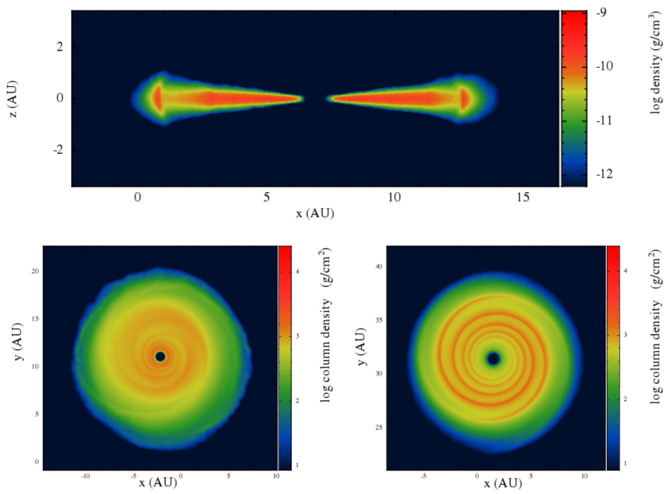

Figure 34: In the upper plot a vertical slice of an isothermal disk with the HIDECL parameters is shown after 20 binary revolutions near the pericenter passage. The two lower plots, illustrating the primary disks shortly after the binary pericenter, show how density waves dissipate more quickly in the radiative disk (left plot) than in the isothermal disk (right plot).

compared to the isothermal case illustrated in Fig. 34 top plot. From Fig. 34 (top plot) it also appears that the density beyond the shock wave is higher in the isothermal model. This may be analytically justified when taking into account that in a radiative disk the ratio between the pre– and post–shock densities can be estimated, according to Durisen (2011), as

$$\frac{\rho_2}{\rho_1} = \frac{\gamma + 1}{\gamma - 1} \tag{100}$$

for $M >> 1$. In an isothermal disk, on the other hand, the ratio can be approximated by

$$\frac{\rho_2}{\rho_1} = \gamma M^2. \tag{101}$$

In this last case, the post–shock density is expected to be higher than in the radiative case.

6.4 INTERMEDIATE STAGE OF PLANET FORMATION

Another important issue to study is the influence of the stellar companion on the accumulation of kilometer-sized planetesimal (Marzari and Scholl, 2000; Thébault et al., 2004, 2006, 2008; Kley and Nelson, 2008; Thébault et al., 2009; Marzari et al., 2009; Xie and Zhou, 2009; Xie et al., 2010b; Paardekooper et al., 2008; Marzari et al., 2012). These studies have shown that this phase might be the most sensitive to binarity effects, because mutual impact velocities can be increased to values that may threaten the formation of large bodies. Crucial in this phase is the evolution of both the eccentricity and perihelion longitude of the planetesimals under the coupled action of the companion gravity and gas drag force. A size–dependent phasing of the orbits develops over the timescale of the secular perturbations of the binary, leading to high (and accretion inhibiting) collision velocities among any planetesimal population with even a small size spread (Thébault et al., 2006). Mechanisms that could come to the rescue of the planetesimal accumulation process are a small inclination between the circumstellar disc and the binary plane (Xie et al., 2010b), or an outward migration of protoplanetary embryos formed in safer regions closer to the star (Payne et al., 2009), or planetesimal growth through the sweeping of small collisional fragments (Paardekooper and Leinhardt, 2010; Xie et al., 2010a), or the fact that the binary was initially wider and was compacted by stellar encounters during the early evolution of the stellar cluster it was born in (Thébault et al., 2009). Another, more radical solution would be that planet formation proceeds through a different channel in close binaries, a hypothesis that could be supported by the fact the exoplanets found in close binaries have different properties than those around single stars (Duchêne, 2010).

7

PLANET FORMATION IN BINARY STAR SYSTEMS : CIRCUMBINARY CASE

7.1 INTRODUCTION

Recently, the KEPLER team announced the discovery of another category of exoplanets in binaries, i.e, transiting circumbinary planets, which move on P–type orbits circumventing both the stars. The first of such planets to be discovered was Kepler–16 b (Doyle et al., 2011) followed by Kepler–34 b, Kepler-35 b (Welsh et al., 2012), Kepler–38 (Orosz et al., 2012a), and Kepler–47 b,c, the first circumbinary multi–planet system (Orosz et al., 2012b). Lately, also the planet Kepler–413b (Kostov et al., 2014) has joined this growing group. The formation of planets in circumbinary P–type orbits might be very different compared to that in S–type orbit (around a component of the pair) since the secular perturbations of the companion star on a planetesimal swarm have different intensity and form compared to that produced by an external perturber. As a consequence, the outcomes of numerical modeling of planetesimal evolution in S–type orbits cannot be applied to study planet formation in circumbinary orbits.

At present, numerical studies have been performed to estimate where in the initial circumbinary disk around Kepler–16 planetesimal accumulation can proceed, even if perturbed and possibly at a slower pace, towards the accumulation of large planetary embryos. Both studies (Meschiari, 2012; Paardekooper et al., 2012) used an N–body approach to compute the trajectories of a large number of planetesimals perturbed by the non–spherically symmetric gravitational field of the stellar pair. The first paper (Meschiari, 2012) focused on the long term effects of the secular perturbations finding potential accretion-friendly zones within 1.75 AU from the star pair and beyond 4 AU. In these regions the mutual impact velocity between planetesimals were, in the majority of collisions, lower than the threshold velocity causing disruption. Their eccentricity distribution is centered around the forced component of the secular perturbations of the binary given by

$$e_f = \frac{5}{4}(1-2\mu)\frac{a_B}{a}e_B, \tag{102}$$

where $\mu = m_2/(m_1 + m_2)$ is the binary mass ratio, a_B and e_B the semimajor axis and eccentricity of the binary system and a is the semimajor axis of the planetesimal (Moriwaki and Nakagawa, 2004).

In a subsequent paper, Paardekooper et al. (2012) re–analyzed planetesimal accumulation around Kepler–16 and also explored two other systems, Kepler–34 and Kepler–35. They focused on the effects of short term eccentricity perturbations on the planetesimal motion. They also considered the possible reaccumulation of small fragments, produced by the shattering of planetesimals impacting at high relative velocity, onto the largest intact planetesimals. Even if this second-generation accretion helps, Paardekooper et al. (2012) conclude that planet formation is not possible at the present location of the planet, but may however be effective beyond twice the present semimajor axis ($a = 0.7$ AU). Both the previously mentioned studies (Meschiari, 2012; Paardekooper et al., 2012) claim that, in spite of the combined perturbations of the binary star system and of the friction from the gas of the circumbinary disk, planet formation seems to be possible beyond a distance of about 2–4 AU from the barycenter of the pair, which is further out than the present location of the exoplanets but still relatively close to the binary.

The basic assumption of an N-body approach to the problem of planetesimal accumulation requires that the gas disk in which the planetesimals are embedded is axisymmetric. This approximation may not be a good one when dealing with circumbinary disks since the gravitational perturbations of the star pair may strongly affect the disk shape. As already shown in (Kley et al., 2008; Marzari et al., 2009, 2012; Müller and Kley, 2012), the disk may become eccentric and be perturbed by strong spiral waves. In that paper, the parameters of the system were similar to those of Kepler–16 but the disk was truncated at 3 AU and the isothermal approximation was used. In this thesis we adopt a more complete approach modeling the circumbinary disk that gave origin to the planet in Kepler–16 as a radiative disk extending out to 10 AU from the barycenter of the two stars. The radiative model is better suited to describe the earlier stages of the disk evolution when it is massive and probably optically thick. It has also been shown (Marzari et al., 2012; Müller and Kley, 2012) that radiative disks, when perturbed, develop overall shapes and internal structure that differ from those of locally isothermal disks, in particular concerning the disk eccentricity and the propagation of spiral waves which may significantly perturb planetesimal trajectories. For this reason, in order to obtain an accurate modeling of the disk structure, in our simulations we solve an energy equation that includes the viscous heating of the disk and radiative losses. On the basis on the above mentioned references we expect that a detailed treatment of the disk thermodynamics is more relevant for the evolution of the disk eccentricity than the inclusion of the effects of self–gravity. In addition, considering a larger disk allows a better handling of the gravitational perturbations of the disk on the planetesimal orbits. If the disk is more massive, since we model a larger portion of it, the perturbations due to a potentially uneven mass distribution, due to the building up of an eccentric shape, are considerably stronger.

In this thesis we compute the trajectories of a large number of planetesimals perturbed by the primordial circumbinary disk. Our simulations focus on the Kepler–16 system and show that the gravitational perturbations of the disk excite large eccentricity values in the planetesimal swarm with a mechanism similar to that described by Nelson and Gressel (2010). These large eccentricities, up to 0.4 and beyond, are able to prevent the onset of accumulation within 10 AU from the stars and maybe also farther out. The present planet observed in the system possibly formed in the outer regions of the disk and migrated inside as described in Pierens and Nelson (2007, 2008). The migration possibly occurred in all the circumbinary systems mentioned above and is strongly suggested by the coincidence between the semimajor axis of the planets and the location of the internal stability limit which can be derived from Holman and Wiegert (1999). As a consequence, our results do not suggest that planet formation is not possible, but that it had to occur in the outer regions of the disk where the perturbations of the star pair are less effective in producing non-axisymmetric density perturbations on the disk.

In Section 2 we describe the numerical model and in Section 3 we describe out results. Section 4 is devoted to the discussion of the results.

7.2 THE HYBRID ALGORITHM MODELING THE EVOLUTION OF THE DISK AND PLANETESIMALS

To compute the trajectories of planetesimals and, at the same time, the evolution of the gaseous disk under the perturbations of the binary, we have used the two-dimensional numerical code FARGO (Masset, 2000) modified to fit the problem. The hydrodynamical equations are solved in a cylindrical coordinate system centered on the barycenter of the binary. We focus on the Kepler–16 system where the mass of the primary is $M_1 = 0.69 M_\odot$, that of the secondary $M_2 = 0.20 M_\odot$, the binary semimajor axis $a_B = 0.224 AU$ and the eccentricity $e_B = 0.159$. The two stars are evolved on a fixed Keplerian orbit neglecting any change in the binary system due to gas accretion by the stars and any momentum exchange with the disk. This choice is justified by the models of Pierens and Nelson (2007) suggesting that a system made of the binary and the disk reach a near-stationary state after some evolution. Incidentally, these authors used binary parameters actually close to those derived for Kepler–16.

The grid used in our calculations to model the disk has $N_r = 256$ radial zones and $N_s = 512$ azimuthal zones, and an arithmetic spacing is used along the radial direction i.e. the radial distance is divided in equal size intervals. All the simulations are carried out including an energy equation of the form (Baruteau and Masset, 2008; Marzari et al., 2012)

$$\frac{\partial e}{\partial t} + \nabla \cdot (e\mathbf{v}) = -p\nabla \cdot \mathbf{v} + Q^{+}_{\text{visc}} - Q^{-}_{\text{cool}} + \lambda e \nabla^2 \log(p/\Sigma^{\gamma}) \quad (103)$$

where $e = p/(\gamma - 1)$ is the thermal energy density, $\gamma = 1.4$ is the adiabatic index, and $\mathbf{v}$ denotes the gas velocity. In the equation we do not include the effects of stellar irradiation. The term Q^{+}_{visc} is the heating term due to the viscous heating while the cooling term Q^{-}_{cool} is assumed to be $2\sigma_{SB}T^4_{\text{eff}}$, where σ_{SB} is the Stefan–Boltzmann constant and T_{eff} is the effective temperature estimated as (Hubeny, 1990)

$$T^4_{\text{eff}} = T^4/\tau_{\text{eff}}, \quad (104)$$

for an effective optical depth

$$\tau_{\text{eff}} = \frac{3\tau}{8} + \frac{\sqrt{3}}{4} + \frac{1}{4\tau}. \quad (105)$$

The vertical optical depth, τ, is approximated as $\tau = \kappa\Sigma/2$, where for the Rosseland mean opacity, κ, we adopt the formulae in Bell and Lin (1994). Following Paardekooper et al. (2011), we also model thermal diffusion as the diffusion of the gas entropy, s, defined as $s = \mathcal{R}(\gamma - 1)^{-1}\log(p/\Sigma^{\gamma})$. This corresponds to the last term in the right-hand side of eq. (103), where λ is a constant thermal diffusion coefficient. Throughout this study, we adopt $\lambda = 10^{-6}$ in code units. The initial aspect ratio $h = H/r$ is constant all over the disk and is set to 0.05. A constant shear kinematic viscosity of 10^{-5} (normalized units), which corresponds at about 5 AU within the disk to an α value of about 2.5×10^{-3} (Shakura and Sunyaev (1973)), is used and open boundary conditions are adopted with standard outflow at both the inner and outer edge. The initial temperature profile of the disk is computed as $T(r) = T_0 r^{-1}$ where the value at 1 AU is set to $T_0 = 630$ K. This value is derived following the approach described in Marzari et al. (2012) and it depends on the initial choice of the aspect ratio h. The Toomre parameter Q is quite large in the inner disk parts, where the binary's perturbation is the strongest. Its radial dependence is approximately $Q(R) \sim 100 \times (R/1\text{AU})^{-3/2}$ and a value of about 10 is measured at $R = 5$ AU.

We neglect in our model the apsidal precession of the binary due to its interaction with the disk. According to Rafikov (2013), the period of the binary precession due to an axisymmetric disk is given by

$$T_{\tilde{\omega}} = 8\pi \left(\frac{M_B}{M_d}\right)\left(\frac{r_o^{1/2} r_{in}^{5/2}}{a_B{}^3\tilde{\phi}n_B}\right) \quad (106)$$

where M_d is the disk mass, M_b the sum of the star masses, n_B the mean motion of the binary, r_{in} the inner border of the disk and r_o the outer one, and $\tilde{\phi}$ is a constant whose value depends on the ratio of

a_B and r_{in} and on the mass ratio and it can be approximated by 0.5. Using this equation we find that $T_{\bar{\varpi}} \sim 3 \times 10^4$ yrs (after some initial evolution, the mass of the disk settles to $M_d = 2.75 \times 10^{-2} M_{\odot}$). This is longer than the timescale over which the planetesimal eccentricity grows i.e. 10^3 yrs. We expect that the binary precession might have an effect on the long term evolution of the system but not on the short timespan we are covering with the model. In addition, since the disk in our simulations is eccentric, eq. (106) may not be very precise being derived under the assumption of an axisymmetric disk. As a consequence, a full numerical approach is needed since the formula for the potential of a axisymmetric disk, used in Rafikov (2013), cannot be applied. We plan to explore this effect in the future hoping in an increase in computing power.

The forces acting on the planetesimals include the binary gravitational force, the gravitational force exerted by the disk and the gas drag force. The latter is calculated in the Stokes regime (see eq. 64) where the gas density in the midplane ρ_g is derived from the surface mass density $\Sigma(r)$ through the relation (Günther and Kley, 2002)

$$\rho_g = \Sigma(r)/[(2\pi)^{1/2} H]. \qquad (107)$$

Respect to (Marzari et al., 2008) we adopt a more extended disk ranging from 0.5 to 10 AU from the binary system with a superficial density profile $\Sigma = \Sigma_0 r^{-1/2}$ where Σ_0 is the density at 1 AU set to $\Sigma_0 = 2.5 \times 10^{-4}$ in normalized units, i.e. $\sim 2.2 \times 10^3$ g/cm^2, compatible with the Minimum Mass Solar Nebula density.

To refine the computation of the drag force acting on the planetesimals we extrapolate the density and velocity $(\rho, \mathbf{v})$ of the gas at the planetesimal location with a bilinear fit from the values at the borders of each grid cell. This is a refinement of the algorithm used in Marzari et al. (2008).

7.3 THE RESULTS

In this section we compute the orbital evolution of the planetesimals and of the disk. Before including the planetesimals in the model, we evolve the disk for 10^5 binary revolutions (approximately 10^4 yr). We then restart the simulation including 400 planetesimals on initially circular orbits with semimajor axis equally spaced from 1 to 8.8 AU and we compute their orbits and the disk evolution for 10^4 yrs.

7.3.1 *The disk shape*

In the upper panel of Fig. 36 we show isocurves of the surface density distribution of the disk confirming its eccentric shape responsible for strong gravitational perturbations on the planetesimal orbits. In the bottom panel we show the azimuthally–averaged disk eccentricity as a function of the distance from the stars, computed as in Marzari et al. (2012), for 3 different evolutionary times separated by 200 yr. The 3 curves suggest a strong variability of the internal disk shape with time. This is due to the propagation of density waves within the disk and was observed also in Marzari et al. (2012) for circumstellar disks in binaries. The behaviour shown in Fig. 36, lower panel, differs from that illustrated in Pelupessy and Portegies Zwart (2013) but the two disk models are substantially different. Pelupessy and Portegies Zwart (2013) adopt a locally isothermal equation of state with a fixed temperature profile $T(r) \sim 300 \times R^{-3/4}$ while our initial temperature profile is $T(r) \sim 630 \times R^{-1}$ and then it evolves in time due to radiative cooling and various sources of heating, including that arising from shock waves. In Fig. 35 we compare the temperature profile of the isothermal disk model by Pelupessy and Portegies Zwart (2013) with the averaged (over 200 yr) equilibrium profile of our radiative model. The difference in both absolute values and slope are noteworthy and this justifies the significant differences in terms of disk eccentricity. It has been shown in Marzari et al. (2012) that

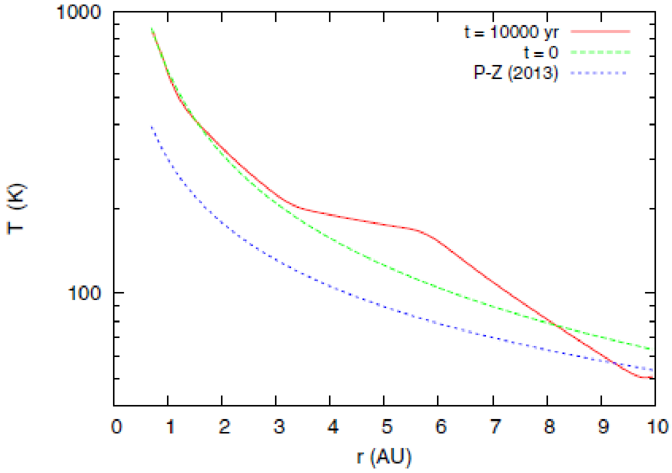

Figure 35: Azimuthally and time averaged (200 yr) temperature profile of our radiative model at $t = 10000$ yr (continuous red line) compared with the initial $t = 0$ yr non–equilibrium one (dashed green line) and the isothermal temperature profile adopted by Pelupessy and Portegies Zwart (2013) (dotted blue line).

the temperature profile and the adopted energy equation have strong effects on the disk eccentricity in perturbed disks. A different thermodynamical model may lead to significant differences in the disk evolution and in particular in the eccentricity which may change by more than a factor 10. The temperature profile of our radiative disk is significantly higher compared to that of Pelupessy and Portegies Zwart (2013) and this plays in favor of a higher disk eccentricity in our model. On the other hand, Marzari et al. (2012) have shown that wave propagation through adiabatic compressions and expansions may be more efficiently damped in presence of radiative losses. This might cause a reduction of the disk eccentricity. All these physical phenomena that can lead to a different disk shape are more important than the disk self–gravity which would have less influence on the disk eccentricity than the thermodynamical model. In addition, self–gravity would not significantly affect the planetesimal dynamics in the inner regions due to the large value of the Toomre parameter Q. The initial different temperature profile is not the only difference between our model and that of Pelupessy and Portegies Zwart (2013), also the superficial density is difference as theirs declines as r^{-1} while ours follows a $r^{-1/2}$ law.

In a real disk, not only viscous heating and radiative cooling determine the disk thermal structure, but also stellar irradiation. Recently, Bitsch et al. (2013) have shown that stellar irradiation dominates in the outer regions of a disk while viscous heating rules close to the star where the structure of disks with and without stellar irradiation are similar. They find via numerical modeling that only beyond approximately 8 AU from the star stellar irradiation begins to have some influence on the evolution of a disk. However, a significant flaring of the disk is observed only for massive disks with $\Sigma_0 \sim 3000 g/cm^3$ and low viscosity ($\alpha \sim 0.001$). In this case the flaring appears consistent beyond 30 AU from the star. In our model, the circumbinary disk of 16 Kepler extends out to 10 AU so it is expected not to be strongly influenced by stellar irradiation but to be dominated by the viscous evolution. In addition, in circumbinary disks density waves excited by the tidal gravity field of the binary propagate within the disk. In three dimensions these waves act like fundamental modes which correspond to large surface distortions in the disk (Lubow and Ogilvie, 1998). Boley et al. (2005) have also shown that shock waves in 3–D disks cause sudden increases in the disk scale height, a phenomenon called hydraulic jump. If the spiral waves excited by the binary perturbations are also shock waves, the hydraulic jumps in the vertical direction can shield the outer disc from stellar irradiation. Disk self-shadowing due to spiral density waves may strongly reduce the relevance of stellar irradiation in circumbinary disks.

The relatively fast changes of the disk eccentricity and of the disk gravity field has an additional perturbative effect on the planetesimals trajectories favouring eccentricity excitation. The orientation of the disk changes slowly with time on a timescale longer than 10^4 yrs. However, the computation of the planetesimal orbits is very time consuming and the timespan of each model is limited by the amount of CPU requirement. This is also the reason why we neglect the self-gravity of the disk in our simulations. A model without planetesimals has however shown that self–gravity does not significantly affect the shape and time variability of the circumbinary disk adopted in our simulations.

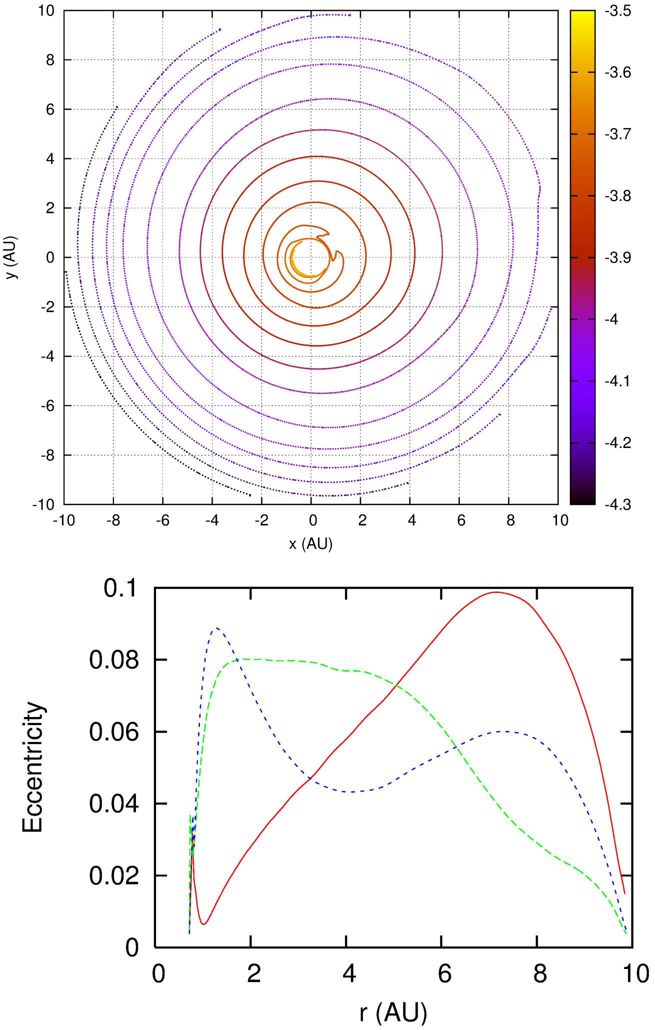

Figure 36: In the upper panel we show isocurves of the disk density distribution (in normalized units) after 2×10^5 binary revolutions illustrating the eccentric shape of the disk. In the bottom panel the azimuthally–averaged disk eccentricity is drawn as a function of the radial distance at 3 different evolutionary times separated by 200 yr.

7.3.2 *Orbital evolution of* 5 *km size planetesimals*

The three major sources of perturbations on the planetesimal orbits are:

- the secular and short term perturbations of the gravity field of the binary,
- the gas drag force,
- the disk gravitational force.

The first kind of perturbation is accounted for also in pure N–body models (neglecting the mutual gravitational attraction of planetesimals) and its effects are summarized by Eqs. 1 and 2. The second term is instead handled very differently in a purely axisymmetric approach and our model. If the axisymmetric approximation is adopted, the gas velocity is assumed to point always in the tangential direction respect a circle centered in the binary barycenter and with radius equal to the planetesimal osculating radial distance. Its modulus is the local Keplerian velocity reduced by a factor that accounts for the pressure term $v_g = v_K(1-2\eta)^{1/2}$ where η is of the order of 10^{-3}. In our model, the gas velocity is computed directly from the solution of the hydrodynamical equations. This is an important aspect since the gas velocity, due to the disk elliptic shape and the presence of spiral waves, is very different from that computed in the axisymmetric approximation. The gas velocity is no longer circular and it can have a significant radial component. Its modulus can be much larger than the value estimated by the previous simplified formula. In addition, the cylindrical symmetry is lost and the direction and modulus of the gas velocity depend on the azimuthal angle.

The third perturbative component on the motion of planetesimals, that we will show to be the dominant one, is due to the gravity field of the disk. An asymmetric distribution of mass causes a significant perturbation of planetesimal trajectories. A similar phenomenon was also observed by Nelson and Gressel (2010) in fully turbulent disks where embedded planetesimals develop large mutual encounter velocities due to stochastic gravitational forces caused by turbulent density fluctuations. In our scenario the density has a shaped asymmetric pattern and this is a worse source of perturbation since its effect does not average to 0. In addition, the orientation of the perihelia play an important role in our scenario (Thébault et al., 2006; Marzari and Scholl, 2000), in particular when large eccentricities are excited. The gravitational perturbations of the eccentric disk significantly decrease the level of perihelia alignment of same size planetesimals and this has important consequences on the accretion process. In Fig. 37 we illustrate the distribution of the eccentricity and perihelion longitude vs. semimajor axis for 5 km size (radius) planetesimals. A peak in eccentricity with a value around 0.4 is observed in between $2--3$ AU

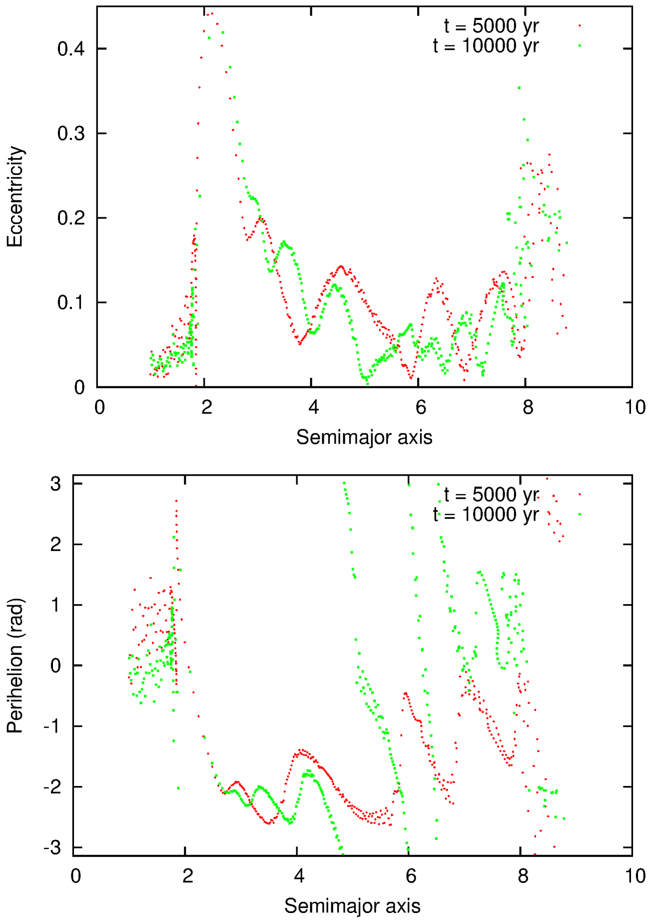

Figure 37: In panel 1 we show the distribution of the eccentricity vs. semimajor axis of 5 km size (radius) planetesimals at two different times. In panel 2 the distribution is that of the perihelion longitude vs. semimajor axis.

with planetesimals quickly drifting inwards. The semimajor axis drift rate is in fact strongly dependent on the eccentricity of the body in the equation given by Adachi et al. (1976) describing the effect of the gas drag

$$\frac{da}{dt} = -\frac{2}{\tau_{drag}}(\eta^2 + \frac{5}{8}e^2 + \frac{1}{2}i^2)^{\frac{1}{2}} \times (\eta + \frac{17}{16}e^2 + \frac{1}{8}i^2) \tag{108}$$

where

$$\eta = \frac{v_{kep} - v_{gas}}{v_{kep}} \tag{109}$$

measures of the amount by which gas orbits the star (or star pair) more slowly than a solid body due to the gas's partial pressure support with v_{kep} being the local Keplerian velocity. The timescale τ_{drag} is given by

$$\tau_{drag} = \frac{8\rho R}{3C_D \rho_{gas} v_{kep}} \tag{110}$$

The region developing large eccentricities is then depleted on a short timescale. The irregular shape of the disk in the inside region is at the origin of the large eccentricity values that lead to the fast inward drift. Farther out, the eccentricity is lower but still high compared to the pure N–body predictions. In this region the radial drift is reduced. The pericenter longitude is only partly aligned and the phasing depends on time since it changes with time. Only the region between 3 and 5 AU seems to maintain some level of coherence over time. This coherence leads to lower impact velocities.

7.3.3 *The influence of the disk gravity unveiled*

By inspecting Fig. 37, the first question that comes to mind is: is it the radial component of the gas drag force or the gravitational attraction of the disk that is responsible for the large values of the planetesimal eccentricities? To answer this question we run an additional model where the gravity of the disk on planetesimal is switched off. Fig. 39 shows the difference in the two cases after 1×10^3 yrs of evolution. The case with the gravity of the disk acting on planetesimals show much larger eccentricities than the test case without the disk gravity. Note that the eccentricity profile in the model where the disk perturbations are included differ from that shown in Fig. 37 since the evolutionary times are different (10^4 yr in Fig. 37 and 10^3 yr in Fig. 39).

While it is possible to analytically estimate the effects of a non–linear gas drag due to an eccentric precessing gaseous disk (Beaugé et al., 2010), it is a prohibitive task trying to predict analytically the details of the gravitational perturbation of an asymmetric disk. The gravity field felt by each planetesimal is a combination of the tidal field of the binary stars, of the eccentric disk and of its spiral arms which are tightly wound close to the stars. Planetesimals are well embedded in the disk and then they are sensitive not only to the overall shape of the disk but also to its fast time variability. In Fig. 38 top panel we show azimuthally averaged radial profiles of the potential produced by the disk at different evolutionary times. To give an idea of the variation of the potential with azimuth we plot also the variation of the potential with azimuth respect to the local average value at two different times. The inner zone, within ~ 1.8 AU, show a slow decrease of the potential with a limited azimuthal variability. This is the region where the planetesimals are less excited in eccentricity. Just beyond 2 AU, the potential begins to rise and the dynamics of planetesimals reacts to this trend change with a steep increase in eccentricity. It is possibly the combination of radial and azimuthal variations that account for the sudden raise in the planetesimal eccentricity, even if it appears difficult to analytically predict the amount of perturbation felt by the planetesimal trajectories. This because the whole shape of the potential changes with time. In addition, there is no analytic expression available for the gravity field of an elliptic disk *within* itself. While the outside potential might be fitted with the analytically expression derived by McCoullogh (Murray and Dermott, 1999), inside the disk the task appears much more complex. Not only a secular theory predicting the eccentricity perturbations of an elliptical disk on bodies located inside the disk itself is intrinsically very complex but to make the task even more difficult the disk changes with time and, as a consequence, also the potential, as shown in Fig. 38. Even if the effects of the non–radial component of gas drag are not relevant in exciting large eccentricity values and the disk gravity does all the job, this does not mean that the gas drag can be neglected when modeling the planetesimal evolution. Large values of eccentricity powers up the gas drag effect on the semimajor axis a since da/dt is proportional to e, as discussed in the previous section. As a consequence, the eccentricity excitation leads also to a fast inward migration related to the eccentricity value. Does the non–radial component of gas drag contributes at later times to excite the eccentricity to the values observed in Fig. 37–a? When the eccentricity is excited by the disk gravity, the large value of η is mostly due to the radial velocity induced by the eccentric orbit of the planetesimal rather than the irregular value due to the the disk. As a consequence, we expect again that the dominant term is the disk gravity and that gas drag still acts as a damping force. This is further confirmed by the case of 25 km size planetesimals discussed in the next section. It has to be noted that the simulations shown in Fig. 39 show the eccentricity value after 10^3 of evolution while those in Fig. 37 and Fig. 40

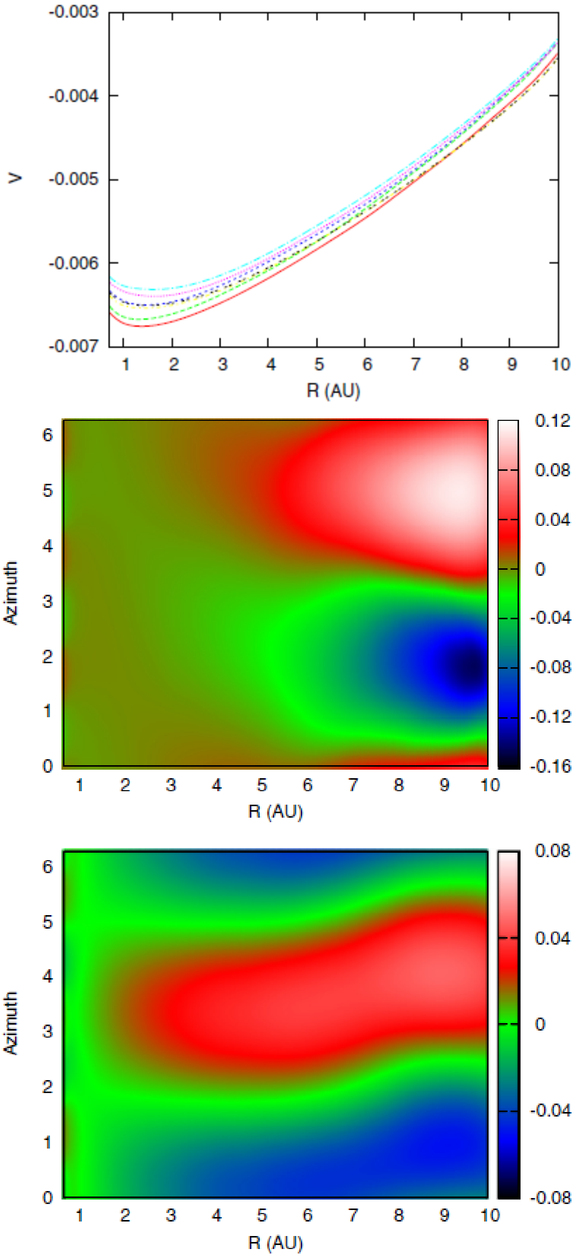

Figure 38: Azimuthally averaged radial profile of the disk potential (given in normalized units) at different evolutionary times sampled every 500 yrs. Some change in the potential is also due to the mass loss through the inner and outer borders of the computational grid. The two bottom plots illustrate the azimuthal variation, computed as $\Delta V = (V - \bar{V})/\bar{V}$, at $t = 2500$ and $t = 4000$ yr, respectively. The azimuthal variation is not regular and depends on the evolutionary time.

illustrate the eccentricity distribution at later times (10^4) when the planetesimal evolution reaches an almost stationary state.

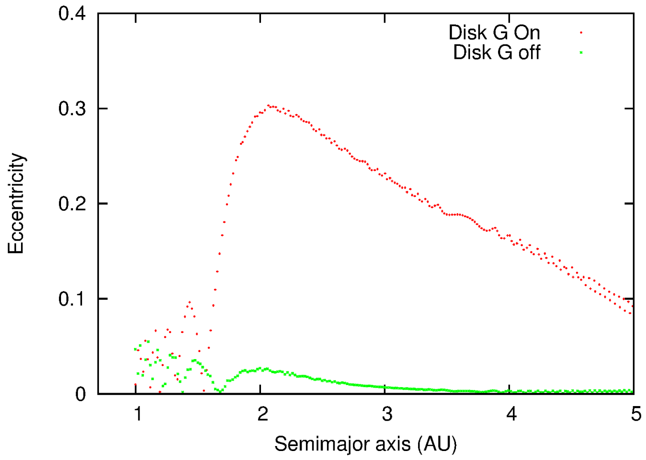

Figure 39: Test run to verify the impact of the disk gravity on the planetesimal dynamics. The outcome of the full model is compared with that of a model without the gravitational attraction of the disk on planetesimals. In this second case the forced eccentricity is significantly reduced. The comparison is performed after 1000 yrs of evolution and for 5 km size planetesimals.

7.3.4 *Evolution of 25 km size planetesimals*

As a further test that the disk gravity is responsible for the large eccentricity values of the planetesimals, we ran an additional simulation for larger bodies 25 km in radius. In Fig. 40 we compare the eccentricity and pericenter distribution of the two different size swarm. The eccentricities are much larger and in effect 5% of the bodies are injected in hyperbolic orbits. Their orbits, located in between 2–3 AU where the eccentricity excitation is the highest, are perturbed by the disk until they reach an eccentricity of about 0.6–0.7 so that, at pericenter, they come close to the binary. Repeated pericenter passages further pump up their eccentricity because of the interaction with the binary until a close encounter with the secondary star ejects them out of the system. In addition, the pericenters are not phased at all for large planetesimals. This is due to the reduced effect of the gas drag which was partly able to damp the eccentricities of the smaller 5 km size planetesimals but it is unable to perform this task for 25 km size bodies. As a consequence, the disk gravity is more effective for the large planetesimals in exciting their orbits.

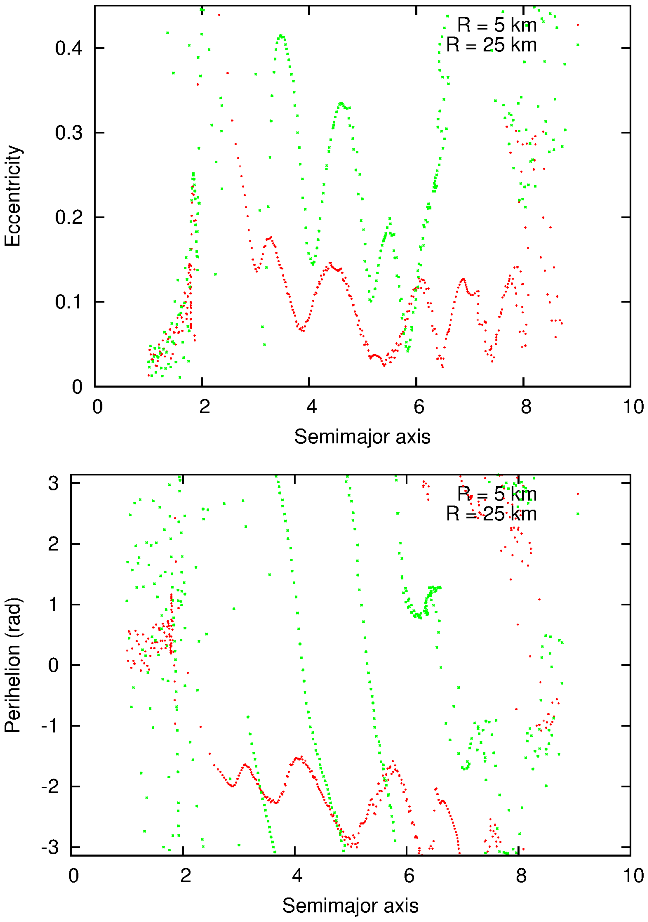

Figure 40: In panel 1 we compare the distribution of the eccentricity vs. semimajor axis of 5 km and 25 km size (radius) planetesimals at $t = 10^4$ yrs. In panel 2 the distribution is that of the perihelion longitude vs. semimajor axis.

7.3.5 *Impact velocities*

The dynamical behaviours identified in the previous sections have to be interpreted in terms of how they affect mutual accretion of planetesimals. The outcome of mutual planetesimal collisions depends on both their impact velocities and their respective sizes. Ideally, one would thus like to follow a whole population of planetesimals with a given size distribution and record all collisions for all impacting pairs of sizes R_1 and R_2. Unfortunately, because of the high CPU cost of computing planetesimal orbits in this sophisticated set-up, only 400 can be followed simultaneously. This is not enough to consider a size distribution amongst them and have enough statistics on dv_{R_1,R_2} everywhere in the disk. We thus considered 2 simplified cases where all planetesimals have the same size, one for "small" planetesimals with $R = 5$ km, and one with a "large" planetesimals with $R = 25$ km. The consequence of this simplification is to underestimate impact velocities among planetesimals, as gas drag tends to minimize these velocities for equal-sized impactors while increasing them for differentially–sized objects (Thébault et al., 2006). As such, our estimates should be considered as a best case (that is, accretion–friendly) scenario.

To derive an estimate of the mutual impact velocities between the "small" and "large" planetesimals orbiting the binary from the orbital parameters of the test bodies in our hybrid model, we used a post–processing code computing all possible crossings among the test planetesimals of our sample. For each pair of orbits, the code looks for the crossing location and computes the relative velocity from 2–body Keplerian formulas. In this way we build up a statistical sample of possible impact velocities which characterize the planetesimal swarm around the binary. These velocities are then compared to the critical velocity $v_{crit(R)}$, corresponding, for impacts between equal–sized bodies of size R, to the limiting value above which impacts result in net mass erosion instead of mass accretion. To derive $v_{crit(R)}$, we use Eqs.1 and 2 of Leinhardt and Stewart (2012), which lead to $v_{crit(5km)} \sim 25$ m s^{-1} for 5 km size planetesimals and $v_{crit(25km)} \sim 125$ m s^{-1} for 25 km size planetesimals. In Fig. 41 we show the relative velocities among equal size $R = 5km$ (upper panel) and $R = 25km$ (lower panel) planetesimals. We see that, for both cases, large values of impact speed are excited in the proximity of the inner border of the disk, i.e., below $\sim$ 2AU. This high velocity regime for equal-sized bodies is the direct consequence of the gas disk gravity, because pure gas drag would have lead to perfect orbital phasing for a given planetesimal size, and thus very low Δv for same size bodies. However, the effect of gas drag is still noticeable, as it is responsible for the fact that average Δv are higher for 25 km planetesimals, $\sim 600 - 1200$ m s^{-1}, than for 5 km objects, $\sim 200 - 400$

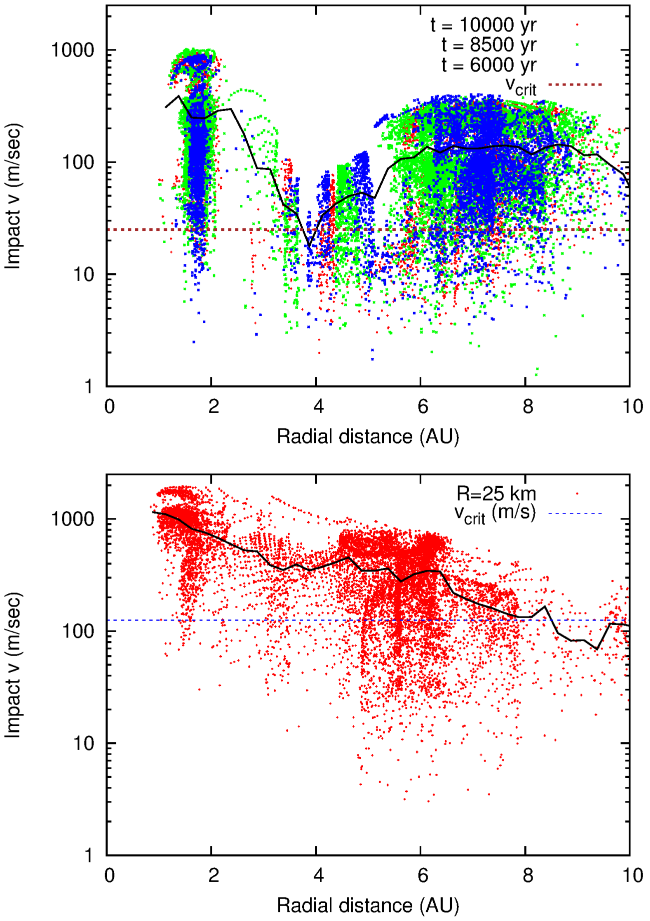

Figure 41: Relative encounter velocities between planetesimals. In panel 1 we compare the relative velocities in the case of small planetesimals at different times. There is a significant time variability in the impact velocity which, however, remains large all the time. In panel 2 we illustrate the relative velocities for $R = 25\mathrm{km}$ planetesimals at $t = 10^4\mathrm{yr}$. The black lines in both plots show the average impact velocity computed in small radial bins. The 2 horizontal lines display the limiting Δv values for the accretion/erosion frontier, as deduced from Leinhardt and Stewart (2012), for 5 km impactors and 25 km ones.

m s^{-1}. This difference can be unambiguously attributed to gas drag, as it is the only size–dependent mechanism acting on planetesimals, so that its damping effect on the eccentricity will be much more pronounced for smaller bodies. However, even for the small planetesimal run, velocities are still much higher than the critical value for erosion $v_{\mathrm{crit(5km)}} \sim 25$ m s^{-1}. This is also true for 25 km planetesimals, despite of the fact that $v_{\mathrm{crit(5km)}}$ is higher, ~ 125 m s^{-1}. The high-Δv regime is maintained, for all planetesimal sizes, in the strongly depleted region between 2 and 3.5 AU. It is followed by a region, between $\sim$ 3.5 and $\sim$ 5.5AU, of lower impact velocities for the small planetesimal case. However, these velocities remain above the erosion threshold, except for the small planetesimal case. However, these velocities remain above the erosion threshold, except for a very narrow region around 4 AU, where $< \Delta v > \sim v_{\mathrm{crit}}$. For the larger 25 km planetesimals, impact speeds are $\geqslant 300 m s^{-1}$, and thus higher than v_{crit}, in this whole intermediate region.

In the outer regions of the simulations, up to 10 AU, impact velocities become comparable for both planetesimal populations. Their values remain relatively high, in the $\sim 100 - 200$ m s^{-1} range, and are above the erosion threshold everywhere, except for the outermost 8.5–10 AU domain, where $< \Delta v >$ become slightly lower than v_{crit} for 25 km objects.

7.4 DISCUSSION AND CONCLUSIONS

The discovery by KEPLER of planets in circumbinary orbits has reawaken the interest regarding the planetesimal accumulation process in such systems. The first numerical investigations of this issue adopted an axisymmetric approximation for the gas disk in which planetesimal are embedded, implicitly assuming that the tidal force of the central binary does not significantly perturbs this disk. We show in this thesis that this is not the case and, due to the presence of the companion star, the circumbinary gas disk becomes eccentric. This has profound implications for the accumulation process of planetesimals due to the excitation of their orbital eccentricity and partial destruction of the perihelia alignment. Our simulations where the disk is evolved together with the planetesimals indeed show that, adding the crucial effect of the gas disk gravity greatly increases impact velocities amongst planetesimals in the circumbinary disc around Kepler 16. For the two planetesimal populations we have considered, 5 and 25 km, the environment is globally very hostile to mutual accretion in the region within 10 AU.

As noted earlier, we have considered a simplified case where all bodies have the same size, so that only a small fraction of all possible planetesimal encounters have been explored. However, in the regions where gas drag has a non–negligible effect on mutual impacting speeds, we expect impact velocities between differentially–sized bodies to be even higher than those amongst equal–sized ones (e.g. Thébault et al., 2006). As a consequence, in these regions our runs probably display a best–case scenario, with a situation that would be even more accretion–hostile in a "real" system with a spread in planetesimal sizes. The $r \leqslant 6\,\mathrm{AU}$ domain clearly corresponds to this case, the important difference between $\Delta v_{5\mathrm{km}}$ and $\Delta v_{25\mathrm{km}}$ being a clear indicator that gas drag is an important factor in imposing the impact speeds. In the region beyond 6 AU, impact speeds for 5km and 25km bodies are comparable, which could at first glance indicate that gas drag has a limited effect there. However, Fig.40 clearly shows that it is not the case, since these two populations have very different eccentricities and periastron in these outer regions, so that gas drag still has an important influence on collision velocities and the fact that $\Delta v_{5\mathrm{km}} \sim \Delta v_{25\mathrm{km}}$ is simply a coincidence. We thus here also expect impact speeds to be higher between differentially-sized objects than for equal-sized ones, so that our single-sized simulations here again probably correspond to the most accretion-friendly configuration possible. The fact that even in this best-case scenario the whole disc below $\sim 9\,\mathrm{AU}$ is strongly hostile to accretion, with the possible exception of a narrow strip around 4 AU, seems to indicate that this result should also hold for any planetesimal population with a spread in its size distributions. Furthermore, even if accretion was to be possible, it is important to stress that it cannot be as efficient as in an unperturbed case. Indeed, planetesimal accumulation will be slowed down, because of the increased encounter velocities due to perturbations which would probably switch off the fast runaway-growth mode that requires very low impact velocities to proceed (see discussion in Thebault, 2011).

Our results should, however, be taken with some caution, as one potentially important effect is not accounted for in our runs, that of the possible re-accretion of collisional fragments that has been identified by Paardekooper et al. (2012). This mechanism would probably help planetesimal growth in this dynamically excited environment, so that its omission overestimates the erosive behaviour of the disk. Unfortunately, it is impossible to implement this effect in the already very complex set-up that has been considered here. We note, however, that other simplifications of our numerical approach might have the opposite effect, i.e., underestimating the erosive nature of the planetesimal swarm. The first one is that we suppose that all planetesimal start on circular orbits at the same time, whereas there might be a spread in their formation epoch (e.g Xie et al., 2010b). Such a spread would lead to increased differential orbits, and thus impact speeds, even between equal-sized objects (Paardekooper et al., 2012). The other simplification is that the spatial resolution in the hydrodynamical model required to correctly compute the disk–planetesimal interactions limits the radial extension of the disk we can model with a reasonable CPU load. Our gas disk is thus probably too small, and we would expect a larger and more massive disk to have more powerful gravitational perturbations on the planetesimal trajectories, possibly increasing the impact velocities.

Given these uncertainties, it is thus too early to reach definitive conclusion regarding the precise balance between accretion and erosion in a realistic planetesimal disk. However, to the very least our simulations have shown that disk gravity plays a crucial role and always act towards increasing impact speeds and the erosive behaviour of the swarm. As such, they strengthen and expand the results obtained by previous works, which already identified that the region where the planet is located is hostile to planetesimal accretion (Meschiari, 2012; Paardekooper et al., 2012). This seems to rule out the *in situ* formation of the Kepler 16 planet following the core-accretion scenario. This result also probably holds for the Kepler-34, Kepler-35 and Kepler-47 planets, given the similarities between these different systems.

A possibility to explain the present position of these planets is that they formed farther out in the circumbinary disk. Subsequent migration due to the interaction with the disk would have brought them back to their present orbits, as shown in (Pierens and Nelson, 2007, 2008). This is also suggested by their mass which is in the Neptune–Saturn range, in agreement with the prediction of (Pierens and Nelson, 2007, 2008). Jupiter size planets in fact would be either ejected from the system or sent on outer orbits. Our simulations show that such migration would have to be very efficient, bringing the planet where it is today from an initial formation region probably located beyond 6 AU from the binary's center of mass.

An alternative scenario may be based on the direct formation of large planetesimals from the accumulation of small solid particles in turbulent structures of the gaseous disk (Johansen et al., 2007; Cuzzi et al., 2008). In circumbinary disks the onset of turbulence may be favored by the tidal gravity field of the central stars and this might lead to the formation of planetesimal large enough to sustain the high velocity impacts occurring in the inner regions of the disk. In this case, planets might form closer to the center of the disk by–passing the critical phase of small body accretion. However, these instability-based scenarios still need to be quantitatively investigated in dynamically perturbed environments such as binaries before any conclusion can be reached.

Part IV

PLANETARY SYSTEM EVOLUTION

8

MECHANISMS ALTERING THE DYNAMICAL CONFIGURATION

8.1 INTRODUCTION

The classic theory of planet formation (see Chap. 5) is a self consistent picture that explains pretty well the Solar–type planets, predicting the development of giant gaseous planets in the outer zones of protoplanetary disks and small rocky ones in the inner parts.

On the other hand, it does not explain the majority of exoplanets observed so far. In effect, the first exoplanet detected (51 Peg b by Mayor and Queloz (1995)) was a giant planet orbiting at a very close separation from his parent star and it was the former of a large class of exoplanet that has been named hot Jupiters.

However, we did not consider some crucial aspects of the early phases of planet formation such as: planetesimal–disk interaction, planetesimal scattering, planet–planet scattering. The net result of these effects is energy and angular momentum exchange between protoplanets or with the leftover of the protoplanetary disk, which drives the evolution of their orbital elements. The final configuration reached by the system after this complex phase could be very different from the original one and it may explain the various classes of exoplanets observed so far, starting from the classic picture of planet formation.

Thus, understanding these processes could be of paramount importance for an extrasolar planets space mission, in order to predict the planet parameter space in different environments, and its evolution with time.

In this chapter I will review the basic theory of planet migration and planet–planet interactions, leaving for the next Chapter an in depth analysis on the influence on planet evolution by other stars passing close–by.

8.2 MIGRATION

The main cause of the evolution of planet orbital elements during the early phases after protoplanet formation is the interaction with the leftover of the gaseous protoplanetary disk. This interaction produce an exchange of energy and angular momentum mediated by the gravitational torques between the planet and the disk which cause planet migration.

A fundamental point is that no torque is exerted on a planet by an axisymmetric disk, so we need one (or more) process that excites nonaxisymmetric structures, such as turbulence, a stellar companion, or the planet itself if it is sufficiently massive (Mars mass or above) to perturb the disk structure. Hence, the latter is the case of a gas giant formed by gravitational instability, or the core of a giant planet in the core accretion model.

8.2.1 *Planet–disk interaction: impulse approximation*

The impulse approximation was first derived by Lin and Papaloizou (1979) and then extended by Papaloizou and Terquem (2006). It is a toy model but it predicts well the general behaviour. Following their derivation, we study the gravitational interaction between the planet and the gas flowing past in a two body problem approach.

We consider a frame of reference moving with the planet and a test gas particle initially on an unperturbed orbit approaching it. For simplicity, we neglect the fact that we are in a corotating frame, so we do not consider the apparent forces acting on the system. Furthermore, we ignore the hydrodynamics except for the disk ability to smooth out the trajectories so that particles resume unperturbed orbits before their next close approach with the planet.

We adopt a Cartesian coordinates system centered on the protoplanet with the x–axis pointed radially outwards, the y–axis in the azimuthal direction following the gas flow and the z–axis pointed in the vertical direction. We assume that the planet has a mass M_p and the gas particle of mass m flows past moving in the trajectory $x = b$, where b is the impact parameter that we consider to be much less than the protoplanet orbital radius, and with the relative velocity $v_y = v$ as represented in Fig. 42. The net result of the gravitational interaction is: an angular momentum transfer between the disk matter and the protoplanet, a deflection in the test particle trajectory by an angle ϕ.

DEFLECTION ANGLE In order to find the deflection angle we firstly derive the perpendicular component of the velocity δv_x induced by the gravitational force orthogonal to the particle trajectory

$$F_x = m\frac{d\delta v_x}{dt} = \mathbf{F}\sin\theta = \frac{GM_p m}{r^2}\sin\theta, \tag{111}$$

where $|\mathbf{r}| = \sqrt{b^2 + s^2}$ is their instantaneous separation and θ is the angle between $\mathbf{r}$ and the local velocity vector $\mathbf{v}$. If we define the time of closest approach as $t = 0$, then the distance along the trajectory from this point will be $\mathbf{s} = \mathbf{v}t$, thus the instantaneous separation is

$$|\mathbf{r}| = \sqrt{b^2 + \mathbf{v}^2 t^2} = \sqrt{b^2\left[1 + \left(\frac{\mathbf{v}t}{b}\right)^2\right]}, \tag{112}$$

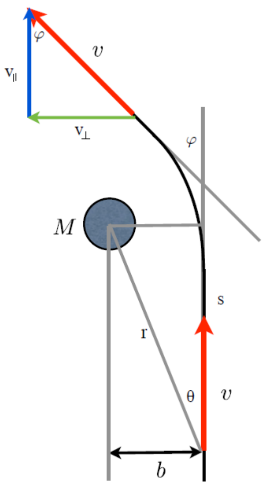

Figure 42: Schematic view of the interaction between a planet and a gas particle approaching it. Source: Mordasini & Klahr lectures.

and given that the angle θ can be expressed as

$$\sin\theta = \frac{b}{|\mathbf{r}|} = \left[1 + \left(\frac{\mathbf{v}t}{b}\right)^2\right]^{-1/2}, \tag{113}$$

we can derive the time–dependent perpendicular component of the force

$$F_x = \frac{GM_p m}{r^2}\sin\theta = \frac{GM_p m}{b^2}\left[1 + \left(\frac{\mathbf{v}t}{b}\right)^2\right]^{-3/2}. \tag{114}$$

Thus, from eqs. (111),(114), we can derive the perpendicular component of the velocity

$$\delta v_x = \int_{-\infty}^{\infty}\frac{F_x}{m}dt = \frac{2}{m}\int_0^{\infty}F_x dt = 2\frac{GM_p}{b^2}\int_0^{\infty}\left[1 + \left(\frac{\mathbf{s}}{b}\right)^2\right]^{-3/2}dt. \tag{115}$$

From the definition of the distance on the trajectory **s** and assuming that the final velocity magnitude is equal to the initial one, that is true for small deflection angles we can redefine the integrated variable as

$$dt = \frac{d\mathbf{s}}{\mathbf{v}}, \tag{116}$$

which gives for the perpendicular velocity

$$\delta v_x = 2\frac{GM_p}{b^2}\int_0^{\infty}\left[1 + \left(\frac{\mathbf{s}}{b}\right)^2\right]^{-3/2}\frac{d\mathbf{s}}{\mathbf{v}}, \tag{117}$$

and redefining the integrated variable as $t = s/b$

$$\delta v_x = 2\frac{GM_p}{b\mathbf{v}}\int_0^{\infty}\frac{dt}{(1+t^2)^{3/2}} = 2\frac{GM_p}{b\mathbf{v}}\left.\frac{t}{\sqrt{1+t^2}}\right|_0^{\infty} = 2\frac{GM_p}{b\mathbf{v}}. \tag{118}$$

Thus, we can approximate the deflection angle ϕ (again for small values) as

$$\phi \approx \frac{\delta v_x}{v - \delta v_y} \approx \frac{\delta v_x}{v} = \frac{2GM_p}{v^2 b}. \tag{119}$$

ANGULAR MOMENTUM TRANSFER The perpendicular component of the velocity is directed radially hence its variation does not correspond to any angular momentum exchange. However, the interaction in the two–body problem is conservative so an increase in the perpendicular velocity must correspond to a decrease in the parallel component. From the conservation of kinetic energy during the encounter and assuming that the perpendicular component of the initial velocity is negligible we can derive

$$v^2 = |\delta v_x|^2 + (v - \delta v_y)^2, \tag{120}$$

which implies for small deflection angles ($\delta v_y^2 << 2v\delta v_y$)

$$\delta v_y \simeq \frac{1}{2v}\left(\frac{2GM_p}{bv}\right)^2. \tag{121}$$

If the planet has a semimajor axis a the implied angular momentum change per unit mass of the gas is

$$\Delta j = a\delta v_y = \frac{2G^2M_p^2 a}{b^2 v^3}. \tag{122}$$

The gas in the zones exterior to the planet orbits more slowly than the planet (in a Keplerian disk) so it is overtaken by it. Thus, the decrease in the parallel component of the relative velocity corresponds to an increase in the gas velocity and in its angular momentum. On the other hand, since the gravitational torque must be equal and opposite for the planet, its velocity is reduced and the same happens to its angular momentum. The net result is an outward migration for the gas and an inward migration for the planet. Considering the gas in the inner zones respect to the planet we found that the gas angular momentum is reduced and the planet angular momentum is increased, so the planet will migrate outward and the gas will migrate inward. Considering both the contribution, the net torque and sense of migration of the planet will depend upon which of the above effects dominates.

TOTAL TORQUE We want to find the total torque acting on the planet due to its interaction with the disk. Assuming a constant gas surface density Σ in the proximity of the planet, the mass of an annulus outside and close to the planet between the radii b and $b + db$, where $b << a$ is given by

$$dm \approx 2\pi a \Sigma db. \tag{123}$$

The total amount of gas in the annulus will reach the close approach to the planet in a time interval

$$\Delta t = \frac{2\pi}{|\Omega - \Omega_p|}, \tag{124}$$

where Ω_p is the planet angular velocity and Ω is the mean gas angular velocity in the annulus. Assuming $b << a$, a first order expansion of the angular frequencies yields

$$|\Omega - \Omega_p| \simeq \left|\frac{d\Omega_p}{da}\right| b = \frac{3\Omega_p}{2a} b. \tag{125}$$

The total temporal change of the planet angular momentum will then be

$$\frac{dJ}{dt} = -\int_0^\infty \frac{\Delta j}{\Delta t} dm, \tag{126}$$

and substituting the previous equations 122, 124,123 with the assumption of quasi Keplerian orbits

$$\Delta v \simeq \left|\frac{d\Omega_p}{da}\right| ab = \frac{3}{2}\Omega_p b, \tag{127}$$

we obtain the wanted relation for the torque acting on the planet

$$\frac{dJ}{dt} = -\int_0^\infty \frac{8G^2M_p^2\Sigma a}{9\Omega_p^2 b^4} db. \tag{128}$$

This integral is divergent due to an unphysical infinite contribution from the gas passing close to the planet. For now, we replace the lower limit with a minimum impact parameter b_{min} and integrating the previous equation we find

$$\frac{dJ}{dt} = -\frac{8}{27}\frac{G^2M_p^2 a\Sigma}{\Omega_p^2 b_{min}^3}. \tag{129}$$

From eq. 129 we can see that the torque on the planet due to its interaction with the gas scales as the square of the planet mass. On the other hand the orbital angular momentum of the planet is by definition linear in the planetary mass. Thus, neglecting all other factors, the time scale on which the planet changes its orbital angular momentum significantly is inversely proportional to the planet mass

$$\tau = \frac{J}{|dJ/dt|} \sim M_p^{-1}. \tag{130}$$

To have an order of magnitude of this timescale, a terrestrial planet orbiting a Solas mass star with a semimajor axis of 5 AU, embedded in a standard protoplanetary disk would have a time scale of ~ 1 Myr, while a Jupiter mass planet with the same orbital parameters would have a time scale of $\sim 2.5 \cdot 10^5$ yr. Noteworthy, this is a low limit since we are considering only the external torque.

Although this is a crude estimate it gives us the idea that gas disk migration is a fundamental process in planet evolution.

8.2.2 *Planet–disk interaction: linear wave theory*

In order to determine the evolution of a planet in a gas disk it results necessary to start from a different point and consider the evolution of linear perturbations caused by the planet within the disk.

A planet embedded in a disk excites density waves through Lindblad and corotation resonances and feels an exerted torque by them as a reaction (Goldreich and Tremaine, 1979; Tanaka et al., 2002).

A resonance occours when a characteristic frequency of the planet matches a frequency whitin the disk. Given a planet in a circular orbit with angular frequency Ω_p embedded in a disk with orbital frequency Ω_d we will have a co–rotation resonance at a distance r where this condition holds

$$\Omega_d(r) = \Omega_p. \tag{131}$$

Thus, in a Keplerian disk the co–rotation resonance is co–orbital with the planet.

Conversely, we talk about Lindblad resonance when the gas disk is excited at its natural frequencies for epicyclic oscillations $\kappa(r)$

$$m[\Omega_d(r) - \Omega_p] = \pm\kappa(r), \tag{132}$$

where m is an integer, and κ is the epicyclic frequency. For a Keplerian disk $\Omega_d(r) = \kappa(r)$, thus the resonances are located at

$$r_L = \left(1 \pm \frac{1}{m}\right)^{2/3} a, \tag{133}$$

where a is the planet semi–major axis. Hence, a planet in a circular orbit embedded in a Keplerian gas disk will excite one co–rotation resonance and a combination of Lindblad resonances closely spaced near the planet location.

However, in most cases the planet has a non zero eccentricity, and we must decompose the planet potential into a set of rigidly rotating components with different pattern speed and frequencies

$$\Omega_p^{l,m} = \Omega_p + \frac{(l-m)}{m}\Omega_p, \tag{134}$$

where l is a second integer. The co–rotation and Lindblad frequencies occur then at the location r where the disk frequencies $\Omega_d(r)$ nearly match one of the planet frequencies $\Omega_p^{l,m}$.

Nonetheless, for small eccentricities, we need to take account only of a small number of planet frequencies since the amplitude of the perturbation scales as $|l-m|$th power of the eccentricity.

The torque contribution on the planet by a resonance will depend on its intrinsic strength and on the gas disk mass at the resonance location. Two limiting cases could be considered.

TYPE I MIGRATION When the planet mass is low and its interaction with the disk weak, the redistribution of angular momentum due to disk viscosity dominates over the local exchange of angular momentum between the planet and the disk. The outcome is that the disk structure is umperturbed, and the planet is embedded in the gas disk, which is present at all resonant locations. For a given disk structure $(\Sigma(\mathbf{r}), T(\mathbf{r}))$, and not considering explicitly viscosity, turbolence, and magnetic fields,

TYPE II MIGRATION When the planet mass is higher than the Mercury mass, the local exchange of angular momentum between the planet and the disk dominates over the angular momentum transport whitin the disk. As a result, the planet profoundly modifies the disk structure, and opens up a gap, severely depleting the inner Lindblad resonances $(l >> 1)$.

TYPE III MIGRATION It is a runaway migration due to an asymmetric surface density distribution in the co–orbital region, which leads to a large corotational torque, that drives the planet into the star on a timescale shorther than the disk evolution time. Such as in Type I migration, the basic structure of the disk is not affected by the planet.

8.3 RESONANT EVOLUTION

A resonance occurs when there is a near commensurability between a characteristic frequency (orbital, spin, precession, . . .) of two or more bodies. Considering, as an example, the mean motion resonance, which is common in extrasolar planets, the condition for resonance is

$$\frac{n_{out}}{n_{in}} \simeq \frac{p}{p+q}, \tag{135}$$

where n_{out}, n_{in} are the mean motions of two bodies, and p, q two small integers. As it can be seen from eq. 135 it is not necessary that the equality is exact.

We talk about resonance when the ratio of the characteristic frequencies oscillates around some fixed value or, equivalently, when the point of conjunction between the two bodies librates around an equilibrium point. On the other hand, the frequencies are out of resonance when the conjunction point circulates, taking all values between 0 and 2π.

8.3.1 *Resonant capture*

The final outcome of a resonance depends mainly on the mismatch between the gravitational interaction of the two planets and the external force due to gas disk torque in a protoplanetary disk. If the former prevails, than the planetary systems ends up in a locked configuration, in a process called resonant capture (Goldreich and Soter, 1966; Borderies and Goldreich, 1984).

In effect, when the two planets are in resonance, a secular exchange of angular momentum between them acts to maintain this condition, preventing the external force that would break the resonance.

The resonant capture occours in general only for convergent orbits and, if it happens during inward migration of the outer planet, than the resonance acts to remove angular momentum from the inner one and the planets migrate inward at the same rate (Peale, 1976). This process explain in an elegant way the presence of short–period extrasolar planets in a main motion resonance configuration.

8.3.2 *Kozai resonance*

Another important resonance that could explain the extrasolar planets parameter space, especially those orbiting binary stars, is the Kozai resonance (Kozai, 1962).

It is a secular resonance that occurs in a hierarchical triple system when the rate of change of the longitude of periapse and ascending node of a tertiary, whose mass is negligible respect to that of a highly inclined secondary external perturber $M_t << M_s$, are in $1:1$ ratio. This could be the case of an inclined binary systems in which a planet orbits one component. It can be shown that the eccentricity and inclination of the tertiary varies significantly, while its period and semimajor axis remain constants.

If the mutual inclination is greater than a critical value $i > i_{crit} \simeq 39.2^o$, than the planet eccentricity and inclination undergo cyclic oscillations with a maximum value (if the tertiary orbit is initially circular) of (Armitage, 2010)

$$e_{t,max} = \left[1 - \frac{5}{3}\cos^2 i\right]^{1/2}, \tag{136}$$

which astonishing does not depend on the star masses, and a characteristic timescale of

$$P_K \sim P_{t,in}\left(\frac{M_p}{M_s}\right)\left(\frac{a_s}{a_{t,in}}\right)^3 (1-e_s^2)^{3/2}. \tag{137}$$

Thus, even a very distant inclined companion could induce a strong Kozai resonance, altough with a long timescale.

This process could be the cause of many highly inclines planets observed so far, that are not explainable with the standard theory of migration. An interesting idea suggest that the formation of hot Jupiter planets could be due to a combined effect of the Kozai resonance by a stellar companion and tidal circularization by the parent star. In effect, the Kozai mechanism do not alter the orbital semimajor axis of the planet. However, if the periapsis of planetary orbit reaches an inner region where the tidal circularization by its parent star comes into play it could force planet migration to the inner regions of the planetary systems where they are observed. This mechanism is observable, since periodically the planet inclination is disaligned respect to its parent star, and it could be detected by radial velocity measuraments during planetary transits with the Rossiter–McLaughlin effect (Rossiter, 1924).

A couple of extrasolar planets, 16 Cyg B b and HD 80606 (Naef et al., 2001), have an high eccentricity which is believed to be due to the Kozai mechanism.

It is to note that if there are other sources of precession, that can be due to additional planetary companions, the Kozai resonance can be overcome.

8.4 PLANETARY SYSTEM STABILITY

The final outcome of a planetary system at the end of the planet formation process is not necessarily a long–term dynamical stable system, since it takes place in a dissipative environment.

Thus, the planet formation is followed by a chaotic phase that could result in a long–term unstable system.

In order to study the evolution of a such system, it is necessary to analyze the stability regions of the three body restricted problem consisting of a massless test particle immersed in the gravitational field Φ of a planet with mass M_p orbiting a star with mass $M_\star$.

8.4.1 *Hill stability*

Lets consider a coordinate system centered on the center of mass, and co–rotating with the planet with an angular frequency Ω in a circular orbit, such that the x–axis coincide with the line joining star and planet. The motion of the test particle is given by

$$\ddot{\mathbf{r}} = -\nabla\Phi - 2(\Omega \times \dot{\mathbf{r}} - \Omega \times (\Omega \times \mathbf{r}), \tag{138}$$

$$\Phi = -\frac{GM_\star}{r_\star} - \frac{GM_p}{r_p}, \tag{139}$$

where $\mathbf{r}$ is the test particle position vector.

In the cartesian coordinates the previous equations translates into

$$\ddot{x} - 2\Omega\dot{y} - \Omega^2 x = -G\left[\frac{M_\star(x + x_\star)}{r_\star^3} + \frac{M_p(x - x_p)}{r_p^3}\right], \tag{140}$$

$$\ddot{y} + 2\Omega\dot{x} - \Omega^2 y = -G\left[\frac{M_\star}{r_\star^3} + \frac{M_p}{r_p^3}\right] y, \tag{141}$$

$$\ddot{z} = -G\left[\frac{M_\star}{r_\star^3} + \frac{M_p}{r_p^3}\right] z, \tag{142}$$

where the star position is $x = -x_\star$, and the planet position $x = x_p$.

Defining a pseudo–potential that considers also the centrifugal force due to the non–inertial reference frame

$$U \equiv \frac{\Omega^2}{2}(x^2 + y^2) + \frac{GM_\star}{r_\star} + \frac{GM_p}{r_p}, \tag{143}$$

the equation of motion of the test particle becomes

$$\ddot{x} - 2\Omega\dot{y} = \frac{\partial U}{\partial x}, \tag{144}$$

$$\ddot{y} + 2\Omega\dot{x} = \frac{\partial U}{\partial y}, \tag{145}$$

$$\ddot{z} = \frac{\partial U}{\partial z}. \tag{146}$$

This system could be further simplified adding the three equations, after having multiplied the first one by $\dot{x}$, the second by $\dot{y}$, and the third by $\dot{z}$

$$\dot{x}\ddot{x} + \dot{y}\ddot{y} + \dot{z}\ddot{z} = \dot{x}\frac{\partial U}{\partial x} + \dot{y}\frac{\partial U}{\partial y} + \dot{z}\frac{\partial U}{\partial z}, \tag{147}$$

$$\frac{d}{dt}\left(\frac{1}{2}\dot{x}^2 + \frac{1}{2}\dot{y}^2 + \frac{1}{2}\dot{z}^2\right) = \frac{dU}{dt}, \tag{148}$$

that could be solved, giving

$$\dot{x}^2 + \dot{y}^2 + \dot{z}^2 = 2U - C_J \tag{149}$$

$$C_J = 2U - v^2, \tag{150}$$

where v is the test particle velocity, and C_J is a constant of motion called Jacobi constant, which is an energy–like quantity.

The Jacobi constant defines the zero velocity surfaces, i.e. the regions of space where $2U = C_J$, which are insurmountable zones for test particles, thus it determines the stability regions.

Considering a test particle in circular orbit with radius a_o, in a system with a planet in circular orbit with radius $a_i < a_o$ such that

$$a_o = a_i(1 + \delta), \tag{151}$$

where δ is a dimensionless separation. Then, the condition for orbital stability is

$$\delta > 2.4\mu^{1/3}, \tag{152}$$

where μ is the planet to star mass ratio. Hence, if the orbital separation are greater than a few Hill radii (since it is proportional to $\mu^{1/3}$), than close encounters do not occour.

However, the conditions for stability in planetary systems with two or more planets, or/and two or more stars are much more complicated and there is no analytical solution for stability regions.

8.4.2 *Planet–planet scattering*

Altough the small semi–major axes observed in the hot Jupiter planet class could be explained via planet migration process, their high eccentric orbits are an open problem.

A possible solution is given by the Jumping Jupiter model (Weidenschilling and Marzari, 1996; Rasio and Ford, 1996; Marzari and Weidenschilling, 2002), that explains the planet eccentricity excitation as a result of a gravitational scattering process in multiple planetary systems.

In effect, in a planetary system formed by two or more giant planets, the mutual perturbation could lead to eccentricity excitation. As a consequence, the system becomes higly unstable and the planets can experence several close encounters. The system at the end of this chaotic period will be drastically different from the original one.

Weidenschilling and Marzari (1996) found that, for three giant planets orbiting a Sun–like star, the most likely outcome is the ejection of one planet, while the other two remain on stable eccentric and slightly inclined orbits. Other less frequent final configurations are the ejection of two planets or the impact of one of them onto the star. However, a common outcome is that the inner planet results in a closer configuration since it loses angular momentum to the ejected planets (see Fig. 43).

This mechanism could also explain a fracion of "hot Jupiters" in close circular orbit if the tidal dissipation is sufficiently effective.

(Marzari et al., 2005) extend the study of the Jumping Jupiter model also for planetary systems hosted by binary stars. They found that in these systems the planetary ejection is favored by the gravitational perturbation of the companion star. The final outcome of system with three initial planets, which strongly depends on the binary eccentricity, is more likely to leave a single or no one planet at the end of the chaotic orbital evolution respect to the single stellar case. The planet orbital configuration at the end of this phase are stable according to the Holman–Wiegert criterion. There are some relevant exceptions when there is a mutual inclination between the binary and planet

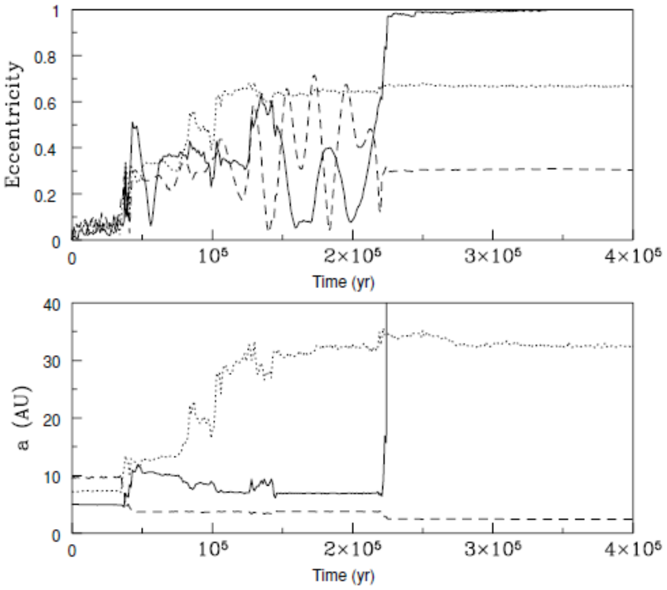

Figure 43: Typical evolution of the semimajor axis (top panel) and eccentricity (bottom panel) of a system of three jovian-mass planets (Marzari and Weidenschilling, 2002).

orbits, and when there are two planets left. However the stability criterion was derived only for single planets in coplanar orbits, and the long–term stability may be strongly different in those systems.

9

HYPERBOLIC PASSAGES

9.1 INTRODUCTION

It is widely believed that most stars form in embedded clusters on a timescale of about 1 Myr (Hillenbrand, 1997; Palla and Stahler, 2000). About 80% of stars within 1 kiloparsec of the Sun are actually found in clusters with a population exceeding 100 members (Porras et al., 2003). During the early stages of cluster evolution, stellar encounters are believed to significantly affect the formation and subsequent dynamical evolution of planetary systems around stars belonging to the structure. According to Malmberg et al. (2007, 2011), Malmberg and Davies (2009), and Zakamska and Tremaine (2004), scattering interactions with other stars in their birth cluster may excite the eccentricity and inclination of planets populating the outer parts of the system. This dynamical mechanism might contribute to explaining why eccentric orbits occur frequently in extrasolar planetary systems. In the case of multiple-planet systems, the eccentricity perturbations due to a stellar flyby can leave the planetary system in an unstable state. On timescales ranging from a few million to billion years an unstable planetary system may undergo a phase of planet–planet scattering leading to the ejection of one or more planets from the system (Weidenschilling and Marzari, 1996; Rasio and Ford, 1996). Furthermore, a stellar flyby might contribute to the excitation of the planet inclination, which is frequently observed (Triaud et al., 2010).

Stellar flybys are more frequent and statistically close in the early stages of a cluster evolution when the structure is more compact. When, after a few crossing times (Allen et al., 2007), a cluster loses its gaseous component, a substantial amount of unbinding occurs (Adams, 2000) and it disperses. The gas removal occurs within about 3–5 Myr from the formation of the cluster and, according to Allen et al. (2007), Fall et al. (2009), Chandar et al. (2010), and Dukes and Krumholz (2012), after about 10 Myr, 90% of stars born in clusters have dispersed into the field. We then expect that most of the close stellar encounters causing significant changes to the orbital elements of the planets occur when the planets are still embedded in circumstellar disks. Even if gas disk lifetimes are not well constrained observationally, they are assumed to be comparable to the cluster bound phase being in the range 3–6 Myr, as suggested by Haisch et al. (2001), or even longer, up to 10–12 Myr, as recently argued by Bell et al. (2013). It is then reasonable to assume that, statistically, most of the close stellar passages occur when the planets are still embedded in disks. The effects of stellar encounters must be modeled by considering the system planet+disk rather than isolated planets.

In effect, most numerical modeling of the effects of stellar encounters on planetary systems in clusters are based on pure N–body simulations where the effects of circumstellar disks are neglected (Malmberg et al., 2007; Malmberg and Davies, 2009; Malmberg et al., 2011; Zakamska and Tremaine, 2004). However, as suggested by the near coincidence between the cluster lifetime and that of circumstellar disks, this assumption may not be fully justified. Close stellar flybys are frequent in the initial stages of cluster evolution when the disks are still interacting with the embedded planets. We concentrate here on the effects of close stellar encounters on planets still embedded in their birth disk. Fragner and Nelson (2009) have shown that stellar flybys significantly altering the orbital parameters of planets are also expected to affect the disk structure. Via hydrodynamical simulations they find that stellar encounters with distances less than three times the disk radius r_d can cause a significant shrinkage of the disk. They concentrated on the effects of the modification of the disk structure on planet growth and migration suggesting that giant planets in systems involved in stellar encounters during their early evolution should have higher masses and larger semimajor axes. Our goal is to test whether the tidal interaction of the planet(s) with the disk, even truncated after the encounter, is able to damp the planet eccentricity and inclination excited after the flyby. The damping might also prevent the onset of gravitational instability in multi–planet systems at later times. For this reason we resort to hydrodynamical modeling to simultaneously compute the disk and planet evolution during and after the stellar flyby. We consider an evolved disk with a density significantly lower than the Minimum Mass Solar Nebula since planet growth is supposed to have already occurred.

We adopt two different approaches to assess this test case. First, we use a hydrodynamical 2D grid code to evalute the eccentricity excitation only, considering both a single planet system and a multiplanet one. Then, we study the test case with a full 3D SPH code, to take account also of the inclination evolution. Furthermore, in this second case we consider also the disks interaction, modeling a disk around each star.

9.2 THE 2–D CASE

9.2.1 *The numerical model*

We used the numerical code FARGO (Masset, 2000) to model the time evolution of a planet embedded in a two-dimensional circumstellar disk surrounding a solar type star ($M = 1 M_\odot$).

The reliability of FARGO, without additional special numerical resolution requirements, has been recently confirmed by Kley et al. (2012). The code solves the hydrodynamical equations on a polar grid, and it uses an upwind transport scheme along with a harmonic, second-order slope limiter (van Leer, 1977).

We focused on evolved disks since we assumed that planets have already formed or are in their final growth stage. At this stage, along with viscous diffusion, the disk is also dispersed by photo–evaporation produced by photons emitted by the central star and, possibly, by nearby stars. For this reason we adopt a low initial disk's surface density which allowed us to neglect the effects of disk self-gravity. For the same reason we can work under the assumption that the disk is locally isothermal so that the temperature only depends on r and H/r is a constant. The initial density profile is $\Sigma = \Sigma_0 r^{-1/2}$ where Σ_0 is the 2D density at 1 AU from the star and was set to $100 g/cm^2$, a value significantly lower than that of the Minimum Mass Solar Nebula, which is at least ten times higher, while for the aspect ratio H/r we chose 0.05. A constant shear kinematic viscosity, $\nu = 10^{-5}$ in code units (mass unit is $1 M_\odot$, G is equal to 1, while the length unit is set to 1 AU), is adopted in all simulations. The disk ranges initially from 0.5 to 30 AU, and the density is smoothly reduced to a floor value of 1×10^{-9} (in code units) beyond 30 AU. The computational domain extends to 50 AU and is discretized in 864×240 grid zones, in r and θ. An outflow boundary condition is adopted at both the grid's inner and outer edges. No mass can flow back into the system once it has escaped. The secondary star ($M = 1 M_\odot$) is started on a hyperbolic orbit having a minimum impact paramater q fixed at the beginning of the simulation, larger than the outer border of the grid. It is initially located at a distance of 800 AU from the star with the planetary system and the relative velocity at infinity is set to 1 km/s, a typical value in clusters.

One or more planets are considered and their orbits are affected by the disk, the mutual gravitational attraction if more than one planet is present, the gravitational force of the central star, and that of the passing star. To properly model the strong gravitational interactions between the passing star and the planets, the numerical integrator computing the planet orbits (a 5th order Runge Kutta in FARGO) has been updated with a variable stepsize. The orbital changes of the planet orbit caused by the stellar flyby significantly depend on the approach configuration. In Fig. 44 we show the outcome of pure 3–body numerical integrations (the disk is neglected) showing the eccentricity evolution of the planet for different initial values of its mean anomaly M sampled from 0° to 360° with a constant interval of 30° (the second star trajectory is kept fixed). Since the initial orbit of the planet is circular, this is the only relevant angle in determing the relative position of stars and planet when the flyby occurs. The jump in eccen-

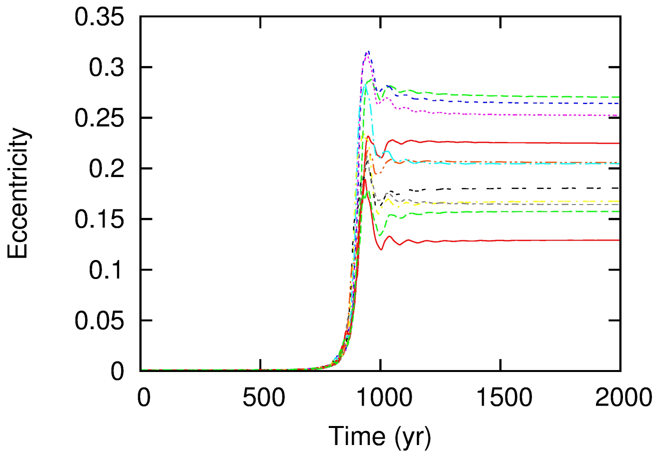

Figure 44: Evolution of the eccentricity of a Jupiter size planet during and after a close stellar encounter in a pure 3–body problem (no disk). The initial mean anomaly M of the planet is sampled with a step of 30° starting from 0°. The eccentricity step Δe depends on the initial value of M which changes the geometrical configuration of the 3 bodies at the stellar encounter.

tricity Δe due to the stellar flyby perturbations significantly depends on M and ranges approximately from about 0.13 to 0.27. Since our goal is to show that the disk is able to damp the eccentricity pumped up during stellar encounters, in our full model stars-planet-disk we always look for initial conditions leading to the largest Δe. However, the outcome shown in Fig. 44 give us only an indication of the eccentricity variation but cannot guide us in looking for the initial value of M to set in the input file of FARGO to get the maximum Δe. This because the evolution of the planet embedded in the disk is different from a pure 3–body problem. The interaction with the disk causes migration in the time interval from the beginning of the simulation and the occurrence of the stellar encounter and this leads to a different geometrical configuration at the encounter. For this reason, in each model we perform four test runs where we sample the initial value of M of the planet and we continue the model with the largest Δe, the most perturbing configuration. We cannot perform an accurate sampling, like the one shown in Fig. 44, using the complete model that includes the stars, the planet(s) and the disk since it would be too much time consuming.

The FARGO code is two-dimensional (2D), so our modeling covers those cases where the trajectory of the incoming star is not very inclined with respect to the planet's orbit.

9.2.2 *Case A: a single planet orbiting at 18 AU from the star*

We first consider a planet with a mass equal to $M_p = 30M_\oplus$, a super–Earth or the core of a giant planet, initially on a circular orbit ($e = 0$) around the star with semimajor axis $a = 18AU$. Such a large semi-major axis is adopted to cover the extreme cases where the planet is located close to the outer border of the disk after the stellar flyby and might be less affected by the disk force. When the planet is fully embedded in the disk, it is expected that the damping is faster and efficient. The minimum approach distance during the stellar encounter q is set to 70 AU. This is a close encounter configuration that has strong effects on both the disk and planet orbit. In fact, when the passing star approaches the system, a significant amount of mass is stripped away from the disk. At the same time, the orbital elements of the planet are changed on a short timescale. A sudden jump occurs in both eccentricity and semimajor axis, as predicted by Malmberg et al. (2007); Malmberg and Davies (2009); Malmberg et al. (2011), and Zakamska and Tremaine (2004).

In Fig. 45 we show the evolution of the disk during the stellar flyby. More than half of the initial mass $M_{d0} = 0.008M_\odot$ is lost, and the disk is left with $M_d = 0.003M_\odot$. Just after the encounter the disk is shrunk to about 12 AU, and it relaxes to 14 AU with time (assuming that its border is marked by a density of $10^{-5.5}$, which is the lowest density of the disk at the truncation radius and before the stellar encounter). The elliptical internal low–density region around the central star has been observed in a number of previous numerical studies of isothermal disks in binaries (Kley et al., 2008; Marzari et al., 2009, 2012). It is related to the formation of strong spiral density waves that propagate all over the disk and cause a flow of mass through the inner border of the disk down to the star surface. It disappears at later times due to the continuing viscous evolution of the disk.

In spite of the strong mass depletion, the disk is still able to interact with the planet and circularize its orbit. This behavior is illustrated in Fig. 46. The planet eccentricity is excited to about 0.2 and the semi-major axis jumps down to 17.5 AU during the interaction with the passing star. However, the subsequent interactions between the disk and the planet damps the eccentricity on a short timescale (less than 10^4 yr) and, at the same time, the planet resumes its type I migration inwards. It is clear from this example that, if excited by stellar encounters, planets on inner orbits will return to circular orbits on an even shorter timescale since the gas density increases closer to the star.

A second simulation was performed with a Jupiter size planet $M_p = 1M_J$ and with the same configuration for the disk and the passing star. To make the model more precise, we should have run the code without the passing star and with the planet on a fixed orbit to give it the time to carve a gap in the disk at its location prior to the stellar flyby. However, as also shown by Fragner and Nelson (2009), a close stellar encounter strongly perturbs the disk, destroying any previous structure present in it. A pre-existing planetary gap would be fully erased by the tidal perturbations of the passing star.

As in the case of the light planet, after the initial step due to the passing star perturbations, the eccentricity of the Jupiter–size planet is damped on a short timescale as shown in Fig. 47. Just after the stellar encounter, the planet is left on an eccentric orbit and without a gap. It has a fast inward migration that halts when its eccentricity is damped to almost zero. At that time, it has carved a new gap around its orbit and it resumes its regular type II migration. Even in this case the stellar encounter does not leave the system with a planet on an eccentric orbit, but it eventually causes a period of rapid inward migration after destroying the gap that the planet developed prior the encounter. But, after about 10^4 yr, the system has absorbed most, if not all, the perturbing effects of the stellar encounter. The disk may still bear some eccentricity, but the viscous evolution will bring it back to a circular state. When this happens, the system will have erased all records of the close stellar passage.

9.2.3 *Case B: three planets orbiting the star*

Stellar encounters are important for multiplanet systems since they could trigger a phase of dynamical instability followed by the ejection of one or more planets and significant changes in the orbital architecture. If the eccentricity of the outer planet is excited by a passing star, Hill's stability might be destroyed, leading to a phase of planet–planet scattering at later times (Malmberg et al., 2007; Malmberg and Davies, 2009; Malmberg et al., 2011; Zakamska and Tremaine, 2004). A high eccentricity is actually the first step in developing of a chaotic behavior.

We explore here the case of a system made of three Jupiter size planets embedded in an evolved disk and migrating towards the star. We preferred a 3–planet system rather than a 2–planet one for its higher dynamical complexity and stronger tendency to develop crossing orbits (Chatterjee et al., 2008). Marzari et al. (2010) have already studied a system of three giant planets embedded in a circumstellar disk, and they show that the migration leads the planets into different evolutionary paths, either mutual resonance trapping or planet–planet scattering. The choice between the two dynamical paths depends on the masses of the planets and on the disk physical properties. In this paper we investigate whether the stellar flyby is always leading to planet–planet scattering with final eccentric orbits that can be observed or if, again, the influence of the disk is able to damp the eccentricity of the planets and erase any memory of the chaotic phase.

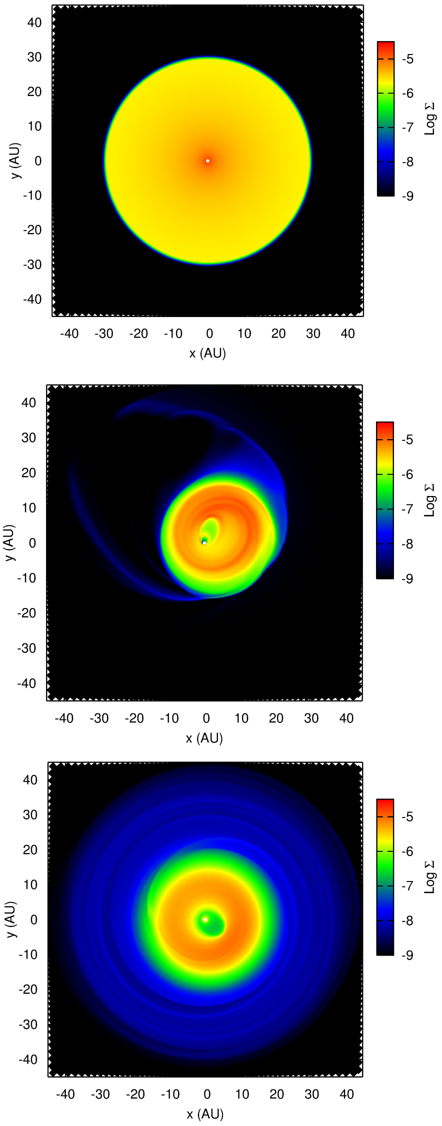

Figure 45: In panels 1,2,3 we show the contours of the gas density (in normalized units) when the passing star is at 800 AU before the pericenter passage, 150 AU and 10000 AU after the pericenter, respectively.

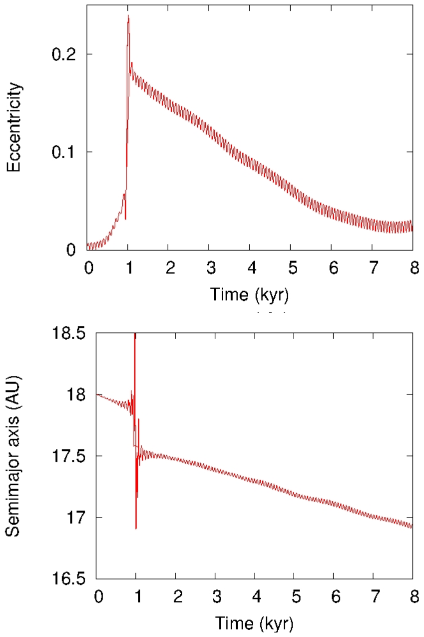

Figure 46: Evolution of the eccentricity and semimajor axis of a light planet ($M_p = 30M_\oplus$) in a circumstellar disk during and after a close stellar encounter. The eccentricity is damped on a short timescale and normal migration is resumed.

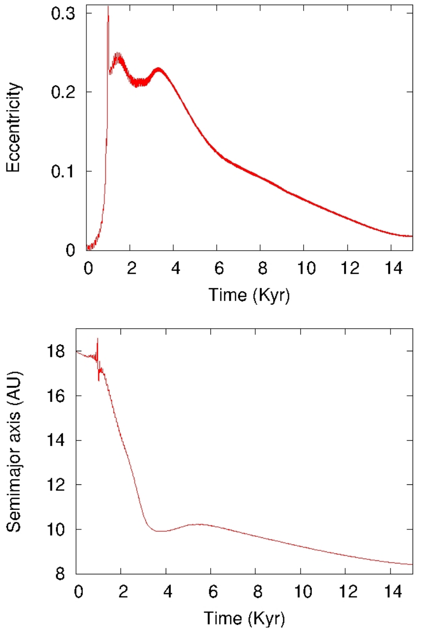

Figure 47: Same as in Fig. 46 but for a more massive planet ($M_p = 1M_j$). Even in this case the eccentricity is damped and type II migration resumed.

In Fig. 48 we illustrate the evolution of a 3–planet system with the planets initially on circular orbits with semimajor axis 5,10,18 AU, respectively. The eccentricity of all planets are excited during the stellar encounter. The outer planet shows a sudden step when the passing star reaches the pericenter, and the other two planets are strongly perturbed, at subsequent times, both by the eccentricity of the outer planet and by the strong eccentricity developed by the disk. The inner planet is the most affected by the turmoil of the stellar encounter, and its eccentricity is slowly pumped up to almost 0.4. However, the disk is slowly circularized and the subsequent disk–planet interactions damp the eccentricities of all the planets. After about 10^4 yr, the system has completely erased the effects of the stellar encounter, and all the three planets migrate towards the star at a slow rate trapped in a mutual 2:1 resonant configuration. Their further evolution would be no different from what is observed in a single star that has not undergone a stellar encounter even if a longer integration would be needed to figure out if the resonant capture is stable or not. However, this is beyond the scope of this paper which focuses on showing that the disk is able to erase the effects of stellar encounters. A second more compact system was modeled where the planets are closer to each other. The inner one has a semimajor axis of 4 AU, the middle one of 8 AU, and the outer of 12 AU. The stellar hyperbolic trajectory is kept the same. Even in this case we observe a consistent eccentricity excitation for all three planets. In Fig. 49 we show the orbital element evolution of the system before and after the close stellar passage. A close

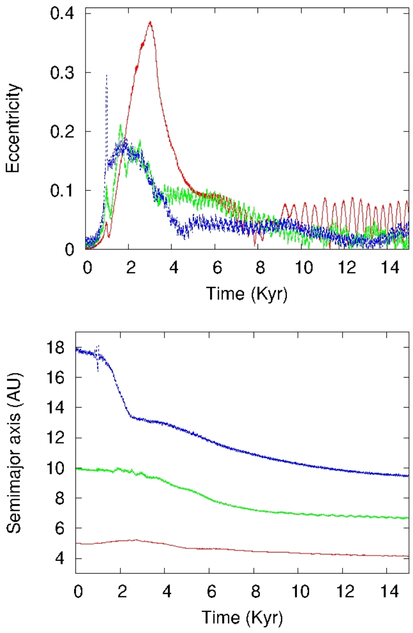

Figure 48: Evolution of a 3–planet system ($M_{p1} = M_{p2} = M_{p3} = 1M_j$) during and after the stellar encounter. Even in this case the eccentricity is damped in less than 10 Kyr.

encounter occurs between the two outer planets, but even in this case on the long term the disk damping takes over, and the eccentricity is slowly reduced after about 10 Kyr from the stellar encounter. The system returns to a quiet evolution with the planetary eccentricities reduced to pre–encounter values with an additional forced component due to the mutual secular perturbations. The planets keep migrating inside within a common gap as shown in Fig. 50. The two inner planets are trapped in a 2:1 resonance, while the outermost planet is drifting at almost the same speed as the resonant pair. This does not mean that the stellar encounter did not affect the evolution of the system since the semimajor axes possibly evolved faster during the period of high eccentricity. However, at the end of the excited period, the eccentricities are damped, and simply by looking at the values of the semimajor axes, it is not possible to guess the occurrence of the stellar encounter. This same behavior was observed in other simulations where the initial orbital elements had different initial orbital angles. As shown in Marzari et al. (2010), a wide variety of outcomes are possible after the chaotic scattering phase ranging from orbital exchange, planet merging, and scattering of a planet in a hyperbolic orbit. Of course in 2D models like those shown in Marzari et al. (2010) and presented here, the probability of planet merging is significantly increased over a more realistic 3D model, since the 2D cross section for impact is significantly larger than for the 3D one. However, this is a possibility that needs to be taken into account. In the case of three

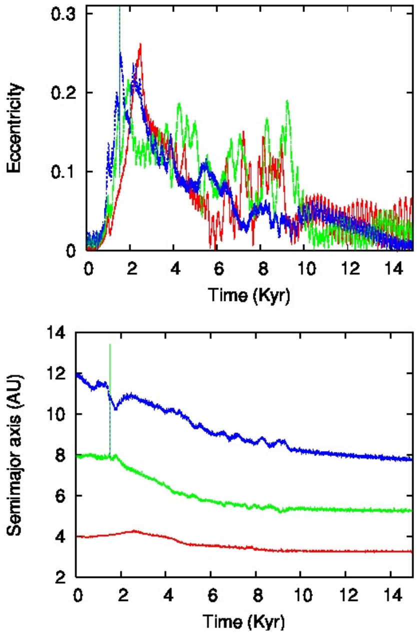

Figure 49: Same as in Fig. 48 but for a system initially mode compact ($a_1$4 AU, $a_2 = 8$ AU and $a_3 = 12$ AU). The eccentricity is damped and only the forced component due to mutual gravitational interactions between the planets is left.

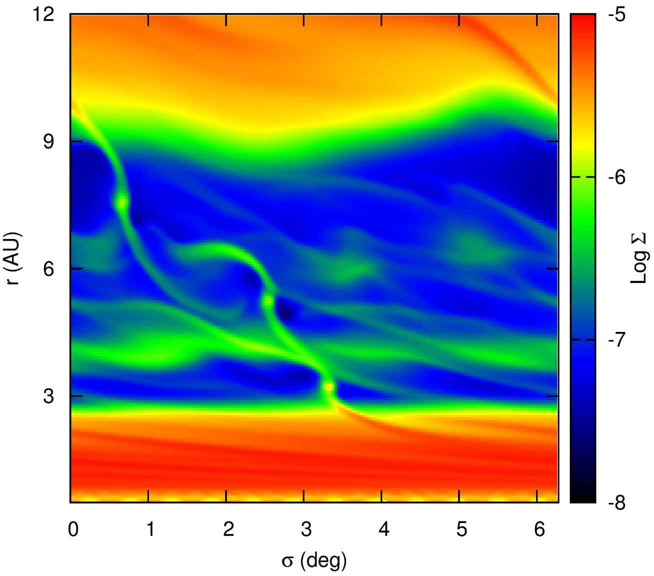

Figure 50: Disk density distribution in cylindrical coordinates after the stellar flyby. The three planets are migrating inside, and they have carved a partial gap. The two inner planets are in a 2:1 mean motion resonance.

planet systems perturbed by a stellar flyby we expect that the statistical distribution of all possible outcomes is different from the unperturbed case. In particular, the occurrence of planet–planet scattering as shown in Fig. 49 may occur more frequently than the unperturbed case due to the large perturbations in the planet orbits induced by the stellar encounter. However, a deep exploration of the parameter space is required and this appears to be a really complicated task due to the large number of free parameters, such as the masses of the planets, their initial orbits, and the disk parameters. Undertaking this task would bring out the real influence of stellar flybys on the planet architecture of systems embedded in clusters, not in terms of eccentricity excitation but in the semimajor axis and mass distribution of the planets. Unfortunately, the required amount of CPU time even for a 2D statistical exploration appears out of reach for the moment.

9.2.4 *Resolution*

To validate our results and demonstrate that the damping of eccentricity after a stellar flyby is a robust result and that it does not depend on the grid resolution used in FARGO, we performed two additional simulations for the case of a single massive planet shown in Fig. 47, which represents our standard model. The first is a lower resolution run with a grid size of 432x120, while the second is a high–resolution run with a 1152x320 grid. The outcome of these two additional models are shown in Fig. 51, where they are compared to the standard resolution model. The three runs confirm that the eccentricity damping occurs independently of the resolution used in the code. However, there are differences in the eccentricity evolution, which are mostly related to the configuration of the planet at the stellar encounter. As shown in Fig. 44, the eccentricity jump depends on the position of the planet in its orbit, i.e. on its mean anomaly M, when the stellar passes close to the planet. If a different resolution is used, prior to the stellar encounter the evolution of the semimajor axis due to the interaction with the disk will be slightly different, and the value of M at the stellar encounter will differ in the three runs. This leads to an avalanche effect that affects the peak eccentricity at the stellar flyby, the subsequent planet migration and the damping rate. However, Fig. 51 confirms that erasing the stellar flyby effects is a robust effect, and the resolution does not alter the morphology of the long–term evolution of the system, which tends towards the circularization of the planet orbit.

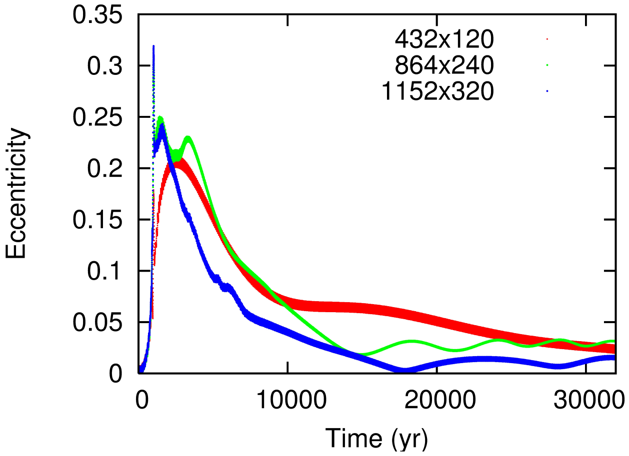

Figure 51: Eccentricity evolution of a single massive planet for 3 different grid resolutions: 432x120, 864x240 and 1152x320, respectively. The parameters are the same as used in the model shown in Fig. 47.

9.3 THE 3–D CASE

9.3.1 *The numerical model*

The hydrodynamical code used to model the evolution of the disks surrounding both stars is VINE (Wetzstein et al., 2009; Nelson et al., 2009). It is based on the smoothed particle hydrodynamics (SPH) algorithm, which solves the hydrodynamical equations by replacing the fluid with a set of particles (Gingold and Monaghan, 1977). The code has been updated to improve momentum and energy conservation as described in Appendix A. Variable smoothing and softening lengths have been introduced as in Price and Monaghan (2004), Springel and Hernquist (2002) and Price and Monaghan (2007). To realistically model the gas accretion onto the planet, we implemented the algorithm described in Ayliffe and Bate (2009). The planet potential is modified adding a "surface" potential term in the following way:

$$F_r = -\frac{GM_p}{r^2}\left[1-\left(\frac{2R_p-r}{R_p}\right)^4\right] \tag{153}$$

for $r < 2R_p$. M_p and R_p are the initial mass and radius of the planet, respectively. When an SPH particle reaches the surface of the planet (R_p) the net force is 0, whereas if r becomes smaller than R_p, the potential becomes strongly repulsive and the particle is driven back to the planet surface.

The disk around each star has an initial density at 1 AU of $\rho_0 \sim 1 \times 10^{-11}$ g/cm^3, approximately 1/100 of the Minimum Mass Solar Nebula. Its radius extends out to 40 AU with a density profile declining as $\rho(r) = \rho_0 r^{-3/2}$, corresponding to a superficial density decreasing as $\Sigma = \Sigma_0 r^{-1/2}$. The total mass of each disk is 7×10^{-3} $M_\odot$, about 14 times less massive than the disks modeled in Forgan and Rice (2009). The reason of such a low density is justified by the presence of a fully formed giant planet in the disk. In our scenario, core–accretion and gas infall already occurred and most of the gas is expected to have been either accreted by the star because of viscous evolution or dispersed by photo–evaporation. In addition, if eccentricity and inclination damping occurs in light disks, it would be even more efficient in massive disks. In modeling these light disks we can neglect the effects of self–gravity and adopt the isothermal approximation since they are optically thin. The disk scale height H is set to 0.05 giving a temperature T_0 at 1 AU from the star of about 620 K. Since during the stellar encounter the disks may become warped, the isothermal temperature profile is always computed respect to the average median plane of the disk. Each disk is simulated with 850000 SPH particles for a total of 1.7 million particles for the whole system.

We adopted the standard SPH artificial viscosity (Monaghan and Gingold, 1983), introducing a linear (α_{SPH}) and a quadratic (β_{SPH}) term whose initial values are set to 0.1 and 0.2, respectively. Meru and Bate (2012) showed that these terms can be compared to the Shakura and Sunyaev (1973) α–viscosity parameter α_{SS} defined as $\nu = \alpha_{SS} c_s H$ where ν is the kinematic viscosity, c_s is the sound speed and H is the vertical pressure scale height. Using their relations we find that, away from the close approach, the corresponding α_{SS} in our models is about 0.002.

One disk harbors a Jupiter size planet orbiting at 18 AU on a circular orbit not inclined respect to the disk. We set the planet on an outside trajectory since we want to maximize the effects of the stellar encounter in order to test if, in spite of the highly perturbing configuration, the disk is still able to damp the planet eccentricity and inclination after the flyby. The second star is started on a hyperbolic orbit with a minimum impact parameter q fixed at the beginning of the simulation. The initial distance between the two stars is 450 AU (approximately 500 yr before the encounter) and the relative velocity at infinity is set to 1 km/s, a typical value in clusters. Different inclinations are considered for the passing star to test the amount of disk warping and planet excitation in inclination. The two disks are oriented at different angles up to the extreme case of prograde-retrograde encountering disks where one is rotating in the direction of the encounter orbit, and the other against it.

Prior to the encounter, the planet begins to carve a gap. We might have let the disk–planet system to evolve longer in order to allow the planet to create a full gap. However, as also shown in Fragner and Nelson (2009) and in the previous 2D model, a close stellar encounter strongly perturbs the disk and planetary orbit, cancelling out any pre-existing structure including a gap around the planet. A new gap is created some time after the stellar flyby when the disk relaxes, as shown in our simulations.

9.3.2 *Definition of the different flyby geometry and disk inclinations*

Due to the large amount of CPU time required by each 3D run, we have performed a limited number of simulations covering, by necessity, a small but meaningful portion of the initial phase space. We look for the most perturbed configurations since our goal is to test the ability of the gaseous disk to damp the planet orbital parameters after the stellar encounter even in extreme conditions. In Tab. 7 we summarize the main initial parameters of each simulation (first 5 columns of the table) while the changes of some relevant disk properties, during the evolution of the system, are given in the other columns. Their meaning will be described later on.

To compute the initial set up for the disks and the hyperbolic encounter, we start from a coplanar configuration where the hyperbolic trajectory of the second star has the pericenter on the positive x–axis while the star harbouring the planet is at the origin of the x–y frame. We then tilt the hyperbolic orbit around the x–axis by an angle i_{s2} to vary the approach geometry. We also rotate the disk of the second star around the y–axis by an angle i_{d2}. The disk of the primary star has instead its median plane on the x–y plane. We could have further varied the initial configuration by rotating both the disks around the x and z–axis, but due to the heavy CPU load of each simulation, we considered only the rotations defined by i_{s2} and i_{d2}.

In Fig. 52a we show an example of this procedure giving a full 3D view of the encounter geometry for the case h where the disk is inclined of 60° respect to the primary disk and the hyperbolic trajectory is inclined of 30^o respect to the primary disk plane. The hyperbolic trajectory is shown during the pericenter passage and the two disks are plotted at 3 different evolutionary times. A 2D projection in the (x,z) plane (Fig. 52b) of the previous plot gives an additional view of the mutual orientations of stars and disks.

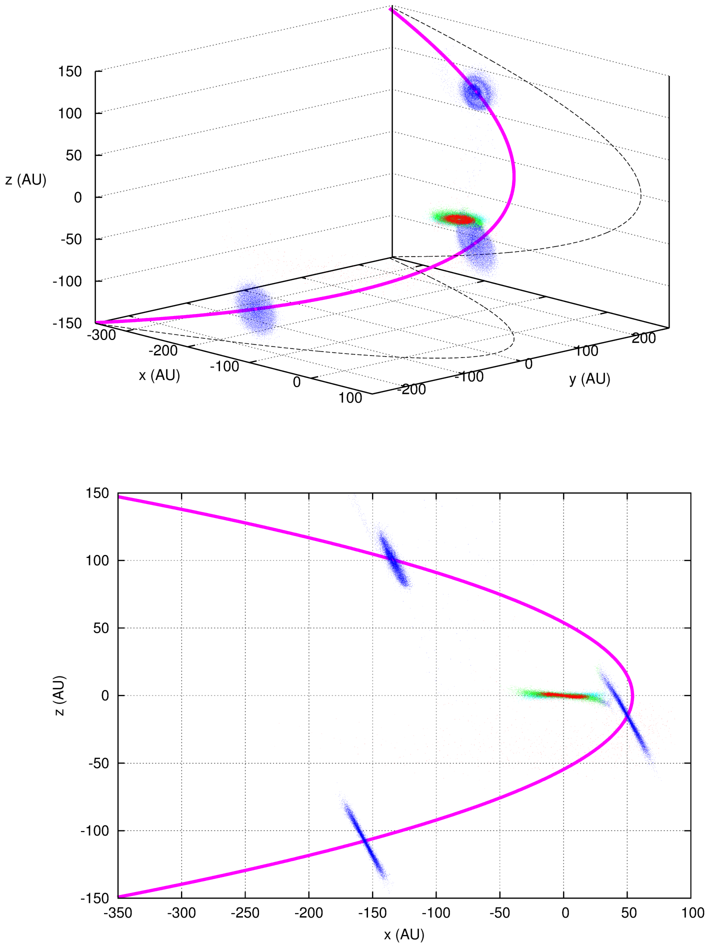

Figure 52: In the top panel we illustrate in 3D the encounter geometry of model h. The hyperbolic trajectory is plotted as a continuous line while its projections on the (x,y) and (x,z) plane are shown as dashed lines. The disks around the primary and secondary star are shown at 3 different evolutionary times around the pericenter passage. The primary disk is at the center of the reference frame so its shape overlaps at the 3 different times. In the bottom panel we show a projection of the 3D plot on the (x,z) plane, a view that helps to understand the dynamical configuration of the encounter.

In a test case we also changed the minimum approach distance q (case b) and we also performed a simulation with no disk around the second star to compare with all other cases with two disks (case d).

This model is relevant for understanding the role of the disk around the second star in the evolution of the planet.

9.3.3 *Cases* a, b *and* c*:* $i_{d2} = 45^o$.

We first analyze the models where the disks are mutually inclined of 45^o i.e. $i_{d2} = 45^o$. In two cases with this configuration we test the dependence on the periapse distance q of the hyperbolic orbit on the evolution of the disks and planet orbit (cases a and b). In the third case c we incline also the hyperbolic trajectory setting $i_{s2} = 60^o$. This last case is more general in terms of geometric configuration and we will adopt it as reference case comparing its outcome to the other two. In Fig. 53 the evolution of the disks and planet are shown at different times for case c. At the minimum distance (first two plots) the disks begin to interact becoming highly eccentric and strongly warped. The outer edge of the disk around the passing star overlaps close to the center with that of the primary star. At subsequent times, the disks are very distorted, and tidal tails are launched causing a significant mass exchange. It is noteworthy that in the third plot the disk around the passing star (secondary star) appears very eccentric, but this is a perspective effect. When the integrated density is computed, the inclined disk is projected on the x–y plane and so it appears more eccentric due to its inclination. About 2800 yr after the flyby, the primary disk is returned to a quiet state and the planet has carved a new gap in the disk, as illustrated in Fig. 54.

9.3.3.1 *Evolution of the planet orbit*

The planet in case c, which appears in the plots of Fig. 53 and Fig. 54 as a local overdensity, is moved on an inclined and eccentric orbit after the stellar flyby due to the gravitational pull of the passing star. However, the subsequent interaction with the disk damps both the eccentricity and inclination and, on a short timescale, the planet is driven back on an almost circular orbit not inclined respect to the disk plane. All the effects of the stellar flyby have been erased apart from a shift in semimajor axis. However, the final planet orbit may be slightly inclined respect to the equatorial plane of the primary star since the disk, after a warped phase, relaxes into an inclined configuration (see Fig. 54, bottom plot). The planet, tidally interacting with the disk, is dragged back not to the star equatorial plane but to the disk median plane, slightly tilted, after the flyby, respect to the star equatorial plane.

In Fig. 55 we show the time evolution of the orbital parameters of the planet in the 3 simulations a, b, and c. The semimajor axis, after a jump caused by the stellar encounter, decreases with time due to the tidal interaction with the disk. A new gap around its orbit is forming, as shown in Fig. 54 (top plot) for the case c ($i_{d2} = 45^o$ and $i_{s2} = 60^o$),

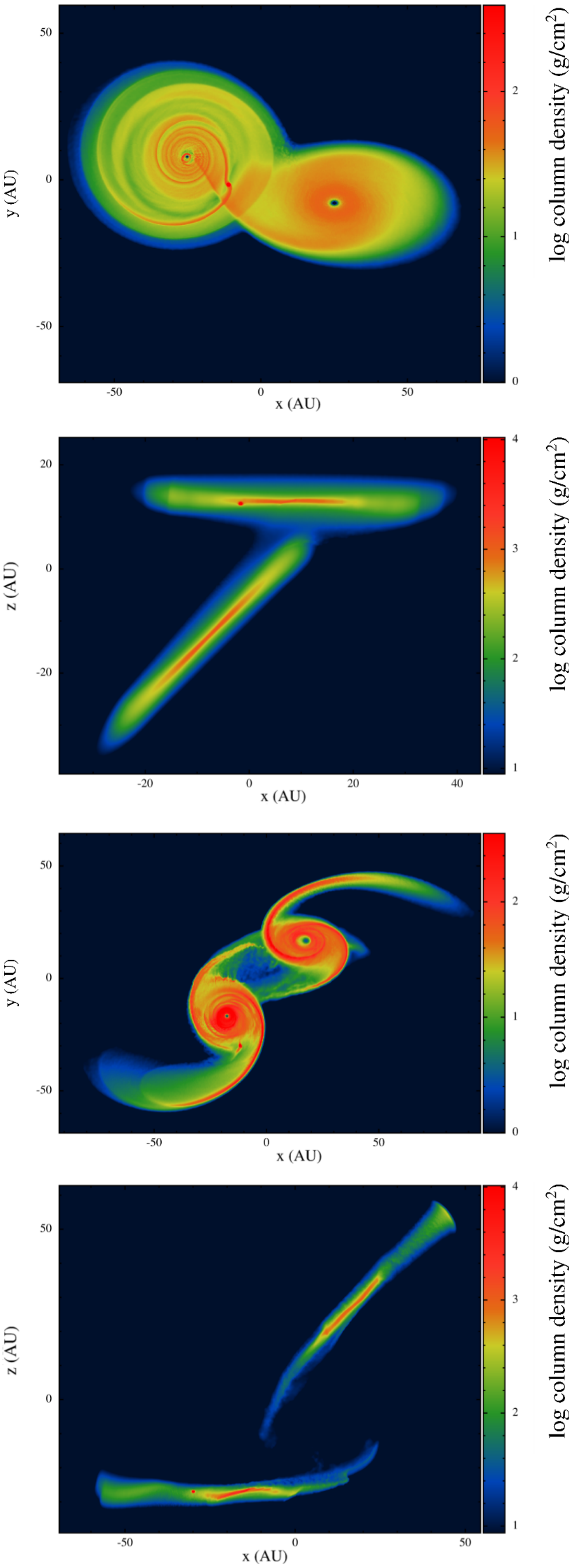

Figure 53: Logarithm of the superficial density (column integrated) of the circumstellar disks in the x–y and x–z plane, at 2 different evolutionary steps during the stellar flyby for the model c. Note that the color scale for the superficial density Σ is different in the x–y (face–on) and x–z (edge–on) projections since the bulk density ρ is integrated along different paths. The top plots show the disks when the stars are close to the pericenter passage, the bottom plots when the stars are departing just 60 yrs after the encounter.

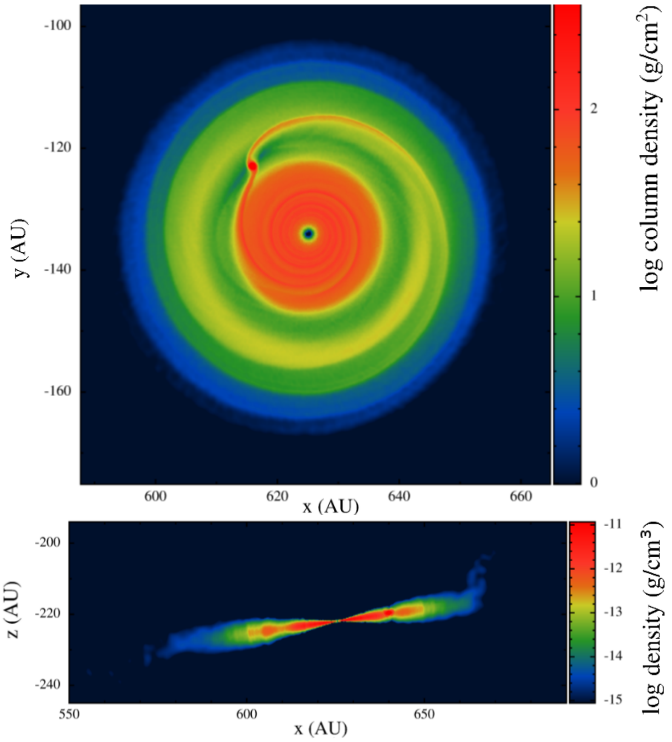

Figure 54: Logarithm of the superficial density (column integrated) of the disk around the star with planet and its x–z slice 2800 yrs after the flyby for the model c. The disk has reached a quiet state and the planet has almost completely carved a gap around its orbit.

but it is not yet deep enough to cause the slow type I migration which will probably start at later times. The delay is also due to the initially inclined orbit of the planet respect to the disk which slows down the gap carving.

The eccentricity pumped up by the stellar flyby is quickly damped when the second star departs from the primary after the encounter. This is illustrated in Fig. 55 middle panel. In the most perturbed configuration (case a) the eccentricity grows up to 0.5 and is quickly reduced to 0.2 in less than 1000 yr. After this initial phase, the damping is slower occurring at a rate of about 6×10^{-6} yr^{-1} leading to a full damping on a timescale, in the worst case, of a few 10^4 yr. In cases b and c the initial eccentricity excitation is of the same order of magnitude. The inclination of the hyperbolic orbit of case c possibly reduces the strength of the passing star perturbations on the planet eccentricity as it does the larger flyby minimum distance in case b. However, the damping appears to be faster in case c where the final eccentricity, after 2700 yr from the flyby, is only 0.02.

In case c the inclination of the planet respect to the equatorial plane of its host star is excited during the flyby up to about 4.5°. After the stellar encounter also the disk is inclined respect to its initial plane and its inclination is about 8.5° as shown in Fig. 56, top plot. The gravitational interaction between the planet and disk drives the planet back into the disk and its inclination is slowly brought to the same value of that of the disk. The mutual inclination between the planet and the disk decreases smoothly with time to a low value of about 1° when the simulation was stopped after 2.3 kyr. In Fig. 56, bottom plot, we show the evolution of the disk and planet inclinations in the case a. The orbit of the planet is not excited in inclination by the stellar flyby since $i_{s2} = 0$. However, the disk around the primary star is first warped and then it settles down to an inclination of about 2.8°. The planet inclination grows until the mutual inclination between planet and disk is negligible.

The outcome of these models confirms that the presence of the disk leads to a fast damping of the eccentricity and inclination due to the stellar flyby, erasing any trace of the event in the trajectory of the planet. Such an event might be recorded in the inclination of the disk (and then of the planet) respect to the equatorial plane of the star but the expected tilting would be very small. It could accelerate the inward migration of the planet by restarting type I migration after the stellar flyby when the gap is erased but soon a new gap would be cleared and type II migration restored.

9.3.4 *Coplanar cases* d, e, *and* f

These models assume a coplanar initial configuration for the disks and for the hyperbolic orbit of the passing star, i.e. $i_{d2} = 0^\circ$ and

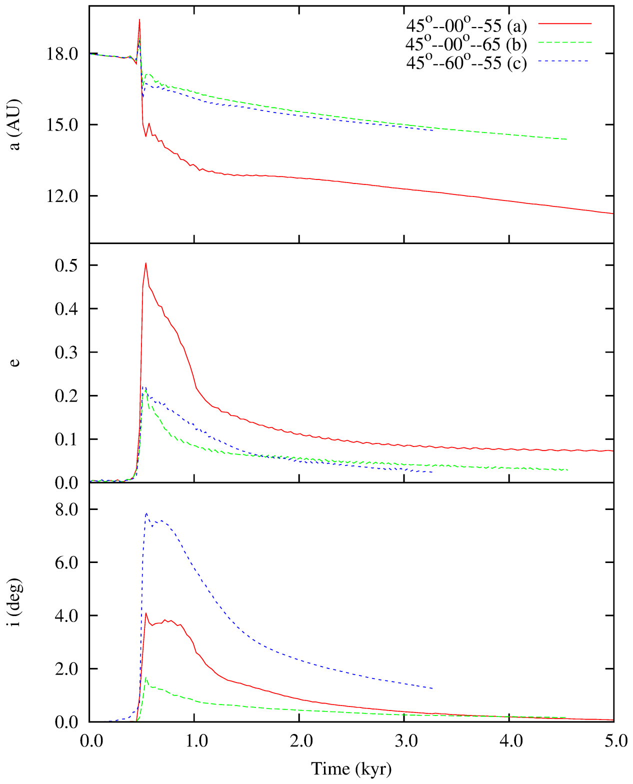

Figure 55: Evolution of the semimajor axis (top panel), eccentricity (middle panel), and inclination (bottom panel) of the planet in models a,b, and c.

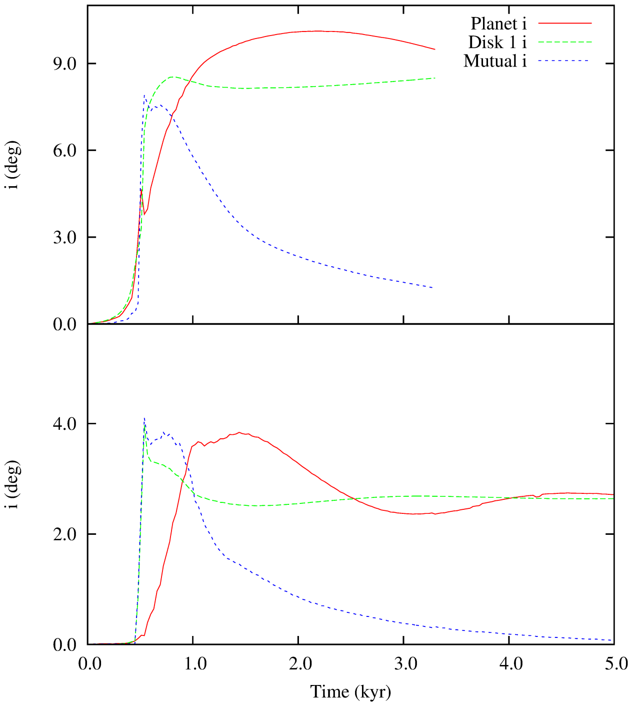

Figure 56: Evolution of the disk, planet and mutual inclination for cases c, top panel, and a, bottom panel.

$i_{s2} = 0^\circ$. They are the analogous of 2D models except that the disks are computed in 3D. We do not have changes in inclination and we concentrate only on the semimajor axis and eccentricity variations. As illustrated in Fig. 57, the eccentricity and semimajor axis jumps in the three cases d, e, and f are about the same. This confirms that the gravitational perturbations of the passing star dominates the dynamical evolution of the planet during the flyby. The subsequent damping is not significantly influenced by the different evolution and mass loss of the disk (see Tab. 7) but it is slightly faster compared to that of case a ($i_{d2} = 45^\circ$, $i_{s2} = 0^\circ$), shown as a reference in Fig. 57. This is possibly due to the disk–planet mutual inclination that, in case a, reduces the tidal interaction.

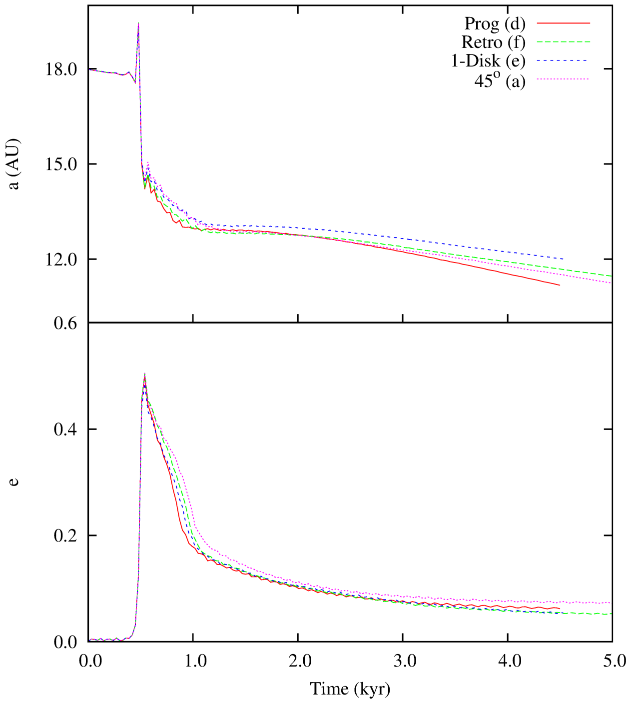

Figure 57: Evolution of planet's orbital elements a and e in models d, e, and f (coplanar cases), compared with the case a.

We considered the prograde-retrograde encountering configuration as an extreme case with one disk (that hosting the planet) rotating in the direction of the encounter orbit, and the other rotating against the encounter. The star is on a hyperbolic orbit coplanar to both disks. The evolution of the disks is not symmetric since for one disk (the primary) the secondary star is on a prograde trajectory while for the second disk the primary star is seen as moving on a retrograde trajectory. In Fig. 61 the disk integrated column density is shown shortly after the stellar flyby (top panel) and 60 years later (bottom panel). The two disks are not perturbed in a symmetric way, as for the coplanar prograde case, and only the primary shows a consistent mass loss along the trailing tidal wave. The disk around the secondary passing star does not become significantly elliptic and it does not develop tidal waves before the encounter. It appears to be less perturbed by the primary star gravity and this is in agreement with the findings of Hall et al. (1996) claiming that the angular momentum transfer between a perturber and a disk in a retrograde configuration is smaller. A similar effect was also observed in Forgan and Rice (2009) for more massive disks. At the pericenter of the flyby the two disks come in contact and mass is transferred from one to the other. As it can be noted in Fig. 61, the primary disk shows the usual spiral structure with the trailing arm extending into the secondary disk. Due to the direct interaction between the disks, the upper part of the secondary disk (retrograde respect to the primary star) is strongly distorted while the bottom part of the disk is almost circular and unperturbed. According to Tab. 7 the primary disk loses approximately $1/4$ of its mass while the secondary disk gains 2% of its initial mass.

In spite of the strong differences in the disk evolution between the prograde and retrograde cases, the orbital evolution of the planet is not significantly different. This reinforces the idea that the tidal damping of the planet eccentricity is a robust mechanism that does not depend significantly on the disk evolution. Once the perturbing effects of the star flyby are passed, and this occurs on a short timescale, the disk relaxes and drives the planet back to a circular non–inclined orbit.

9.3.4.1 *Mass exchanged by disks or lost to infinity*

A significant difference between our 2D and 3D models is the amount of mass lost by the disk with planet during the encounter. In 2D the primary disk retained about half of its initial mass at the end of the simulation while in the 3D cases here presented the fraction of mass loss, summarized for all models in Tab. 7, is significantly smaller and it strongly depends on the encounter geometry, as shown in Fig.59. This difference may be ascribed to the following reasons.

- In previous 2D models only one disk was included while in the present models we consider 2 disks. The presence of the disk around the secondary star has important consequences for the evolution of the system since a consistent fraction of the mass lost during the encounter by the disk around the primary is replaced by mass stripped from the disk of the secondary. According to Tab. 7 up to 13% of the disk initial mass can be exchanged between the two disks. Explicative in this context is the outcome of model e. In Fig.60 we show the density distribution after the stellar encounter illustrating how, during the stellar flyby, the second star, initially without its own disk, strips material from the primary. The new captured disk has a mass with mass equal to 15% of the initial disk mass of the primary (see Tab. 7). This proves that a large amount of mass can be transferred from one disk to the other, an effect not observed in the 2D model because the secondary star was out of the computational grid.

- In 3D the disk evolution, and then the mass loss, depends also on the behaviour along the vertical direction. This leads to a lower mass loss in 3D models respect to 2D ones as illustrated in Fig.58 where we compare the outcome of the 3D model e with a 2D simulation, performed with the SPH code, having the same initial physical parameters and profiles of model e. The mass loss is slightly higher in the 2D model just after the stellar flyby. However, the comparison also suggests that changing the dimensions of the simulations has less impact on the mass loss than the existence of a secondary disk. As a consequence, the mass loss difference between 2D and 3D models is mainly due to the mass exchange between the two circumstellar disks. Note that the apparent increase of the disk mass after it hit the minimum is fictitious and it is due to the difficulty of defining the disk borders during the encounter when the shape of the disk is very elongated and asymmetrical.

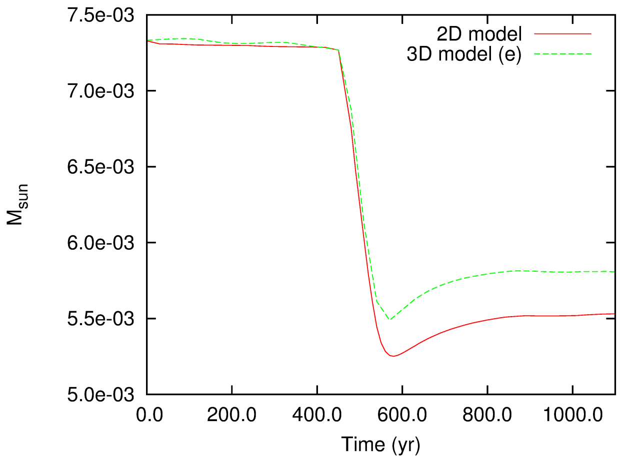

Figure 58: Disk mass evolution in the 3D model e compared to a 2D model with identical initial parameters and integrated with the same SPH code VINE. The mass loss during the encounter is higher in the 2D model.

- Previously published 2D simulations were performed with a grid code having a limited spatial domain centered on the primary star. Mass exiting the grid domain was lost by the system. In the models shown here an SPH code is used and there are no boundaries for the disks. As a consequence, gas excited on highly eccentric trajectories during the stellar flyby is allowed to fall back on the disk at later times while in the simulations with the grid code it was lost. This can be noted also in Fig. 59 where the mass of the disk is computed adding up all the mass moving within $R_{out} = 50$ AU from the star. During the flyby mass is lost but part of it comes back within R_{out} before the onset of an almost constant mass loss due to viscosity, spiral waves excited by the planet and residual disk instability related to the stellar flyby.

- The 2D models were propagated a bit longer in time and this might explain part of the larger mass loss. In the 3D models the disk is still loosing a small amount of mass when we halt the simulation. This last effect, however, accounts for only a small fraction of the difference in the mass loss between 2D and 3D models.

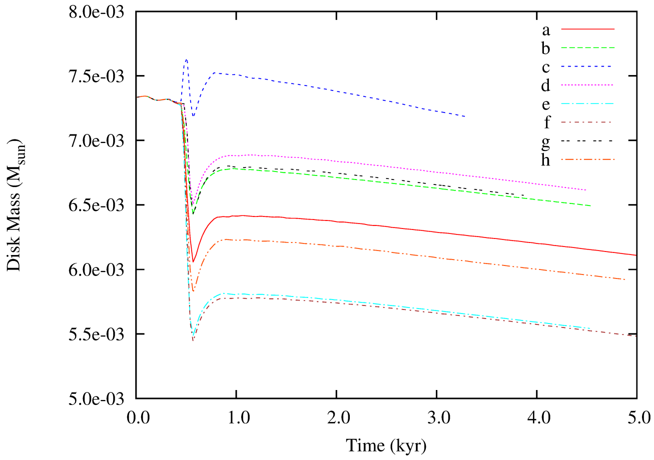

Figure 59: Mass of the disk around the star harbouring the planet as a function of time for the different models summarized in Tab. 7. The flyby is marked by a jump followed by a slow mass decrease.

Since the aim of our calculations is to show that the disk damps the excitation caused by the stellar flyby on the planet orbital elements, we are interested in the mass loss only occurring during the damping. The disk, in this short timescale (~ 5 kyr), possibly does not reach a configuration where the mass loss is only due to viscosity and spiral waves excited by the planet but it is still loosing mass because of the binary perturbations. However, this is not relevant for our computations since the damping of the planet orbit has already occurred.

The mass exchange might cause a limited variation in the original metallicity of the disk compared to that of the host star assuming that the two encountering stars have significantly different values of metallicity. However, the amount of pollution is tiny and possibly without significant consequences for planet formation. The reduced mass loss in the more realistic 3D models presented here leads to a longer lifetime of the disk and a stronger damping effects on the eccentricity and inclination of the planet after the flyby.

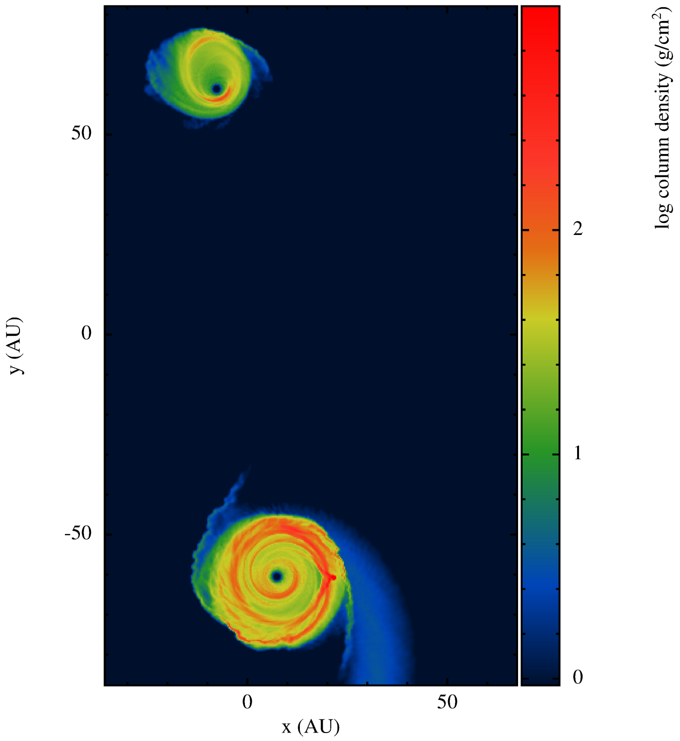

Figure 60: Capture of a disk by the second star, initially without any disk (model e), during the stellar flyby. The plot show the system shortly after the stellar encounter when the material has been transferred from one star to the other via the extended tidal wave.

Table 7: List of models

id	i_{d2}	i_{s2}	q (AU)	nd	$\frac{\Delta M_{d1}}{M_{d1}}$	$\frac{\Delta M_{d2}}{M_{d2}}$	M_{12}	M_{21}	e_{d1}	e_{d2}	i_{d1}	i_{d2}
a	45°	0°	55	2	−16%	−3%	11%	10%	0.09	0.09	2.6°	−3.4°
b	45°	0°	65	2	−11%	−1%	7%	6%	0.05	0.05	1.0°	−1.8°
c	45°	60°	55	2	−2%	−17%	3%	13%	0.04	0.07	8.5°	2.0°
d	0°	0°	55	2	−6%	−5%	8%	11%	0.08	0.09	0.0°	0.0°
e	...	0°	55	1	−21%	...	15%	0%	0.08	0.31	0.0°	0.0°
f	180°	0°	55	2	−24%	2%	8%	2%	0.07	0.17	0.0°	0.0°
g	60°	30°	55	2	−10%	−8%	9%	11%	0.06	0.05	9.2°	58.9°
h	−60°	30°	55	2	−17%	2%	10%	5%	0.06	0.06	6.0°	61.6°

Each simulation is labelled by an alphabet letter in the column indicated with 'id'. i_{d2} is the mutual inclination between the two disks defined by a rotation along the x-axis, i_{s2} is the inclination of the hyperbolic trajectory of the second star computed respect to the initial plane of the primary disk, q is the minimum approach distance during the flyby and nd indicates the number of disks included in the simulation. At the end of each simulation we have computed the amount of mass lost by disk 1 $\frac{\Delta M_{d1}}{M_{d1}}$ and disk 2 $\frac{\Delta M_{d2}}{M_{d2}}$. M_{12} and M_{21} are the amount of mass transferred by one disk to the other. e_{d1}, e_{d1}, i_{d1} and i_{d1} are the disk eccentricities and inclinations.

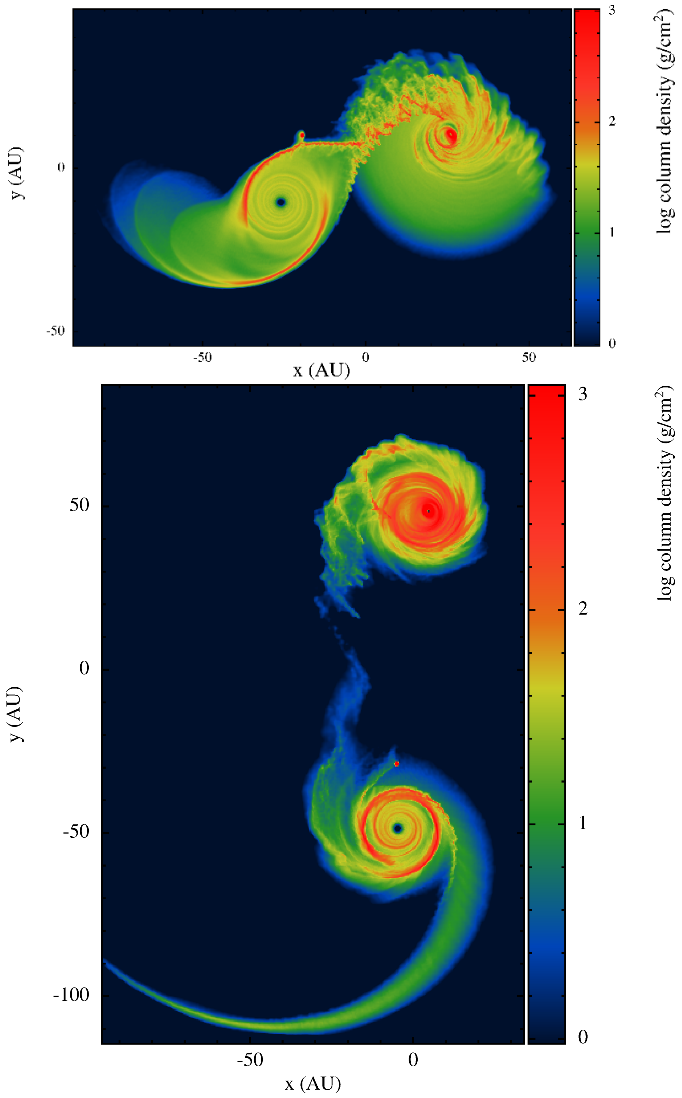

Figure 61: Logarithm of the superficial density (column integrated) of the circumstellar disks at 2 different evolutionary steps for the model e. Due to the geometry of the system, the evolution of the two disks is asymmetric.

9.3.5 *Highly misaligned configurations:* g *and* h

We finally considered two cases with a large mutual inclination between the disks and an inclined hyperbolic trajectory for the star. In cases g and h $i_{d2} = 60^\circ$ and $i_{d2} = -60^\circ$, respectively, while $i_{s2} = 30^\circ$. In Fig. 62 we illustrate the orbital evolution of the planet. The evolution of the semimajor axis and eccentricity is very similar to that of the other cases previously discussed. It is noteworthy that the initial eccentricity step is inversely proportional to i_{s2}, the inclination of the hyperbolic orbit respect to the primary disk plane. When $i_{s2} = 0^\circ$ the jump is about 0.5, for $i_{s2} = 30^\circ$ it is slightly smaller than 0.4 while it reduces to 0.2 when $i_{s2} = 60^\circ$. A similar trend was observed also by Forgan and Rice (2009) and it may then be unnecessary to test higher inclined configurations since the Δe would be smaller.

A small difference between cases g and h in terms of eccentricity damping rate can be ascribed to the different mass loss of the two disks. In case g the disk mass is reduced by 10% after about 3000 yr while in case h 17% of the mass is lost after the same time interval (Tab. 7).

As in case c, the mutual inclination between the planet and disk is reduced and the planet is quickly pulled back into the disk (Fig. 62 bottom plot). Even in this highly inclined configuration, the maximum inclination of the disk (and planet) around the primary star is excited to a maximum of about 9° (case g) which will be the final misalignment between the equatorial plane of the star and the final planet orbit after the disk dissipation.

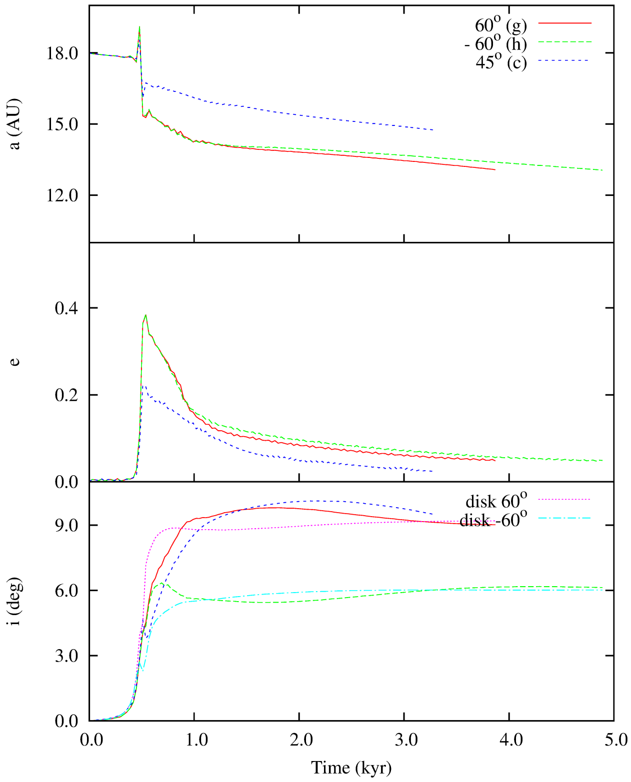

Figure 62: Evolution of the planet orbital elements (a, e, i) in cases g, and h, compared with the test case c. In the bottom panel we also plot the inclinations of the primary disks in the two models g, and h (labelled disk 60°, and disk -60°). The bottom panel shows that the planet is dragged to the disk plane on a short timescale (~ 3 Kyr).

9.4 CONCLUSIONS

We have shown that circumstellar disks are able to absorb the effects of close stellar encounters on planetary systems orbiting stars in clusters. The orbital changes a planet undergoes during a close stellar flyby are quickly damped by the interaction with the disk on a timescale on the order of 10 kyr (and even shorter for 3D simulations). This damping is very efficient since in our simulations we consider evolved disks with a density at least ten times lower than the MMSN. This assumption is dictated by the fact that planets take time to form and in the meantime the disk is slowly dissipating by viscous evolution and photo–evaporation. Furthermore, the relevance of this damping may be significant since stellar flybys are expected to be more frequent and closer in the early stages of a stellar cluster lifetime. As a matter of fact, the timescale on which a cluster loses its gaseous component and begins to disperse is comparable to the circumstellar disk lifetime. Statistically, a large fraction of close stellar encounters are expected to occur while the circumstellar disk is still present and able to damp the eccentricity induced by the stellar flyby.

We find some significant differences between 2D and 3D simulations.

- The mass lost by the primary disk during the stellar flyby depends on the 3D geometry of the encounter and does not lead to the large mass loss observed in 2D simulations. The difference is mainly due to the inclusion of a disk around the passing star that exchange mass with the primary disk during the close encounter and the use of an SPH code that allows us to better track the evolution of the gas far away from the stars.

- The semimajor axis of the planet just after the encounter migrates inward at a slower rate in 3D simulations compared to 2D models. Type II migration of an eccentric orbit, like that of the planet just after the encounter, appears to be significantly less efficient in 3D models.

- The initial eccentricity excited by the stellar flyby is damped more quickly in 3D models and this is partly due to the reduced amount of mass lost by the disk.

We also observed a slower eccentricity damping efficiency when the orbit of the planet is inclined respect to the disk due to a slightly weaker disk–planet interaction.

The only observable difference after the close approach in the 3D model may be a residual misalignment between the planet–disk orbital plane and the star equatorial plane. In fact, during the encounter, the disk harbouring the planet is warped by the interaction with the passing star and its disk. Then it relaxes on a new plane tilted respect to the original one. In our models we find a maximum tilting of about 9°. Subsequently, the planet is pulled back into the disk by tidal interaction with the gas and its orbit also becomes inclined respect to the star equatorial plane. If there are repeated stellar flybys the final tilting of the planet orbit may be larger but it appears unlikely that this mechanism may lead to the large planet inclinations found (Triaud et al., 2010).

Our results do not imply that stellar flybys do not affect the evolution of planetary systems in clusters. However, they may do it in a more subtle way if the circumstellar disk is still present. The evolution of the system, in particular planet migration, is faster when the eccentricity is excited and the disk may also temporarily enhance the eccentricity excitation, as shown in the case of three planet systems in the 2D model. Even planets close encounters can occur, but after the period of dynamical excitation, the disk damps the eccentricity and inclination, the system returns to a quiet state, and it resumes normal migration speed.

By inspecting the dynamical properties and architecture of planetary systems orbiting around stars that were members of clusters, it would be difficult 'a posteriori' to distinguish between systems whose evolution was influenced by stellar flybys and those that were not. The influence of stellar flybys will be detectable only on a statistical basis as shown by the modeling of Fragner and Nelson (2009). Many parameters are indeed affecting the behavior of the disk+planet system during the stellar flyby and they include the initial disk density profile and the architecture of the planetary system. A large number of simulations are required to statistically assess the contribution of stellar flybys to the evolution of planetary systems in clusters.

Concerning the effects of stellar flybys on planetary systems in stellar cluster, we do not expect any signature of the stellar encounters in the eccentricity of the planets. Some misalignment between the planet orbit and the star equatorial plane may appear but it would be limited. Repeated stellar flybys may excite a significant misalignment between the star equatorial plane and the planet orbit but its extent depends on the stellar cluster star density. A period of fast type II migration may occur after the stellar encounter since any gap created by the planet before the flyby is destroyed during the strong interaction between the stars and the disks at the pericenter. A new gap is created when the planet is finally pulled back into the disk midplane and its orbit circularized. The rate at which the disks are destroyed in clusters may be slower than expected since when two stars have an encounter, their disks exchange mass rather than loosing it.

In our modeling, we have considered a rather extreme configuration for the encounter in terms of flyby distance and planet orbit. It would be interesting to explore in more detail the effects of repeated close encounters on more complex planetary systems. For example, an exploration on the consequences of stellar encounters in systems of 3 planets, like that in our 2D model, would be interesting also in 3D. The parameter space is really huge and many different configurations may be envisaged in light of recent discoveries of extrasolar planetary systems. However, according to our results, it appears reasonable to expect that if the damping works in extreme conditions it should be effective also in different, potentially more complex, scenarios.

10

CONCLUSIONS

The standard model of planet formation developed on the ground of Solar System observations and exploration failed to predict the two very first discoveries of an exoplanet. In effect, the first was detected around the pulsar PSR B1257+12 (Wolszczan and Frail, 1992), proving that Solar–type stars are not the only stars hosting planets. Most puzzling, the second one (Mayor and Queloz, 1995), even if detected around a Solar type star, was a Jupiter class planet orbiting its host star with a semimajor axis smaller than that of Mercury.

Since then, the theory of planet formation and evolution (reviewed in this Thesis) has made huge steps in the understanding of the basic processes at play, with the aid of planet detection surveys which had furnished an increasing and various sample of planets, and more realistics computer simulations on which to test the developing theory.

The most interesting scenario in this context is that of binary star systems, which are a test bench of paramount importance for the planet formation process.

In this Thesis I presented two original works in which I have addressed planet formation in these complex scenarios. In the first one (Chap. 6) I have studied the evolution of circumstellar protoplanetary disks in close binary systems, verifying that the conditions for planetesimal formation are prohibitive due to the tidal interaction of the companion star which truncates the disk, heats it up, and excites strong tidal waves during the periastron passages. However, these effects are strongly dependant on the binary semimajor axis and they are considerably reduced for wider systems.

In the second work I have considered the planetesimal stage of planet formation in the 16–Kepler system, showing that, due to the presence of the companion star, the circumbinary gas disk becomes eccentric. The asymmetric gravity field of the disk excites the planetesimals eccentricities and their perihelia alignment is partially destructed, leading to prohibitive impact velocities inside 10 AU from the binary for planetesimal sizes of 5 and 25 km in size. The planet observed in this system near the dynamical stability limit could be explained assuming that it formed in the outer zones of the protoplanetary disk and then migrated inside.

It is also of fundamental importance to study the planetary system evolution after the planet formation process, in order to predict the actual planetary system configurations.

In particular, I have studied both in 2 and 3 dimensions the influence that a close stellar encounter in an open cluster could have on an evolving planetary system, in order to predict the effects of this mechanism on the overall statistics of planets in clusters. I found that even a rarefied gas disk, which is expected to be still present after the cluster dispersal, could effectively damp eccentricity and inclination excitations caused by stellar flyby.

These studies are not a mere intellectual play, since it has been proven that the fraction of binary stars is almost equal to that of single Solar–type stars (Duquennoy and Mayor, 1991; Raghavan et al., 2010), and it is even higher in star forming regions (Parker et al., 2011). Thus, in order to understand planet formation one has to take into account binary stars.

The possibility to find an Earth analogue with modern technologies and dedicated space missions had burst the interest in this scientific field. However, up to now there have been two important limitations, namely, selection and bias effects, and difficulties in the physical characterization of detected planets.

With the next generation of space missions devoted to planet detection we are entering a new era in this scientific field, since we will obtain a complete characterization of the bulk and atmosphere properties of extrasolar planets down to Earth–size.

In particular, the PLATO mission is the most promising, having the possibility to detect a wide range of planetary systems due to its long–based observational strategy, and to take advantage of the huge amount of stellar data from the Gaia mission that will help PLATO both in the target selection phase, and in a better characterization of the planet physical parameters.

From the next generation missions we will obtain an unprecedented picture of planetary systems evolution at play, that will revolutionize our understanding of the planet formation process.

PLATO will survey a complete sample of stars in nearly half of the sky, reducing the selection effects observed in past space missions (see Chap. 4), and giving us a more realistic picture of planet evolution in different stellar environments. Thus, we would better understand the influence of stellar types and multiplicity on planet formation.

Moreover, it would be capable of detecting planets orbiting binaries in S–type orbits (see Chap. 6) down to the smaller limit of binary semi–major axis for planet formation ($a_b = 10$–20 AU) and, thanks to its observational strategy, it would be able to detect multi–planetary systems in close configurations ($a_b < 100$ AU). Hence, it would be possible to address the different planet mass distribution observed so far in the binary environment (see Chap. 4), confirming the possibility of a more complex formation process.

Concerning the fascinating category of circumbinary planets, the unprecedented amount of stellar data from Gaia would allow to select a large sample of binary stars to be observed in search of planets by PLATO. This in turn could help us to understand the trends observed in circumbinary planet systems, such as the planet packing near the dynamical stability limit (Chap. 7).

The information about stellar ages, that PLATO would obtain, could improve greatly our understanding of long–term dynamical processes at play in binary and multiplanet systems such as Kozai resonances with a distant companion (see Sec. 8.3.2), or planet–planet scattering (see Sec. 8.4.2).

With the aid of dedicated spectroscopic follow–ups, PLATO will also give a statistical distribution of inclinations and eccentricities in open clusters via the Rossiter–McLaughlin effect (where possible), giving potential clues on the origin of the mutual inclination between the star equatorial plane and the planet orbital plane.

As I have shown in Chap. 9, stellar encounters cannot account for a significant amount of such inclinations.

The binary star environment is a great opportunity, not an impediment like in the first exoplanet surveys, to investigate planet formation, evolution and dynamical behaviour. It will be nice if the first Earth analogue would be detected in the habitable zone of a binary (or multiple) star system.

Part V

APPENDIX

A

THE SPH METHOD

A.1 INTRODUCTION

The Smoothed Particle Hydrodynamics (SPH) is a Lagrangian method of solving the equations of fluid dynamics (Gingold and Monaghan, 1977). In other words, it obtains approximate numerical solutions of the equations of fluid dynamics by replacing the fluid with a set of particles.

This method has been adopted to simulate a large sample of astrophysical scenarios, from the large scale of cosmological problems to the small one of planet formation processes. This versatility is due to its ability to deal with no fixed boundary problems and a high spatial adaptivity (Lodato and Cossins, 2011), which are fundamental properties in the astrophysical context.

For our simulations we have successfully adopted the 3D SPH code VINE (Wetzstein et al., 2009; Nelson et al., 2009). Moreover, we have updated it with some important features that improve momentum and energy conservation during the simulations, and we have implemented a fully radiative approach so that the viscous heating is diffused in the disk and emitted at the disk's outer borders. The flux–limited approximation, as described in Levermore and Pomraning (1981), is used in the code. Here below we describe in detail the substantial modifications to the original code.

A.2 VARIABLE SMOOTHING LENGTH

The basic idea of the variable smoothing length method (Price and Monaghan, 2004; Springel and Hernquist, 2002) is that the smoothing length h is related to the particle coordinates through a relation between h and the particle density ρ

$$\frac{\partial h_a}{\partial \mathbf{r}_b} = \frac{\partial h_a}{\partial \rho_a}\frac{\partial \rho_a}{\partial \mathbf{r}_b}. \tag{154}$$

The ansatz on the dependence of h on ρ is of the form

$$h_a = \eta \left(\frac{m_a}{\rho_a}\right)^{1/3}, \tag{155}$$

where η is a dimensionless parameter that specifies the size of the smoothing length in terms of averaged particle spacing (setting η to

1.2 gives in 3D about 60 particles around any given one). The derivative of the above equation respect to ρ gives

$$\frac{\partial h_a}{\partial \rho_a} = -\frac{h_a}{3\rho_a}. \tag{156}$$

The density definition in VINE is given by

$$\rho(\mathbf{r}_a) = \sum_{b=1}^{N} m_b W(\mathbf{r}_{ab}, h_{ab}), \tag{157}$$

where $\mathbf{r}_{ab} = |\mathbf{r}_a - \mathbf{r}_b|$ and $h_{ab} = (h_a + h_b)/2$, so we have a nonlinear equation to be solved for both h and ρ.

To find a self–consistent solution to eq. (155–157), we have to solve the following equation

$$f(h_a) = \rho_a(h_a) - \rho_{sum}(h_a) = 0, \tag{158}$$

with a Newton–Raphson method until convergence is reached. The derivative of the function $f(h_a)$ is

$$f'(h_a) = \frac{\partial \rho_a}{\partial h_a} - \sum_b m_b \frac{\partial W_{ab}}{\partial h} = -\frac{3\rho_a}{h_a}\Omega_a, \tag{159}$$

where

$$\Omega_a = \left[1 - \frac{\partial h_a}{\partial \rho_a} \sum_b m_b \frac{\partial W_{ab}}{\partial h}\right], \tag{160}$$

accounts for the gradient of the smoothing length. Convergence is assumed to occur when $|h_{new} - h|/h_0 < \epsilon = 10^{-3}$. Due to the dependence of h on ρ, the equations of motion are changed accordingly

$$\frac{d\mathbf{v}_a}{dt} = -\sum_b m_b \left(\frac{P_a}{\rho_a^2 \Omega_a} + \frac{P_b}{\rho_b^2 \Omega_b} + \Pi_{ab}\right) \nabla_b W_{ab}, \tag{161}$$

where Π_{ab} is the artificial viscous pressure term. The continuity equation becomes

$$\frac{d\rho_a}{dt} = \frac{1}{\Omega_a} \sum_b m_b (\mathbf{v}_a - \mathbf{v}_b) \cdot \nabla_b W_{ab}, \tag{162}$$

and the energy equation

$$\frac{du_a}{dt} = \frac{P_a}{\Omega_a \rho_a^2} \sum_b m_b \mathbf{v}_{ab} \cdot \nabla_b W_{ab} + \frac{1}{2} \sum_b m_b \Pi_{ab} \mathbf{v}_{ab} \cdot \nabla_b W_{ab}, \tag{163}$$

where $\mathbf{v}_{ab} = \mathbf{v}_a - \mathbf{v}_b$.

The artificial viscosity term is added a) to correctly model shock waves that inject entropy into the flow over distances that are much shorter than a smoothing length and b) to simulate the evolution of viscous disks. The Π term broadens the shock over a small number of smoothing lengths and correctly resolves it ensuring at the same time that the Rankine–Hugoniot equations are satisfied. In this way it prevents discontinuities in entropy, pressure, density, and velocity fields. SPH simulations (Monaghan and Gingold, 1983) include both a linear term (bulk viscosity), which dissipates kinetic energy as particles approach each other to reduce subsonic velocity oscillations following a shock, and a quadratic term (von Neumann–Richtmyer viscosity), which convert kinetic energy to thermal energy preventing particle interpenetration in shocks

$$\Pi_{ab} = \begin{cases} (-\alpha_{SPH} c_{ab} \mu_{ab} + \beta_{SPH} \mu_{ab}^2)/\rho_{ab} & \mathbf{v}_{ab} \cdot \mathbf{r}_{ab} \leqslant 0, \\ 0 & \mathbf{v}_{ab} \cdot \mathbf{r}_{ab} > 0, \end{cases} \tag{164}$$

where all quantities are symmetrized. The term μ_{ab} plays the role of the velocity divergence,

$$\mu_{ab} = \frac{h_{ab} \mathbf{v}_{ab} \cdot \mathbf{r}_{ab}}{\mathbf{r}_{ab}^2 + \eta^2 h_{ab}^2} f_{ab}, \tag{165}$$

with $\eta << 1$ to prevent singularities as particles approach, while f_{ab} (Balsara, 1995) is introduced to avoid large entropy generation in pure shear flows and is defined as

$$f_a = \frac{| < \nabla \cdot \mathbf{v}_a > |}{| < \nabla \cdot \mathbf{v}_a > | + | < \nabla \times \mathbf{v}_a > | + \eta'}, \tag{166}$$

where again $\eta' << 1$ is a factor used to prevent singularities, and α_{SPH} and β_{SPH} determine the strength of the artificial viscosity. In general they are set initially to 0.1 and 0.2, respectively, but they can vary during the simulation, keeping only their ratio fixed (Morris and Monaghan, 1997; Rosswog et al., 2000).

The shear viscosity contribution deriving from the linear and quadratic artificial viscosity terms can be compared to the Shakura and Sunyaev (1973) viscosity α_{SS} as in Meru and Bate (2012):

$$\alpha_{SS} = \alpha_{SS,lin} + \alpha_{SS,quad} = \frac{31}{525} \alpha_{SPH} \frac{h}{H} + \frac{9}{70\pi} \beta_{SPH} \left(\frac{h}{H} \right)^2. \tag{167}$$

It has been shown (Monaghan, 1985; Lodato and Price, 2010; Meru and Bate, 2012) that even in the continuum limit, the artificial viscosity terms α_{SPH} and β_{SPH} mimic a Navier–Stokes viscosity.

A.3 VARIABLE SOFTENING LENGTH

The variable softening length method is needed when self–gravity is included in the model (Price and Monaghan, 2007). The modified gravitational potential per unit mass may be written in the form

$$\Phi(\mathbf{r}) = -G \sum_b m_b \phi(|\mathbf{r} - \mathbf{r}_b|), \tag{168}$$

where ϕ is a softening kernel that is a function of the particle separation and the softening length (h, which corresponds to the smoothing length as in Price and Monaghan (2007)). The form of ϕ is given below. The gravitational force in $\mathbf{r}$ is computed as

$$\mathbf{F}(\mathbf{r}) = -\nabla\Phi = -G\sum_b m_b \phi'(|\mathbf{r}-\mathbf{r}_b|)\frac{\mathbf{r}-\mathbf{r}_b}{|\mathbf{r}-\mathbf{r}_b|}, \tag{169}$$

where $\phi' = \partial\phi/\partial|\mathbf{r}-\mathbf{r}_b|$, and we have neglected the spatial variation of h. To get an expression for ϕ, the Poisson's equation is used

$$\nabla^2\Phi = 4\pi G\rho, \tag{170}$$

and by using the SPH definition for the density (eq. 157), it is possible to derive a relation between the smoothing kernel W and the softening kernel ϕ

$$W(r) = -\frac{1}{4\pi r^2}\frac{\partial}{\partial r}\left(r^2\frac{\partial\phi}{\partial r}\right). \tag{171}$$

The kernel softens the gravity from neighbor particles while it is the usual $1/r$ potential for those far away. The additional terms to the equation of motion due to the self–gravity are (Price and Monaghan, 2007)

$$\begin{aligned}\frac{d\mathbf{v}_a}{dt} =& -G\sum_b m_b \phi'_{ab}(h_{ab})\frac{\mathbf{r}_a-\mathbf{r}_b}{|\mathbf{r}_a-\mathbf{r}_b|}\\ &-\frac{G}{2}\sum_b m_b\left[\frac{\zeta_a}{\Omega_a}+\frac{\zeta_b}{\Omega_b}\right]W'_{ab}(h_{ab}),\end{aligned} \tag{172}$$

where the first term represents the softened gravitational force, and the second one is used when the adapting softening length is adopted and restore the energy conservation with

$$\zeta_a = \frac{\partial h_a}{\partial\rho_a}\sum_b m_b\frac{\partial\phi_{ab}}{\partial h}. \tag{173}$$

A.4 SPH IMPLEMENTATION OF RADIATION HYDRODYNAMICS IN THE FLUX–LIMITED DIFFUSION

The coupled energy equations describing the evolution of the specific gas internal energy u_g and of the total frequency–integrated radiation energy ξ are the following (Mihalas and Mihalas, 1984; Whitehouse and Bate, 2004):

$$\frac{D\xi}{Dt} = -\frac{\nabla\cdot\mathbf{F}}{\rho}-\frac{\nabla\mathbf{v}:\mathbf{P}}{\rho}-ac\kappa\left[\frac{\rho\xi}{a}-\left(\frac{u_g}{c_v}\right)^4\right], \tag{174}$$

$$\frac{Du_g}{Dt} = -\frac{P\nabla\cdot\mathbf{v}}{\rho}+ac\kappa\left[\frac{\rho\xi}{a}-\left(\frac{u_g}{c_v}\right)^4\right], \tag{175}$$

where $a = 4\sigma_B/c$ and κ is the mean absorption opacity. The term $\frac{\nabla\cdot\mathbf{F}}{\rho}$ on the right–hand side of eq. (174) is the radiation flux term. For an isotropic radiation field (*Eddington approximation*), the radiative flux is given by

$$\mathbf{F} = -\frac{c}{3\chi\rho}\nabla E, \tag{176}$$

where χ is the total opacity, which is the sum of absorption and scattering terms; E is the radiative energy density $E = \xi \cdot \rho$; and c is the light speed. In optically thin regions where $\chi \to 0$ the Eddington approximation fails ($\mathbf{F} \to \infty$), since photons travel freely and their free paths may exceed characteristic lengths of the system, making the radiation field anisotropic. In this case the flux–limited approximation is used (Levermore and Pomraning, 1981) and the radiation flux can be written as a Fick's law of diffusion

$$\mathbf{F} = -D\nabla E, \tag{177}$$

where $D = c\lambda/(\chi\rho)$ is a diffusion coefficient, and the dimensionless function $\lambda = \lambda(E)$ is the flux–limiter defined as (Levermore and Pomraning, 1981; Whitehouse and Bate, 2004)

$$\lambda(R) = \frac{2+R}{6+3R+R^2}. \tag{178}$$

where R is the dimensionless quantity $R = |\nabla E|/(\chi\rho E)$. In the optically thin limit ($R \to \infty$) the flux limiter tends towards

$$\lim_{R\to\infty} \lambda(R) = \frac{1}{R}, \tag{179}$$

so the magnitude of the flux approaches $|\mathbf{F}| = c|\nabla E|/(\chi\rho R) = cE$. In the optically thick (or diffusion) limit, $R \to 0$ so the flux–limiter

$$\lim_{R\to 0} \lambda(R) = \frac{1}{3} \tag{180}$$

and the flux takes the value given by eq. (176).
The second term on the right–hand side of eq. (174) $\frac{\nabla\mathbf{v}:\mathbf{P}}{\rho}$, describing the radiation pressure, contains the radiation pressure tensor $\mathbf{P}$ that, in the flux–limited approximation, can be expressed in terms of the radiation energy density

$$\mathbf{P} = \mathbf{f}E, \tag{181}$$

where $\mathbf{f}$ is the Eddington tensor, defined as

$$\mathbf{f} = \frac{1}{2}(1-f)\mathbf{I} + \frac{1}{2}(3f-1)\hat{\mathbf{n}}\hat{\mathbf{n}}, \tag{182}$$

where $\hat{\mathbf{n}} = \nabla E/|\nabla E|$ is the unit vector in the direction of the radiation energy density gradient and $f = f(E)$ is a scalar function called the Eddington factor. The flux limiter and the Eddington factor are related through

$$f = \lambda + \lambda^2 R^2, \tag{183}$$

The last term in both eqs. (174) and (175) controls the interaction between the radiation and the gas. In fact we can rewrite the term inside the square bracket as $T_r^4 - T_g^4$.

In non–irradiated protoplanetary disks, the temperatures are low enough that the energy stored in radiation is negligible compared to the thermal energy of the gas ($\xi << u_g$). Under this condition, the so–called one–temperature approach (Kley et al., 2009), the two coupled equations, eqs. (174) and (175), reduce to a single equation for the gas internal energy u_g

$$\frac{Du_g}{Dt} = -\frac{P\nabla\cdot\mathbf{v}}{\rho} - \frac{\nabla\cdot\mathbf{F}}{\rho}. \tag{184}$$

The radiation flux term can be rewritten using the flux–limiter λ as

$$\begin{aligned} -\frac{\nabla\cdot\mathbf{F}}{\rho} &= \frac{1}{\rho}\nabla\cdot\left(\frac{c\lambda}{\kappa_R\rho}\nabla E\right), & (185)\\ &= \frac{1}{\rho}\nabla\cdot\left[\frac{c\lambda}{\kappa_R\rho}\nabla\left(\frac{4\sigma_B}{c}T^4\right)\right], &\\ &= \frac{1}{\rho}\nabla\cdot\left[\frac{16\sigma_B\lambda}{\kappa_R\rho}T^3\nabla T\right], & (186)\end{aligned}$$

where κ_R, the Rosseland mean opacity, approximates χ. To compute κ_R we use a power–law dependence on temperature and density $\kappa_R = \kappa_0\rho^a T^b$ as in Bell and Lin (1994) where the coefficients κ_0, a, and b depend on the opacity regime. The previous equation has the same form of the heat conduction equation

$$\frac{du}{dt} = \frac{1}{\rho}\nabla\cdot(k\nabla T), \tag{187}$$

where k is the thermal conductivity. This similarity is useful when we try to implement the energy equation (eq. 186) in the SPH formalism. Cleary and Monaghan (1999) give in fact the following SPH expression for the heat transport equation

$$\frac{du_a}{dt} = \sum_{b=1}^{N}\frac{m_b}{\rho_a\rho_b}\left(\frac{4k_ak_b}{k_a+k_b}\right)(T_a - T_b)\frac{\nabla W_{ab}}{r_{ab}}. \tag{188}$$

In the case of radiative diffusion, the coefficients k_a and k_b have to be substituted by (Whitehouse and Bate, 2004)

$$k_a = \frac{16\sigma_B}{\kappa_a\rho_a}\lambda_a T_a^3. \tag{189}$$

A.5 COOLING VIA BOUNDARY PARTICLES

While the disk is heated by the viscous dissipation (we neglect star irradiation effects), it is at the same time cooled by the thermal emission into the vacuum at the upper and lower surfaces. To model the radiation escape, we introduce "boundary" particles into the algorithm. These particles populate the regions where the optical depth of the disk τ is equal to 1 (Ayliffe and Bate, 2009; Meru, 2010). To identify the boundary particles among all the particles representing the disk we proceed as follows:

1. The disk is divided in sectors $(r + \Delta r, \theta + \Delta\theta)$;
2. In each sector, SPH particles are sorted along both r and z;
3. The parameter z_b is defined as the height at which the optical depth τ is ≈ 1 so that
$$\tau = -\int_{\infty}^{z_b} \kappa\rho dz. \tag{190}$$
Under the assumption of low temperature and density in the outer layers of the disk, the vertical isothermal approximation can be locally used (thin disk condition) so that the opacity κ is approximately constant and can be taken out of the integral leading to the following expression
$$\tau = \kappa \int_{z_b}^{\infty} \rho dz = \kappa\Sigma_b = 1, \tag{191}$$
where Σ_b is the surface mass density of the boundary particles;
4. In the SPH formalism, the superficial density can be computed as
$$\Sigma = \frac{N m_p}{A_s}, \tag{192}$$
where m_p is the SPH particle mass, N the total number of particles present in the sector (independently of the z coordinate), and A_s the sector area;
5. Knowing Σ_b we can compute N_b, the number of particles populating the layer with $\tau = 1$. This number is given by
$$N_b = \frac{A_s}{\kappa m_p}, \tag{193}$$
This is done in both the positive and negative vertical directions.

The boundary particles evolve normally, but they interact radiatively with the "normal" SPH particles in the bulk of the disk absorbing radiation without releasing it. The amount of heat they are supposed to radiatively transfer to their neighbors, which is computed from the energy equation, is lost to infinity. In this way they act as cooling particles radiating away energy. It is noteworthy that the temperature of the boundary particles is not set to a low value but is in equilibrium with the local temperature profile of the disk. This prevents them from rapidly migrating towards the median plane of the disk due to their low pressure value. However, they absorb the energy of the other particles and act as energy sinks. In Fig. 63 we show two representative vertical temperature profiles obtained from our simulations of disks in binaries. They are computed in a quiet ring far from the center of both the primary and secondary disks to avoid the heating due to strong spiral waves, which also act when the binary is at the apocenter. The cooling due to boundary particles is effective and leads to a decrease in the temperature towards the surfaces of the disk.

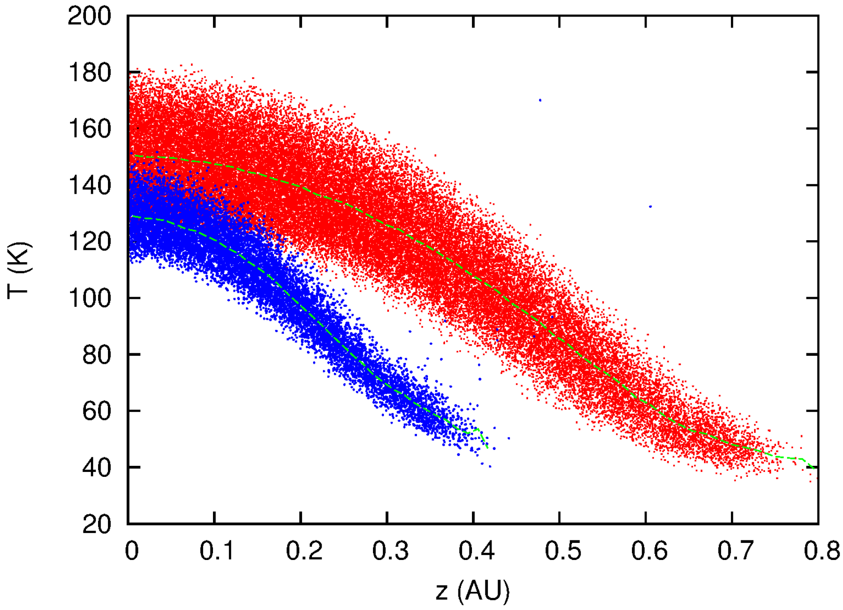

Figure 63: Temperature profiles as a function of the height over the median plane of the disk (z component) for the primary disk at r ~ 6 AU and for the secondary disk at r ~ 3 AU. These locations are far from the center of the disk where the heating due to the spiral waves, even at apocenter, is the strongest. The dots are the individual temperatures of the SPH particles encompassed between 6 and 6.3 AU for the primary disk and 3 and 3.3 AU for the secondary disk. The continuous lines are the average temperature values. The SPH particles of the primary disk are represented by red dots, while blue dots are relative to the secondary disk.

BIBLIOGRAPHY

I. Adachi, C. Hayashi, and K. Nakazawa. The gas drag effect on the elliptical motion of a solid body in the primordial solar nebula. *Progress of Theoretical Physics*, 56:1756–1771, December 1976. doi: 10.1143/PTP.56.1756.

F. C. Adams. Theoretical Models of Young Open Star Clusters: Effects of a Gaseous Component and Gas Removal. *ApJ*, 542:964–973, October 2000. doi: 10.1086/317052.

E. Agol, J. Steffen, R. Sari, and W. Clarkson. On detecting terrestrial planets with timing of giant planet transits. *MNRAS*, 359:567–579, May 2005. doi: 10.1111/j.1365-2966.2005.08922.x.

L. Allen, S. T. Megeath, R. Gutermuth, P. C. Myers, S. Wolk, F. C. Adams, J. Muzerolle, E. Young, and J. L. Pipher. The Structure and Evolution of Young Stellar Clusters. *Protostars and Planets V*, pages 361–376, 2007.

P. J. Armitage. *Astrophysics of Planet Formation*. Cambridge University Press, 2010.

P. Artymowicz and S. H. Lubow. Dynamics of binary-disk interaction. 1: Resonances and disk gap sizes. *ApJ*, 421:651–667, February 1994. doi: 10.1086/173679.

E. Asphaug, M. Jutzi, and N. Movshovitz. Chondrule formation during planetesimal accretion. *Earth and Planetary Science Letters*, 308: 369–379, August 2011. doi: 10.1016/j.epsl.2011.06.007.

B. A. Ayliffe and M. R. Bate. Gas accretion on to planetary cores: three-dimensional self-gravitating radiation hydrodynamical calculations. *MNRAS*, 393:49–64, February 2009. doi: 10.1111/j.1365-2966.2008.14184.x.

A. Baglin, M. Auvergne, L. Boisnard, T. Lam-Trong, P. Barge, C. Catala, M. Deleuil, E. Michel, and W. Weiss. CoRoT: a high precision photometer for stellar ecolution and exoplanet finding. In *36th COSPAR Scientific Assembly*, volume 36 of *COSPAR Meeting*, page 3749, 2006.

D. S. Balsara. von Neumann stability analysis of smooth particle hydrodynamics–suggestions for optimal algorithms. *Journal of Computational Physics*, 121:357–372, 1995. doi: 10.1016/S0021-9991(95) 90221-X.

C. Baruteau and F. Masset. On the Corotation Torque in a Radiatively Inefficient Disk. *ApJ*, 672:1054–1067, January 2008. doi: 10.1086/523667.

M. R. Bate, I. A. Bonnell, and N. M. Price. Modelling accretion in protobinary systems. *MNRAS*, 277:362–376, November 1995.

C. Beaugé, S. Ferraz-Mello, and T. A. Michtchenko. *Planetary Masses and Orbital Parameters from Radial Velocity Measurements*, page 1. 2007.

C. Beaugé, A. M. Leiva, N. Haghighipour, and J. C. Otto. Dynamics of planetesimals due to gas drag from an eccentric precessing disc. *MNRAS*, 408:503–513, October 2010. doi: 10.1111/j.1365-2966.2010.17132.x.

C. P. M. Bell, T. Naylor, N. J. Mayne, R. D. Jeffries, and S. P. Littlefair. Pre-main-sequence isochrones - II. Revising star and planet formation time-scales. *MNRAS*, 434:806–831, September 2013. doi: 10.1093/mnras/stt1075.

K. R. Bell and D. N. C. Lin. Using FU Orionis outbursts to constrain self-regulated protostellar disk models. *ApJ*, 427:987–1004, June 1994. doi: 10.1086/174206.

B. Bitsch and W. Kley. Orbital evolution of eccentric planets in radiative discs. *A&A*, 523:A30, November 2010. doi: 10.1051/0004-6361/201014414.

B. Bitsch, A. Crida, A. Morbidelli, W. Kley, and I. Dobbs-Dixon. Stellar irradiated discs and implications on migration of embedded planets. I. Equilibrium discs. *A&A*, 549:A124, January 2013. doi: 10.1051/0004-6361/201220159.

J. Blum and G. Wurm. The Growth Mechanisms of Macroscopic Bodies in Protoplanetary Disks. *ARA&A*, 46:21–56, September 2008. doi: 10.1146/annurev.astro.46.060407.145152.

A. C. Boley and R. H. Durisen. Gravitational Instabilities, Chondrule Formation, and the FU Orionis Phenomenon. *ApJ*, 685:1193–1209, October 2008. doi: 10.1086/591013.

A. C. Boley, R. H. Durisen, and M. K. Pickett. The Three-Dimensionality of Spiral Shocks: Did Chondrules Catch a Breaking Wave? In A. N. Krot, E. R. D. Scott, and B. Reipurth, editors, *Chondrites and the Protoplanetary Disk*, volume 341 of *Astronomical Society of the Pacific Conference Series*, page 839, December 2005.

M. Bonavita and S. Desidera. The frequency of planets in multiple systems. *A&A*, 468:721–729, June 2007. doi: 10.1051/0004-6361:20066671.

N. Borderies and P. Goldreich. A simple derivation of capture probabilities for the J + 1 : J and J + 2 : J orbit-orbit resonance problems. *Celestial Mechanics*, 32:127–136, February 1984. doi: 10.1007/BF01231120.

A. P. Boss. Giant planet formation by gravitational instability. *Science*, 276:1836–1839, 1997. doi: 10.1126/science.276.5320.1836.

A. P. Boss and R. H. Durisen. Chondrule-forming Shock Fronts in the Solar Nebula: A Possible Unified Scenario for Planet and Chondrite Formation. *ApJL*, 621:L137–L140, March 2005. doi: 10.1086/429160.

A. P. Boss and J. A. Graham. Clumpy disk accretion and chondrule formation. *Icarus*, 106:168, November 1993. doi: 10.1006/icar.1993.1164.

T. M. Brown, D. W. Latham, M. E. Everett, and G. A. Esquerdo. Kepler Input Catalog: Photometric Calibration and Stellar Classification. *AJ*, 142:112, October 2011. doi: 10.1088/0004-6256/142/4/112.

D. A. Caldwell, J. J. Kolodziejczak, J. E. Van Cleve, J. M. Jenkins, P. R. Gazis, V. S. Argabright, E. E. Bachtell, E. W. Dunham, J. C. Geary, R. L. Gilliland, H. Chandrasekaran, J. Li, P. Tenenbaum, H. Wu, W. J. Borucki, S. T. Bryson, J. L. Dotson, M. R. Haas, and D. G. Koch. Instrument Performance in Kepler's First Months. *ApJL*, 713: L92–L96, April 2010. doi: 10.1088/2041-8205/713/2/L92.

A. G. W. Cameron. Physics of the primitive solar accretion disk. *Moon and Planets*, 18:5–40, February 1978. doi: 10.1007/BF00896696.

B. Campbell, G. A. H. Walker, and S. Yang. A search for substellar companions to solar-type stars. *ApJ*, 331:902–921, August 1988. doi: 10.1086/166608.

P. Cassen and D. S. Woolum. Radiatively Damped Density Waves in Optically Thick Protostellar Disks. *ApJ*, 472:789, December 1996. doi: 10.1086/178107.

R. Chandar, S. M. Fall, and B. C. Whitmore. New Tests for Disruption Mechanisms of Star Clusters: The Large and Small Magellanic Clouds. *ApJ*, 711:1263–1279, March 2010. doi: 10.1088/0004-637X/711/2/1263.

S. Chatterjee, E. B. Ford, S. Matsumura, and F. A. Rasio. Dynamical Outcomes of Planet-Planet Scattering. *ApJ*, 686:580–602, October 2008. doi: 10.1086/590227.

F. J. Ciesla, L. L. Hood, and S. J. Weidenschilling. Evaluating planetesimal bow shocks as sites for chondrule formation. *Meteoritics and Planetary Science*, 39:1809–1821, November 2004. doi: 10.1111/j.1945-5100.2004.tb00077.x.

P. W. Cleary and J. J. Monaghan. Conduction Modelling Using Smoothed Particle Hydrodynamics. *Journal of Computational Physics*, 148:227–264, January 1999. doi: 10.1006/jcph.1998.6118.

A. C. M. Correia, S. Udry, M. Mayor, A. Eggenberger, D. Naef, J.-L. Beuzit, C. Perrier, D. Queloz, J.-P. Sivan, F. Pepe, N. C. Santos, and D. Ségransan. The ELODIE survey for northern extra-solar planets. IV. HD 196885, a close binary star with a 3.7-year planet. *A&A*, 479: 271–275, February 2008. doi: 10.1051/0004-6361:20078908.

J. N. Cuzzi, R. C. Hogan, and K. Shariff. Toward Planetesimals: Dense Chondrule Clumps in the Protoplanetary Nebula. *ApJ*, 687:1432–1447, November 2008. doi: 10.1086/591239.

S. Daemgen, S. Correia, and M. G. Petr-Gotzens. Protoplanetary disks of T Tauri binary systems in the Orion nebula cluster. *A&A*, 540: A46, April 2012. doi: 10.1051/0004-6361/201118314.

X. Delfosse, J.-L. Beuzit, L. Marchal, X. Bonfils, C. Perrier, D. Ségransan, S. Udry, M. Mayor, and T. Forveille. M dwarfs binaries: Results from accurate radial velocities and high angular resolution observations. In R. W. Hilditch, H. Hensberge, and K. Pavlovski, editors, *Spectroscopically and Spatially Resolving the Components of the Close Binary Stars*, volume 318 of *Astronomical Society of the Pacific Conference Series*, pages 166–174, December 2004.

S. J. Desch and H. C. Connolly, Jr. A model of the thermal processing of particles in solar nebula shocks: Application to the cooling rates of chondrules. *Meteoritics and Planetary Science*, 37:183–207, February 2002. doi: 10.1111/j.1945-5100.2002.tb01104.x.

S. J. Desch and J. N. Cuzzi. The Generation of Lightning in the Solar Nebula. *Icarus*, 143:87–105, January 2000. doi: 10.1006/icar.1999.6245.

S. Desidera and M. Barbieri. Properties of planets in binary systems. The role of binary separation. *A&A*, 462:345–353, January 2007. doi: 10.1051/0004-6361:20066319.

S. B. Dieterich, T. J. Henry, D. A. Golimowski, J. E. Krist, and A. M. Tanner. The Solar Neighborhood. XXVIII. The Multiplicity Fraction of Nearby Stars from 5 to 70 AU and the Brown Dwarf Desert around M Dwarfs. *AJ*, 144:64, August 2012. doi: 10.1088/0004-6256/144/2/64.

L. R. Doyle, J. A. Carter, D. C. Fabrycky, R. W. Slawson, S. B. Howell, J. N. Winn, J. A. Orosz, A. Prsa, W. F. Welsh, S. N. Quinn, D. Latham, G. Torres, L. A. Buchhave, G. W. Marcy, J. J. Fortney, A. Shporer, E. B. Ford, J. J. Lissauer, D. Ragozzine, M. Rucker, N. Batalha, J. M. Jenkins, W. J. Borucki, D. Koch, C. K. Middour,

J. R. Hall, S. McCauliff, M. N. Fanelli, E. V. Quintana, M. J. Holman, D. A. Caldwell, M. Still, R. P. Stefanik, W. R. Brown, G. A. Esquerdo, S. Tang, G. Furesz, J. C. Geary, P. Berlind, M. L. Calkins, D. R. Short, J. H. Steffen, D. Sasselov, E. W. Dunham, W. D. Cochran, A. Boss, M. R. Haas, D. Buzasi, and D. Fischer. Kepler-16: A Transiting Circumbinary Planet. *Science*, 333:1602–, September 2011. doi: 10.1126/science.1210923.

G. Duchêne. Planet Formation in Binary Systems: A Separation-Dependent Mechanism? *ApJL*, 709:L114–L118, February 2010. doi: 10.1088/2041-8205/709/2/L114.

G. Duchêne and A. Kraus. Stellar Multiplicity. *ARAA*, 51:269–310, August 2013. doi: 10.1146/annurev-astro-081710-102602.

D. Dukes and M. R. Krumholz. Was the Sun Born in a Massive Cluster? *ApJ*, 754:56, July 2012. doi: 10.1088/0004-637X/754/1/56.

C. P. Dullemond and C. Dominik. Dust coagulation in protoplanetary disks: A rapid depletion of small grains. *A&A*, 434:971–986, May 2005. doi: 10.1051/0004-6361:20042080.

X. Dumusque, F. Pepe, C. Lovis, D. Ségransan, J. Sahlmann, W. Benz, F. Bouchy, M. Mayor, D. Queloz, N. Santos, and S. Udry. An Earth-mass planet orbiting α Centauri B. *Nature*, 491:207–211, November 2012. doi: 10.1038/nature11572.

A. Duquennoy and M. Mayor. Multiplicity among solar-type stars in the solar neighbourhood. II - Distribution of the orbital elements in an unbiased sample. *A&A*, 248:485–524, August 1991.

R. H. Durisen. *Disk Hydrodynamics*, pages 149–236. The University of Chicago Press, May 2011.

R. H. Durisen, A. P. Boss, L. Mayer, A. F. Nelson, T. Quinn, and W. K. M. Rice. Gravitational Instabilities in Gaseous Protoplanetary Disks and Implications for Giant Planet Formation. *Protostars and Planets V*, pages 607–622, 2007.

A. Eggenberger, S. Udry, and M. Mayor. Statistical properties of exoplanets. III. Planet properties and stellar multiplicity. *A&A*, 417: 353–360, April 2004. doi: 10.1051/0004-6361:20034164.

A. Einstein. Lens-Like Action of a Star by the Deviation of Light in the Gravitational Field. *Science*, 84:506–507, December 1936. doi: 10.1126/science.84.2188.506.

S. M. Fall, R. Chandar, and B. C. Whitmore. New Tests for Disruption Mechanisms of Star Clusters: Methods and Application to the Antennae Galaxies. *ApJ*, 704:453–468, October 2009. doi: 10.1088/0004-637X/704/1/453.

E. B. Ford, D. Ragozzine, J. F. Rowe, J. H. Steffen, T. Barclay, N. M. Batalha, W. J. Borucki, S. T. Bryson, D. A. Caldwell, D. C. Fabrycky, T. N. Gautier, M. J. Holman, K. A. Ibrahim, H. Kjeldsen, K. Kinemuchi, D. G. Koch, J. J. Lissauer, M. Still, P. Tenenbaum, K. Uddin, and W. Welsh. Transit Timing Observations from Kepler. V. Transit Timing Variation Candidates in the First Sixteen Months from Polynomial Models. *ApJ*, 756:185, September 2012. doi: 10.1088/0004-637X/756/2/185.

D. Forgan and K. Rice. Stellar encounters: a stimulus for disc fragmentation? *MNRAS*, 400:2022–2031, December 2009. doi: 10.1111/j.1365-2966.2009.15596.x.

D. Forgan, K. Rice, P. Cossins, and G. Lodato. The nature of angular momentum transport in radiative self-gravitating protostellar discs. *MNRAS*, 410:994–1006, January 2011. doi: 10.1111/j.1365-2966.2010.17500.x.

M. M. Fragner and R. P. Nelson. Giant planet formation in stellar clusters: the effects of stellar fly-bys. *A&A*, 505:873–889, October 2009. doi: 10.1051/0004-6361/200912292.

M. Fukagawa, T. Tsukagoshi, M. Momose, K. Saigo, N. Ohashi, Y. Kitamura, S.-i. Inutsuka, T. Muto, H. Nomura, T. Takeuchi, H. Kobayashi, T. Hanawa, E. Akiyama, M. Honda, H. Fujiwara, A. Kataoka, S. Z. Takahashi, and H. Shibai. Local Enhancement of Surface Density in the Protoplanetary Ring Surrounding HD 142527. *ArXiv e-prints*, September 2013.

C. F. Gammie. Nonlinear Outcome of Gravitational Instability in Cooling, Gaseous Disks. *ApJ*, 553:174–183, May 2001. doi: 10.1086/320631.

R. A. Gingold and J. J. Monaghan. Smoothed particle hydrodynamics - Theory and application to non-spherical stars. *MNRAS*, 181:375–389, November 1977.

L. Girardi, M. A. T. Groenewegen, E. Hatziminaoglou, and L. da Costa. Star counts in the Galaxy. Simulating from very deep to very shallow photometric surveys with the TRILEGAL code. *A&A*, 436:895–915, June 2005. doi: 10.1051/0004-6361:20042352.

L. Girardi, M. Barbieri, M. A. T. Groenewegen, P. Marigo, A. Bressan, H. J. Rocha-Pinto, B. X. Santiago, J. I. B. Camargo, and L. N. da Costa. *TRILEGAL, a TRIdimensional modeL of thE GALaxy: Status and Future*, page 165. 2012. doi: 10.1007/978-3-642-18418-5_17.

P. Goldreich and S. Soter. Q in the Solar System. *Icarus*, 5:375–389, 1966. doi: 10.1016/0019-1035(66)90051-0.

P. Goldreich and S. Tremaine. The excitation of density waves at the Lindblad and corotation resonances by an external potential. *ApJ*, 233:857–871, November 1979. doi: 10.1086/157448.

P. Goldreich and W. R. Ward. The Formation of Planetesimals. *ApJ*, 183:1051–1062, August 1973. doi: 10.1086/152291.

R. Günther and W. Kley. Circumbinary disk evolution. *A&A*, 387: 550–559, May 2002. doi: 10.1051/0004-6361:20020407.

K. E. Haisch, Jr., E. A. Lada, and C. J. Lada. Disk Frequencies and Lifetimes in Young Clusters. *ApJL*, 553:L153–L156, June 2001. doi: 10.1086/320685.

S. M. Hall, C. J. Clarke, and J. E. Pringle. Energetics of star-disc encounters in the non-linear regime. *MNRAS*, 278:303–320, January 1996.

A. P. Hatzes, W. D. Cochran, M. Endl, B. McArthur, D. B. Paulson, G. A. H. Walker, B. Campbell, and S. Yang. A Planetary Companion to γ Cephei A. *ApJ*, 599:1383–1394, December 2003. doi: 10.1086/379281.

W. D. Heacox. Of Logarithms, Binary Orbits, and Self-Replicating Distributions. *PASP*, 108:591, July 1996. doi: 10.1086/133769.

L. A. Hillenbrand. On the Stellar Population and Star-Forming History of the Orion Nebula Cluster. *AJ*, 113:1733–1768, May 1997. doi: 10.1086/118389.

M. J. Holman and N. W. Murray. The Use of Transit Timing to Detect Terrestrial-Mass Extrasolar Planets. *Science*, 307:1288–1291, February 2005. doi: 10.1126/science.1107822.

M. J. Holman and P. A. Wiegert. Long-Term Stability of Planets in Binary Systems. *AJ*, 117:621–628, January 1999. doi: 10.1086/300695.

L. L. Hood. Thermal processing of chondrule and CAI precursors in planetesimal bow shocks. *Meteoritics and Planetary Science*, 33: 97–107, January 1998. doi: 10.1111/j.1945-5100.1998.tb01611.x.

L. L. Hood, F. J. Ciesla, N. A. Artemieva, F. Marzari, and S. J. Weidenschilling. Nebular shock waves generated by planetesimals passing through Jovian resonances: Possible sites for chondrule formation. *Meteoritics and Planetary Science*, 44:327–342, April 2009. doi: 10.1111/j.1945-5100.2009.tb00736.x.

I. Hubeny. Vertical structure of accretion disks - A simplified analytical model. *ApJ*, 351:632–641, March 1990. doi: 10.1086/168501.

A. Johansen, J. S. Oishi, M.-M. Mac Low, H. Klahr, T. Henning, and A. Youdin. Rapid planetesimal formation in turbulent circumstellar disks. *Nature*, 448:1022–1025, August 2007. doi: 10.1038/nature06086.

M. K. R. Joung, M.-M. Mac Low, and D. S. Ebel. Chondrule Formation and Protoplanetary Disk Heating by Current Sheets in Nonideal Magnetohydrodynamic Turbulence. *ApJ*, 606:532–541, May 2004. doi: 10.1086/381651.

D. M. Kary, J. J. Lissauer, and Y. Greenzweig. Nebular gas drag and planetary accretion. *Icarus*, 106:288, November 1993. doi: 10.1006/icar.1993.1172.

W. Kley. Evolution of an embedded Planet in a Binary System. In *IAU Symposium*, volume 200 of *IAU Symposium*, page 211P, 2000.

W. Kley and R. P. Nelson. Planet formation in binary stars: the case of γ Cephei. *A&A*, 486:617–628, August 2008. doi: 10.1051/0004-6361:20079324.

W. Kley, J. C. B. Papaloizou, and G. I. Ogilvie. Simulations of eccentric disks in close binary systems. *A&A*, 487:671–687, August 2008. doi: 10.1051/0004-6361:200809953.

W. Kley, B. Bitsch, and H. Klahr. Planet migration in three-dimensional radiative discs. *A&A*, 506:971–987, November 2009. doi: 10.1051/0004-6361/200912072.

W. Kley, T. W. A. Müller, S. M. Kolb, P. Benítez-Llambay, and F. Masset. Low-mass planets in nearly inviscid disks: numerical treatment. *A&A*, 546:A99, October 2012. doi: 10.1051/0004-6361/201219719.

D. G. Koch, W. J. Borucki, G. Basri, N. M. Batalha, T. M. Brown, D. Caldwell, J. Christensen-Dalsgaard, W. D. Cochran, E. DeVore, E. W. Dunham, T. N. Gautier, III, J. C. Geary, R. L. Gilliland, A. Gould, J. Jenkins, Y. Kondo, D. W. Latham, J. J. Lissauer, G. Marcy, D. Monet, D. Sasselov, A. Boss, D. Brownlee, J. Caldwell, A. K. Dupree, S. B. Howell, H. Kjeldsen, S. Meibom, D. Morrison, T. Owen, H. Reitsema, J. Tarter, S. T. Bryson, J. L. Dotson, P. Gazis, M. R. Haas, J. Kolodziejczak, J. F. Rowe, J. E. Van Cleve, C. Allen, H. Chandrasekaran, B. D. Clarke, J. Li, E. V. Quintana, P. Tenenbaum, J. D. Twicken, and H. Wu. Kepler Mission Design, Realized Photometric Performance, and Early Science. *ApJL*, 713:L79, April 2010. doi: 10.1088/2041-8205/713/2/L79.

R. H. Koch and B. J. Hrivnak. On Zahn's theory of tidal friction for cool, main-sequence close binaries. *AJ*, 86:438–441, March 1981. doi: 10.1086/112902.

E. Kokubo and S. Ida. On Runaway Growth of Planetesimals. *Icarus*, 123:180–191, September 1996. doi: 10.1006/icar.1996.0148.

V. B. Kostov, P. R. McCullough, J. A. Carter, M. Deleuil, R. F. Diaz, D. C. Fabrycky, G. Hebrard, T. C. Hinse, T. Mazeh, J. A. Orosz, Z. I. Tsvetanov, and W. F. Welsh. Kepler-413b: a slightly misaligned, Neptune-size transiting circumbinary planet. *ArXiv e-prints*, January 2014.

Y. Kozai. Secular perturbations of asteroids with high inclination and eccentricity. *AJ*, 67:591, November 1962. doi: 10.1086/108790.

P. Kroupa. Inverse dynamical population synthesis and star formation. *MNRAS*, 277:1491, December 1995.

G. P. Kuiper. On the Origin of the Solar System. In J. A. Hynek, editor, *50th Anniversary of the Yerkes Observatory and Half a Century of Progress in Astrophysics*, page 357, 1951.

A.-M. Lagrange, M. Bonnefoy, G. Chauvin, D. Apai, D. Ehrenreich, A. Boccaletti, D. Gratadour, D. Rouan, D. Mouillet, S. Lacour, and M. Kasper. A Giant Planet Imaged in the Disk of the Young Star β Pictoris. *Science*, 329:57–, July 2010. doi: 10.1126/science.1187187.

Z. M. Leinhardt and S. T. Stewart. Collisions between Gravity-dominated Bodies. I. Outcome Regimes and Scaling Laws. *ApJ*, 745:79, January 2012. doi: 10.1088/0004-637X/745/1/79.

C. D. Levermore and G. C. Pomraning. A flux-limited diffusion theory. *ApJ*, 248:321–334, August 1981. doi: 10.1086/159157.

E. H. Levy and S. Araki. Magnetic reconnection flares in the protoplanetary nebula and the possible origin of meteorite chondrules. *Icarus*, 81:74–91, September 1989. doi: 10.1016/0019-1035(89)90126-7.

D. N. C. Lin and J. Papaloizou. Tidal torques on accretion discs in binary systems with extreme mass ratios. *MNRAS*, 186:799–812, March 1979.

J. J. Lissauer. Planet formation. *ARAA*, 31:129–174, 1993. doi: 10.1146/annurev.aa.31.090193.001021.

G. Lodato and P. J. Cossins. Smoothed Particle Hydrodynamics for astrophysical flows. The dynamics of protostellar discs. *European Physical Journal Plus*, 126:44, April 2011. doi: 10.1140/epjp/i2011-11044-6.

G. Lodato and D. J. Price. On the diffusive propagation of warps in thin accretion discs. *MNRAS*, 405:1212–1226, June 2010. doi: 10.1111/j.1365-2966.2010.16526.x.

S. H. Lubow and G. I. Ogilvie. Three-dimensional Waves Generated at Lindblad Resonances in Thermally Stratified Disks. *ApJ*, 504:983, September 1998. doi: 10.1086/306104.

D. Malmberg and M. B. Davies. On the origin of eccentricities among extrasolar planets. *MNRAS*, 394:L26–L30, March 2009. doi: 10.1111/j.1745-3933.2008.00603.x.

D. Malmberg, F. de Angeli, M. B. Davies, R. P. Church, D. Mackey, and M. I. Wilkinson. Close encounters in young stellar clusters: implications for planetary systems in the solar neighbourhood. *MNRAS*, 378:1207–1216, July 2007. doi: 10.1111/j.1365-2966.2007.11885.x.

D. Malmberg, M. B. Davies, and D. C. Heggie. The effects of fly-bys on planetary systems. *MNRAS*, 411:859–877, February 2011. doi: 10.1111/j.1365-2966.2010.17730.x.

J. G. Martí and C. Beaugé. Stellar scattering and the origin of the planet around γ-Cephei-A. *A&A*, 544:A97, August 2012. doi: 10.1051/0004-6361/201219403.

A. F. Martínez Fiorenzano, R. G. Gratton, S. Desidera, R. Cosentino, and M. Endl. Line bisectors and radial velocity jitter from SARG spectra. *A&A*, 442:775–784, November 2005. doi: 10.1051/0004-6361:20052888.

M. A. Martos and D. P. Cox. Magnetohydrodynamic Modeling of a Galactic Spiral Arm as a Combination Shock and Hydraulic Jump. *ApJ*, 509:703–716, December 1998. doi: 10.1086/306514.

F. Marzari and M. Barbieri. Planets in binary systems: is the present configuration indicative of the formation process? *A&A*, 467:347–351, May 2007a. doi: 10.1051/0004-6361:20077102.

F. Marzari and M. Barbieri. Planet dispersal in binary systems during transient multiple star phases. *A&A*, 472:643–647, September 2007b. doi: 10.1051/0004-6361:20077876.

F. Marzari and H. Scholl. Planetesimal Accretion in Binary Star Systems. *ApJ*, 543:328–339, November 2000. doi: 10.1086/317091.

F. Marzari and S. J. Weidenschilling. Eccentric Extrasolar Planets: The Jumping Jupiter Model. *Icarus*, 156:570–579, April 2002. doi: 10.1006/icar.2001.6786.

F. Marzari, S. J. Weidenschilling, M. Barbieri, and V. Granata. Jumping Jupiters in Binary Star Systems. *ApJ*, 618:502–511, January 2005. doi: 10.1086/425976.

F. Marzari, P. Thébault, and H. Scholl. Planetesimal Evolution in Circumbinary Gaseous Disks: A Hybrid Model. *ApJ*, 681:1599–1608, July 2008. doi: 10.1086/588423.

F. Marzari, H. Scholl, P. Thébault, and C. Baruteau. On the eccentricity of self-gravitating circumstellar disks in eccentric binary systems. *A&A*, 508:1493–1502, December 2009. doi: 10.1051/0004-6361/200912251.

F. Marzari, C. Baruteau, and H. Scholl. Planet-planet scattering in circumstellar gas disks. *A&A*, 514:L4, May 2010. doi: 10.1051/0004-6361/201014716.

F. Marzari, C. Baruteau, H. Scholl, and P. Thebault. Eccentricity of radiative disks in close binary-star systems. *A&A*, 539:A98, March 2012. doi: 10.1051/0004-6361/201118075.

B. D. Mason, D. R. Gies, W. I. Hartkopf, W. G. Bagnuolo, Jr., T. ten Brummelaar, and H. A. McAlister. ICCD speckle observations of binary stars. XIX - an astrometric/spectroscopic survey of O stars. *AJ*, 115:821, February 1998. doi: 10.1086/300234.

F. Masset. FARGO: A fast eulerian transport algorithm for differentially rotating disks. *A&AS*, 141:165–173, January 2000. doi: 10.1051/aas:2000116.

M. Mayor and D. Queloz. A Jupiter-mass companion to a solar-type star. *Nature*, 378:355–359, November 1995. doi: 10.1038/378355a0.

F. Meru. *On the fragmentation of self-gravitating discs*. PhD thesis, University of Exeter, 2010.

F. Meru and M. R. Bate. On the convergence of the critical cooling time-scale for the fragmentation of self-gravitating discs. *MNRAS*, 427:2022–2046, December 2012. doi: 10.1111/j.1365-2966.2012.22035.x.

S. Meschiari. Circumbinary Planet Formation in the Kepler-16 System. I. N-body Simulations. *ApJ*, 752:71, June 2012. doi: 10.1088/0004-637X/752/1/71.

S. A. Metchev and L. A. Hillenbrand. The Palomar/Keck Adaptive Optics Survey of Young Solar Analogs: Evidence for a Universal Companion Mass Function. *ApJS*, 181:62–109, March 2009. doi: 10.1088/0067-0049/181/1/62.

D. Mihalas and B. W. Mihalas. *Foundations of radiation hydrodynamics*. Oxford University Press, 1984.

J. J. Monaghan. Particle methods for hydrodynamics. *Comp. Phys. Rep.*, 3:71–124, October 1985.

J. J. Monaghan and R. A. Gingold. Shock Simulation by the Particle Method SPH. *Journal of Computational Physics*, 52:374, November 1983. doi: 10.1016/0021-9991(83)90036-0.

C. Mordasini, Y. Alibert, H. Klahr, and T. Henning. Characterization of exoplanets from their formation. I. Models of combined planet formation and evolution. *A&A*, 547:A111, November 2012. doi: 10.1051/0004-6361/201118457.

G. Morfill, H. Spruit, and E. H. Levy. Physical processes and conditions associated with the formation of protoplanetary disks. In E. H. Levy and J. I. Lunine, editors, *Protostars and Planets III*, pages 939–978, 1993.

K. Moriwaki and Y. Nakagawa. A Planetesimal Accretion Zone in a Circumbinary Disk. *ApJ*, 609:1065–1070, July 2004. doi: 10.1086/421342.

J. P. Morris and J. J. Monaghan. A Switch to Reduce SPH Viscosity. *Journal of Computational Physics*, 136:41–50, September 1997. doi: 10.1006/jcph.1997.5690.

M. A. Morris, A. C. Boley, S. J. Desch, and T. Athanassiadou. Chondrule Formation in Bow Shocks around Eccentric Planetary Embryos. *ApJ*, 752:27, June 2012. doi: 10.1088/0004-637X/752/1/27.

M. Mugrauer and R. Neuhäuser. The multiplicity of exoplanet host stars. New low-mass stellar companions of the exoplanet host stars HD 125612 and HD 212301. *A&A*, 494:373–378, January 2009. doi: 10.1051/0004-6361:200810639.

M. Mugrauer, R. Neuhäuser, A. Seifahrt, T. Mazeh, and E. Guenther. Four new wide binaries among exoplanet host stars. *A&A*, 440: 1051–1060, September 2005. doi: 10.1051/0004-6361:20042297.

T. W. A. Müller and W. Kley. Circumstellar disks in binary star systems. Models for γ Cephei and α Centauri. *A&A*, 539:A18, March 2012. doi: 10.1051/0004-6361/201118202.

C. D. Murray and S. F. Dermott. *Solar system dynamics*. Cambridge University Press, 1999.

M. W. Muterspaugh, B. F. Lane, S. R. Kulkarni, M. Konacki, B. F. Burke, M. M. Colavita, M. Shao, W. I. Hartkopf, A. P. Boss, and M. Williamson. The Phases Differential Astrometry Data Archive. V. Candidate Substellar Companions to Binary Systems. *AJ*, 140: 1657–1671, December 2010. doi: 10.1088/0004-6256/140/6/1657.

D. Naef, D. W. Latham, M. Mayor, T. Mazeh, J. L. Beuzit, G. A. Drukier, C. Perrier-Bellet, D. Queloz, J. P. Sivan, G. Torres, S. Udry, and S. Zucker. HD 80606 b, a planet on an extremely elongated orbit. *A&A*, 375:L27–L30, August 2001. doi: 10.1051/0004-6361:20010853.

T. Nakamoto, M. R. Hayashi, N. T. Kita, and S. Tachibana. Chondrule-forming Shock Waves in the Solar Nebula by X-Ray Flares. In A. N. Krot, E. R. D. Scott, and B. Reipurth, editors, *Chondrites and the Protoplanetary Disk*, volume 341 of *Astronomical Society of the Pacific Conference Series*, page 883, December 2005.

A. F. Nelson. Planet Formation is Unlikely in Equal-Mass Binary Systems with A ˜ 50 AU. *ApJL*, 537:L65–L68, July 2000. doi: 10.1086/312752.

A. F. Nelson, M. Wetzstein, and T. Naab. Vine – A Numerical Code for Simulating Astrophysical Systems Using Particles. II. Implementation and Performance Characteristics. *ApJS*, 184:326–360, October 2009. doi: 10.1088/0067-0049/184/2/326.

R. P. Nelson and O. Gressel. On the dynamics of planetesimals embedded in turbulent protoplanetary discs. *MNRAS*, 409:639–661, December 2010. doi: 10.1111/j.1365-2966.2010.17327.x.

J. A. Orosz, W. F. Welsh, J. A. Carter, E. Brugamyer, L. A. Buchhave, W. D. Cochran, M. Endl, E. B. Ford, P. MacQueen, D. R. Short, G. Torres, G. Windmiller, E. Agol, T. Barclay, D. A. Caldwell, B. D. Clarke, L. R. Doyle, D. C. Fabrycky, J. C. Geary, N. Haghighipour, M. J. Holman, K. A. Ibrahim, J. M. Jenkins, K. Kinemuchi, J. Li, J. J. Lissauer, A. Prša, D. Ragozzine, A. Shporer, M. Still, and R. A. Wade. The Neptune-sized Circumbinary Planet Kepler-38b. *ApJ*, 758:87, October 2012a. doi: 10.1088/0004-637X/758/2/87.

J. A. Orosz, W. F. Welsh, J. A. Carter, D. C. Fabrycky, W. D. Cochran, M. Endl, E. B. Ford, N. Haghighipour, P. J. MacQueen, T. Mazeh, R. Sanchis-Ojeda, D. R. Short, G. Torres, E. Agol, L. A. Buchhave, L. R. Doyle, H. Isaacson, J. J. Lissauer, G. W. Marcy, A. Shporer, G. Windmiller, T. Barclay, A. P. Boss, B. D. Clarke, J. Fortney, J. C. Geary, M. J. Holman, D. Huber, J. M. Jenkins, K. Kinemuchi, E. Kruse, D. Ragozzine, D. Sasselov, M. Still, P. Tenenbaum, K. Uddin, J. N. Winn, D. G. Koch, and W. J. Borucki. Kepler-47: A Transiting Circumbinary Multiplanet System. *Science*, 337:1511–, September 2012b. doi: 10.1126/science.1228380.

M. Osorio, P. D'Alessio, J. Muzerolle, N. Calvet, and L. Hartmann. A Comprehensive Study of the L1551 IRS 5 Binary System. *ApJ*, 586:1148–1161, April 2003. doi: 10.1086/367695.

S.-J. Paardekooper and Z. M. Leinhardt. Planetesimal collisions in binary systems. *MNRAS*, 403:L64–L68, March 2010. doi: 10.1111/j.1745-3933.2010.00816.x.

S.-J. Paardekooper, P. Thébault, and G. Mellema. Planetesimal and gas dynamics in binaries. *MNRAS*, 386:973–988, May 2008. doi: 10.1111/j.1365-2966.2008.13080.x.

S.-J. Paardekooper, C. Baruteau, and W. Kley. A torque formula for non-isothermal Type I planetary migration - II. Effects of diffusion. *MNRAS*, 410:293–303, January 2011. doi: 10.1111/j.1365-2966.2010.17442.x.

S.-J. Paardekooper, Z. M. Leinhardt, P. Thébault, and C. Baruteau. How Not to Build Tatooine: The Difficulty of In Situ Formation of Circumbinary Planets Kepler 16b, Kepler 34b, and Kepler 35b. *ApJL*, 754:L16, July 2012. doi: 10.1088/2041-8205/754/1/L16.

B. Paczynski. A model of selfgravitating accretion disk. *ACTAA*, 28: 91–109, 1978.

F. Palla and S. W. Stahler. Accelerating Star Formation in Clusters and Associations. *ApJ*, 540:255–270, September 2000. doi: 10.1086/309312.

J. C. B. Papaloizou and C. Terquem. Planet formation and migration. *Reports on Progress in Physics*, 69:119–180, January 2006. doi: 10.1088/0034-4885/69/1/R03.

R. J. Parker and S. P. Quanz. On the frequency of planetary systems around G dwarfs. *MNRAS*, 436:650–658, November 2013. doi: 10.1093/mnras/stt1603.

R. J. Parker, S. P. Goodwin, and R. J. Allison. The evolution of binary populations in cool, clumpy star clusters. *MNRAS*, 418:2565–2575, December 2011. doi: 10.1111/j.1365-2966.2011.19646.x.

M. J. Payne, M. C. Wyatt, and P. Thébault. Outward migration of terrestrial embryos in binary systems. *MNRAS*, 400:1936–1944, December 2009. doi: 10.1111/j.1365-2966.2009.15586.x.

S. J. Peale. Orbital resonances in the solar system. *ARAA*, 14:215–246, 1976. doi: 10.1146/annurev.aa.14.090176.001243.

F. I. Pelupessy and S. Portegies Zwart. The formation of planets in circumbinary discs. *MNRAS*, 429:895–902, February 2013. doi: 10.1093/mnras/sts461.

A. Pierens and R. P. Nelson. On the migration of protoplanets embedded in circumbinary disks. *A&A*, 472:993–1001, September 2007. doi: 10.1051/0004-6361:20077659.

A. Pierens and R. P. Nelson. On the formation and migration of giant planets in circumbinary discs. *A&A*, 483:633–642, May 2008. doi: 10.1051/0004-6361:200809453.

W. Pilipp, T. W. Hartquist, G. E. Morfill, and E. H. Levy. Chondrule formation by lightning in the Protosolar Nebula? *A&A*, 331:121–146, March 1998.

A. Porras, M. Christopher, L. Allen, J. Di Francesco, S. T. Megeath, and P. C. Myers. A Catalog of Young Stellar Groups and Clusters within 1 Kiloparsec of the Sun. *AJ*, 126:1916–1924, October 2003. doi: 10.1086/377623.

D. J. Price and J. J. Monaghan. Smoothed Particle Magnetohydrodynamics - II. Variational principles and variable smoothing-length terms. *MNRAS*, 348:139–152, February 2004. doi: 10.1111/j.1365-2966.2004.07346.x.

D. J. Price and J. J. Monaghan. An energy-conserving formalism for adaptive gravitational force softening in smoothed particle hydrodynamics and N-body codes. *MNRAS*, 374:1347–1358, February 2007. doi: 10.1111/j.1365-2966.2006.11241.x.

D. Queloz, M. Mayor, L. Weber, A. Blécha, M. Burnet, B. Confino, D. Naef, F. Pepe, N. Santos, and S. Udry. The CORALIE survey for southern extra-solar planets. I. A planet orbiting the star Gliese 86. *A&A*, 354:99–102, February 2000.

R. R. Rafikov. Building Tatooine: Suppression of the Direct Secular Excitation in Kepler Circumbinary Planet Formation. *ApJL*, 764:L16, February 2013. doi: 10.1088/2041-8205/764/1/L16.

D. Raghavan, H. A. McAlister, T. J. Henry, D. W. Latham, G. W. Marcy, B. D. Mason, D. R. Gies, R. J. White, and T. A. ten Brummelaar. A Survey of Stellar Families: Multiplicity of Solar-type Stars. *ApJS*, 190:1–42, September 2010. doi: 10.1088/0067-0049/190/1/1.

F. A. Rasio and E. B. Ford. Dynamical instabilities and the formation of extrasolar planetary systems. *Science*, 274:954–956, November 1996.

N. J. Rattenbury. Microlensing of close binary stars. *MNRAS*, 392:439–447, January 2009. doi: 10.1111/j.1365-2966.2008.14074.x.

S. Refsdal. The gravitational lens effect. *MNRAS*, 128:295, 1964.

W. W. Roberts, Jr., J. M. Huntley, and G. D. van Albada. Gas dynamics in barred spirals - Gaseous density waves and galactic shocks. *ApJ*, 233:67–84, October 1979. doi: 10.1086/157367.

L. F. Rodríguez, P. D'Alessio, D. J. Wilner, P. T. P. Ho, J. M. Torrelles, S. Curiel, Y. Gómez, S. Lizano, A. Pedlar, J. Cantó, and A. C. Raga. Compact protoplanetary disks around the stars of a young binary system. *Nature*, 395:355–357, September 1998. doi: 10.1038/26421.

T. Roell, R. Neuhäuser, A. Seifahrt, and M. Mugrauer. Extrasolar planets in stellar multiple systems. *A&A*, 542:A92, June 2012. doi: 10.1051/0004-6361/201118051.

R. A. Rossiter. On the detection of an effect of rotation during eclipse in the velocity of the brigher component of beta Lyrae, and on the constancy of velocity of this system. *ApJ*, 60:15–21, July 1924. doi: 10.1086/142825.

S. Rosswog, M. B. Davies, F.-K. Thielemann, and T. Piran. Merging neutron stars: asymmetric systems. *A&A*, 360:171–184, August 2000.

T. V. Ruzmaikina and W. H. Ip. Chondrule formation in radiative shock. *Icarus*, 112:430–447, December 1994. doi: 10.1006/icar.1994.1196.

P. D. Sackett. Searching for Unseen Planets via Occultation and Microlensing. In J.-M. Mariotti and D. Alloin, editors, *NATO ASIC Proc. 532: Planets Outside the Solar System: Theory and Observations*, page 189, 1999.

I. S. Sanders and G. J. Taylor. Implications of ^{26}Al in Nebular Dust: Formation of Chondrules by Disruption of Molten Planetesimals. In A. N. Krot, E. R. D. Scott, and B. Reipurth, editors, *Chondrites and the Protoplanetary Disk*, volume 341 of *Astronomical Society of the Pacific Conference Series*, page 915, December 2005.

N. I. Shakura and R. A. Sunyaev. Black holes in binary systems. Observational appearance. *A&A*, 24:337–355, 1973.

V. Springel and L. Hernquist. Cosmological smoothed particle hydrodynamics simulations: the entropy equation. *MNRAS*, 333:649–664, July 2002. doi: 10.1046/j.1365-8711.2002.05445.x.

H. Tanaka, T. Takeuchi, and W. R. Ward. Three-Dimensional Interaction between a Planet and an Isothermal Gaseous Disk. I. Corotation and Lindblad Torques and Planet Migration. *ApJ*, 565:1257–1274, February 2002. doi: 10.1086/324713.

P. Thebault. Against all odds? Forming the planet of the HD 196885 binary. *Celestial Mechanics and Dynamical Astronomy*, 111:29–49, October 2011. doi: 10.1007/s10569-011-9346-2.

P. Thébault, F. Marzari, H. Scholl, D. Turrini, and M. Barbieri. Planetary formation in the γ Cephei system. *A&A*, 427:1097–1104, December 2004. doi: 10.1051/0004-6361:20040514.

P. Thébault, F. Marzari, and H. Scholl. Relative velocities among accreting planetesimals in binary systems: The circumprimary case. *Icarus*, 183:193–206, July 2006. doi: 10.1016/j.icarus.2006.01.022.

P. Thébault, F. Marzari, and H. Scholl. Planet formation in α Centauri A revisited: not so accretion friendly after all. *MNRAS*, 388:1528–1536, August 2008. doi: 10.1111/j.1365-2966.2008.13536.x.

P. Thébault, F. Marzari, and H. Scholl. Planet formation in the habitable zone of α Centauri B. *MNRAS*, 393:L21–L25, February 2009. doi: 10.1111/j.1745-3933.2008.00590.x.

A. Toomre. On the gravitational stability of a disk of stars. *ApJ*, 139: 1217–1238, May 1964. doi: 10.1086/147861.

A. H. M. J. Triaud, A. Collier Cameron, D. Queloz, D. R. Anderson, M. Gillon, L. Hebb, C. Hellier, B. Loeillet, P. F. L. Maxted, M. Mayor, F. Pepe, D. Pollacco, D. Ségransan, B. Smalley, S. Udry, R. G. West, and P. J. Wheatley. Spin-orbit angle measurements for six southern transiting planets. New insights into the dynamical origins of hot Jupiters. *A&A*, 524:A25, December 2010. doi: 10.1051/0004-6361/201014525.

H. C. Urey. Parent bodies of the meteorites and the origin of chondrules. *Icarus*, 7:350–359, 1967. doi: 10.1016/0019-1035(67)90079-6.

H. C. Urey and H. Craig. The composition of the stone meteorites and the origin of the meteorites. *Geochim. Cosmochim. Acta*, 4:36–82, August 1953. doi: 10.1016/0016-7037(53)90064-7.

B. van Leer. Towards the Ultimate Conservative Difference Scheme. IV. A New Approach to Numerical Convection. *Journal of Computational Physics*, 23:276, March 1977. doi: 10.1016/0021-9991(77)90095-X.

S. J. Weidenschilling. Aerodynamics of solid bodies in the solar nebula. *MNRAS*, 180:57–70, July 1977.

S. J. Weidenschilling and F. Marzari. Gravitational scattering as a possible origin for giant planets at small stellar distances. *Nature*, 384:619–621, December 1996. doi: 10.1038/384619a0.

S. J. Weidenschilling, F. Marzari, and L. L. Hood. The Origin of Chondrules at Jovian Resonances. *Science*, 279:681, January 1998. doi: 10.1126/science.279.5351.681.

W. F. Welsh, J. A. Orosz, J. A. Carter, D. C. Fabrycky, E. B. Ford, J. J. Lissauer, A. Prša, S. N. Quinn, D. Ragozzine, D. R. Short, G. Torres, J. N. Winn, L. R. Doyle, T. Barclay, N. Batalha, S. Bloemen, E. Brugamyer, L. A. Buchhave, C. Caldwell, D. A. Caldwell, J. L. Christiansen, D. R. Ciardi, W. D. Cochran, M. Endl, J. J. Fortney, T. N. Gautier, III, R. L. Gilliland, M. R. Haas, J. R. Hall, M. J. Holman, A. W. Howard, S. B. Howell, H. Isaacson, J. M. Jenkins, T. C. Klaus, D. W. Latham, J. Li, G. W. Marcy, T. Mazeh, E. V. Quintana, P. Robertson, A. Shporer, J. H. Steffen, G. Windmiller, D. G.

Koch, and W. J. Borucki. Transiting circumbinary planets Kepler-34 b and Kepler-35 b. *Nature*, 481:475–479, January 2012. doi: 10.1038/nature10768.

W. F. Welsh, J. A. Orosz, J. A. Carter, and D. C. Fabrycky. Recent Kepler Results On Circumbinary Planets. *ArXiv e-prints*, August 2013.

M. W. Werner, T. L. Roellig, F. J. Low, G. H. Rieke, M. Rieke, W. F. Hoffmann, E. Young, J. R. Houck, B. Brandl, G. G. Fazio, J. L. Hora, R. D. Gehrz, G. Helou, B. T. Soifer, J. Stauffer, J. Keene, P. Eisenhardt, D. Gallagher, T. N. Gautier, W. Irace, C. R. Lawrence, L. Simmons, J. E. Van Cleve, M. Jura, E. L. Wright, and D. P. Cruikshank. The Spitzer Space Telescope Mission. *ApJS*, 154:1–9, September 2004. doi: 10.1086/422992.

M. Wetzstein, A. F. Nelson, T. Naab, and A. Burkert. Vine – A Numerical Code for Simulating Astrophysical Systems Using Particles. I. Description of the Physics and the Numerical Methods. *ApJS*, 184: 298–325, October 2009. doi: 10.1088/0067-0049/184/2/298.

S. C. Whitehouse and M. R. Bate. Smoothed particle hydrodynamics with radiative transfer in the flux-limited diffusion approximation. *MNRAS*, 353:1078–1094, October 2004. doi: 10.1111/j.1365-2966.2004.08131.x.

J. N. Winn. *Exoplanet Transits and Occultations*, pages 55–77. University of Arizona Press, 2011.

A. Wolszczan and D. A. Frail. A planetary system around the millisecond pulsar PSR1257 + 12. *Nature*, 355:145–147, January 1992. doi: 10.1038/355145a0.

J. A. Wood. Processing of chondritic and planetary material in spiral density waves in the nebula. *Meteoritics and Planetary Science*, 31: 641–645, September 1996. doi: 10.1111/j.1945-5100.1996.tb02037.x.

G. Wurm, G. Paraskov, and O. Krauss. Growth of planetesimals by impacts at $\sim$ 25 m/s. *Icarus*, 178:253–263, November 2005. doi: 10.1016/j.icarus.2005.04.002.

J.-W. Xie and J.-L. Zhou. Planetesimal Accretion in Binary Systems: Role of the Companion's Orbital Inclination. *ApJ*, 698:2066–2074, June 2009. doi: 10.1088/0004-637X/698/2/2066.

J.-W. Xie, M. J. Payne, P. Thébault, J.-L. Zhou, and J. Ge. From Dust to Planetesimal: The Snowball Phase? *ApJ*, 724:1153–1164, December 2010a. doi: 10.1088/0004-637X/724/2/1153.

J.-W. Xie, J.-L. Zhou, and J. Ge. Planetesimal Accretion in Binary Systems: Could Planets Form Around α Centauri B? *ApJ*, 708:1566–1578, January 2010b. doi: 10.1088/0004-637X/708/2/1566.

N. L. Zakamska and S. Tremaine. Excitation and Propagation of Eccentricity Disturbances in Planetary Systems. *AJ*, 128:869–877, August 2004. doi: 10.1086/422023.

S. Zucker and T. Mazeh. On the Mass-Period Correlation of the Extrasolar Planets. *ApJL*, 568:L113–L116, April 2002. doi: 10.1086/340373.

S. Zucker, T. Mazeh, N. C. Santos, S. Udry, and M. Mayor. Multi-order TODCOR: Application to observations taken with the CORALIE echelle spectrograph. II. A planet in the system <ASTROBJ>HD 41004</ASTROBJ>. *A&A*, 426:695–698, November 2004. doi: 10.1051/0004-6361:20040384.